VENTILATION PERFORMANCE OF PASSENGER AIRCRAFT IN CONTROLLING CONTAMINANT DISPERSION FROM EXPIRATORY EVENTS

by
Hossam A. Abdelaal

A Thesis
presented to
The University of Guelph

In partial fulfilment of requirements
for the degree of
Doctor of Philosophy
in
Mechanical Engineering

Guelph, Ontario, Canada

ABSTRACT

VENTILATION PERFORMANCE OF PASSENGER AIRCRAFT IN CONTROLLING CONTAMINANT DISPERSION FROM EXPIRATORY EVENTS

Hossam A. Abdelaal
University of Guelph, 2019

Advisors:
Dr. Yi Wai Chiang
Dr. Amir Abbas Aliabadi

The cabins of passenger aircraft experience one of the most complex indoor environments among all other means of mass public transportation. Numerical simulations for the ventilation performance in mitigating the passenger exposure to cough-released airborne contaminant are performed in a model for a Boeing 767-300 sectional cabin. The effect of the aircraft acceleration-induced body forces on the airflow patterns and the contaminant dispersion behavior in the cabin is investigated for different aircraft operating conditions. Sulfur hexafluoride (SF_6) was used as a surrogate for cough particles in the size from 1.6 to 3.0 µm. The flight legs studied are the steady level flight (cruise) leg, and the climb and descent legs under both the aircraft normal and extreme (flight through gusts) operating conditions. It was found that the acceleration-induced body forces on the aircraft have limited effect on the contaminant dispersion behavior under normal operating conditions. However, under extreme operating conditions, it was found that those body forces have a significant impact on the contaminant dispersion phenomena, especially during the climb leg, during which the exposure to cough-released airborne contaminants may reach 2.8 to 3 times its counterpart during other flight legs. To counter those high passenger exposures, different airflow design and source control strategies are researched for their ability to reduce the airborne contam-

inant dispersion in the aircraft cabin model during the steady level flight leg and climb leg under extreme operating conditions. Some strategies were effective and resulted in exposures reduced by up to 60 %. To complement the findings attained utilizing the SF_6 surrogate, uniform particles with diameters 2.5 µm, 7.5 µm, and 10 µm were injected in the cabin model. It was found that the 7.5 µm particles exhibited a dissimilar dispersion behavior to the 2.5 and 10 µm particles as they could stay for long time in the cabin without settling and/or depositing on surfaces during the two investigated flight legs. This indicates that expiratory airborne particles of intermediate size can pose the greatest infection risk on the passengers throughout most of the flight duration.

Dedication

This work would not have been possible without the reconciliation of Allah the Almighty and Most Merciful. I would like to wholeheartedly thank Dr. Yi Wai Chiang and Dr. Amir Abbas Aliabadi for their passionate mentorship and everlasting support that made this research see the light. I also thank my small family; my lovely wife Mai and daughter Cady, who are with me here in Canada, and my father, god bless his soul, mother, and brother back in Egypt for their prayers, love and support. Lastly, I thank all my friends and colleagues at the University of Guelph for being my family away from home.

Acknowledgements

The authors thank the Government of Ontario, Canada, for providing the funding for this work in the form of the Ontario Trillium Scholarship (OTS) for the lead author. The authors also thank Natural Sciences and Engineering Research Council (NSERC) of Canada, specifically the Discovery Grant program (Grant Number 401231) supporting the lead author knowledge dissemination in conferences and journals. They also thank Dr. Christopher Y. H. Chao (Department of Mechanical Engineering, Hong Kong University of Science and Technology, Clear Water Bay, Hong Kong, China), and Dr. Man Pun Wan (Department of Mechanical and Aerospace Engineering, Nanyang Technological University, Singapore) for providing their full experimental research data. Additionally, the authors recognize CMC Microsystems for providing the Academic Research license of ANSYS. Finally, they thank the Centre for Advanced Computing (CAC) at Queen's University (Kingston, ON, Canada) for allowing access to the Frontenac Compute Cluster, and SHARCNET for providing the Graham cluster to run the simulations.

Table of Contents

List of Tables **ix**

List of Figures **xiii**

List of Abbreviations **xiv**

List of Mathematical Symbols **xvi**

1 Introduction **1**
- 1.1 Motivation . . . 2
- 1.2 Contributions to the Scientific Field . . . 3
- 1.3 Thesis Structure . . . 3

2 Literature Review and Objectives **5**
- 2.1 Airborne Contaminants Aboard Aircraft . . . 5
  - 2.1.1 Gaseous Contaminants . . . 6
  - 2.1.2 Particulate Contaminants . . . 8
- 2.2 Aircraft Ventilation Strategies and their Effect on Air Quality and Airborne Infection Aboard . . . 10
- 2.3 Research Approaches for Studying Airflow Distribution and Air Quality in Aircraft Cabins . . . 13
- 2.4 Best Practices for Aircraft Airflow and Air Quality Research . . . 17
  - 2.4.1 Attributes and Scope of the Research . . . 18
  - 2.4.2 Experimental Work Difficulties and Advantages . . . 18
  - 2.4.3 Numerical Modelling Characteristics and Requirements . . . 21
- 2.5 Conclusions . . . 25
- 2.6 Investigated Research Gaps and Current Study Objectives . . . 26

3 Aircraft Cabin Model and Governing Equations **28**
- 3.1 Simulated Cabin Geometry . . . 28
- 3.2 Model Boundary and Initial Conditions . . . 29
- 3.3 Governing Equations . . . 32
- 3.4 Conclusions . . . 34

4 Grid Creation and Model Validation **36**
4.1 Grid Properties and Independence Test 36
4.2 Model Validation and Error Estimation 39
4.2.1 Validation using Contaminant Concentration Time Series 39
4.2.2 Validation using Ventilation Airflow Velocities 42
4.3 Conclusions 44

5 Airflow Design and Source Control Strategies for Reducing Airborne Contaminant Exposure in the Aircraft Cabin During the Steady Level Flight Leg **45**
5.1 Airflow Design Strategies 45
5.1.1 Airflow Direction 45
5.1.2 Airflow Rate 51
5.2 Source Control Strategies 57
5.2.1 Cough Direction 57
5.2.2 Cough Velocity (Volumetric Flow Rate) 59
5.2.3 Cougher Location in the Cabin 63
5.3 Conclusions 72

6 Acceleration-Induced Body Forces on Passenger Aircraft During the Climb and Descent Legs under Normal and Extreme Operating Conditions **75**
6.1 Aircraft Normal Operating Conditions 75
6.1.1 Method for Calculating the Acceleration Components for the Climb and Descent Legs under Normal Operating Conditions 75
6.1.2 Effect on Contaminant Dispersion behavior in the Cabin under Normal Operating Conditions 78
6.2 Aircraft Extreme Operating Conditions 80
6.2.1 Defining the Acceleration Components for the Climb and Descent Legs under Extreme Operating Conditions 80
6.2.2 Effect on Airflow Patterns and Circulation in the Cabin under Extreme Operating Conditions 81
6.2.3 Effect on Contaminant Dispersion behavior in the Cabin under Extreme Operating Conditions 87
6.3 Conclusions 98

7 Airflow Design and Source Control Strategies for Reducing Airborne Contaminant Exposure in the Aircraft Cabin During the Climb Leg under Extreme Operating Conditions **101**
7.1 Airflow Design Strategies 102
7.1.1 Airflow Direction 102
7.1.2 Airflow Rate 104
7.2 Source Control Strategies 108
7.2.1 Cough Direction 108

7.2.2 Cough Velocity . . . 112
7.2.3 Cougher Location in the Cabin . . . 114
7.3 Conclusions . . . 120

8 Comparison of Particulate Contaminant Dispersion behavior in the Aircraft Cabin between the Climb Leg under Extreme Operating Conditions and the Steady Level Flight Leg 123
8.1 Cough-Released Particles . . . 124
8.2 Passenger Exposure Ratios . . . 127
8.3 Conclusions . . . 128

9 Conclusions and Future Work 129
9.1 Conclusions . . . 129
9.1.1 Climb and Descent Legs Under Aircraft Normal Operating Conditions 130
9.1.2 Climb and Descent Legs Under Aircraft Extreme Operating Conditions 131
9.1.3 Passenger Exposure Reduction Strategies between the Steady Level Flight Leg and the Climb Leg under Aircraft Extreme Operating Conditions . . . 132
9.1.4 Cough-released Particles Dispersion behavior in the Cabin . . . 135
9.1.5 Merits and Limitations of the Current Study . . . 135
9.2 Further Research Gaps and Future Research Topics . . . 136
9.2.1 Determination of Contaminant Levels and Properties in Aircraft Cabins 136
9.2.2 Aircraft Ventilation Strategies . . . 136
9.2.3 Suggested Air Quality Research Approaches in Aircrafts . . . 137

References 138

A Python Codes 149
A.1 Area under Curve . . . 149
A.2 Calculation of Acceleration Components . . . 151

B Recorded Acceleration Data 155

C Published Work 160
C.1 Peer-Reviewed Journal Papers . . . 160
C.2 Refereed Conferences . . . 161

List of Tables

2.1 Summary of Key Aircraft Airflow Distribution and Air Quality Studies . . . 14
2.2 Experimental Techniques Used in Aircraft Cabin Airflow and Air Quality Studies 19
2.3 Categories of Numerical Turbulence Models Used for Airflow and Air Quality Studies 24

3.1 List of Boundary and Initial Conditions Used in the Model 30

4.1 FB and NMSE Values for the Numerical Predictions 40
4.3 Airflow Velocities in the Cabin between Experiment and Numerical Predictions 43

5.1 Exposure Ratios at the Two Monitoring Locations between Different Parametric Sensitivity Cases and the Baseline Steady Level Flight Case 72

6.1 Ratio of Passenger Exposure between Climb and Descent Cases under Aircraft Normal Operating Conditions and the Baseline Steady Level Flight Case . . 80
6.2 Airflow Circulation Values and Changes 86
6.4 Exposure Ratios at the Two Monitoring Locations for Different Flight Legs . 96

7.1 Exposure Ratios at the Two Monitoring Locations between Different Parametric Sensitivity Cases and the Baseline Climb Case under Aircraft Extreme Operating Conditions 120

8.1 Passenger Exposure Ratios to the Airborne Expiratory Particles between the Climb Leg Under Extreme Conditions and the Steady Level Flight Leg . . . 127

List of Figures

2.1 Aircraft Ventilation Systems 11

3.1 The Simulated Cabin Model 31

4.1 Change of the Normalized SF_6 Concentration with the Simulation Time on Four Grid Levels 37
4.2 Comparison between the Experimental and Numerical Normalized SF_6 Concentration with the Simulation Time Using Different Turbulence Models . . . 41

5.1 Airflow Redirection Angles in 2-D and 3-D 46
5.2 Predicted SF_6 Concentration Time Series During the Steady Level Flight Leg Using the Default, 20°, and 30° Airflow Supply Angles 48
5.3 Predicted SF_6 Concentration Time Series During the Steady Level Flight Leg Using the Default and 60° Airflow Supply Angles 49
5.4 SF_6 Concentration Contour Plots During Steady Level Flight at 350 s Using Airflow Supply Angles $\alpha = 20°$ and $\alpha = 60°$ 50
5.5 Predicted SF_6 Concentration Time Series During the Steady Level Flight Leg Using Supply Angles $\alpha = 20°$ and $\beta = 20°$ (to Front and Back) 51
5.6 SF_6 Concentration Contour Plots During Steady Flight at 350 s Using Airflow Supply Angles $\beta = 20°$ to the Front and $\beta = 20°$ to the Back 52
5.7 Predicted SF_6 Concentration time Series During the Steady Level Flight Leg Using 100% More, 50% More, and 50% Less Supply Airflow Rates with respect to the Original Steady Level Flight Flow Rate 54
5.8 SF_6 Concentration Contour Plots During Steady Flight at 350 s Using 100% More Airflow Rate, 50% More Airflow Rate, and 50% Less Airflow Rate . . . 56
5.9 The Two Cough Orientations Used in the Current Study 58
5.10 Predicted SF_6 Concentration Time Series During the Steady Level Flight Leg Using the 30° Downwards, 40° Downwards, and 30° Upwards Cough Direction Angles 58
5.11 SF_6 Concentration Contour Plots During Steady Flight at 350 s Using Cough Direction Angle $\theta = 30°$ Downwards and Cough Direction Angle $\theta = 30°$ Upwards 60
5.12 Predicted SF_6 Concentration Time Series During the Steady Level Flight Leg Using the 20 m s^{-1} and 5 m s^{-1} Cough Release Velocities 62

5.13 SF_6 Concentration Contour Plots During Steady Flight at 350 s Using 5 m s^{-1} Cough Velocity, 20 m s^{-1} Cough Velocity, and 10.6 m s^{-1} Cough Velocity . 65
5.14 Predicted SF_6 Concentration Time Series During the Steady Level Flight Leg Using the 21.2 m s^{-1} Cough Release Velocity for 0.5 Second Duration and The SF_6 Contour Plot at Passenger Breathing Level at 350 s for the Same Case . 67
5.15 New Cougher Locations with respect to the Original Location 68
5.16 Predicted SF_6 Concentration Time Series During the Steady Level Flight Leg with the Cougher Moved to the Center Row on the Left Side of the Cabin . 68
5.17 Predicted SF_6 Concentration Time Series During the Steady Level Flight Leg with the Cougher Moved to the Front Row on the Right Side of the Cabin . 69
5.18 SF_6 Concentration Contour Plots During Steady Flight at 350 s with the Cougher Located at the Center Row on the Left Side of the Cabin and with the Cougher Located at the Front Row on the Right Side of the Cabin . . . 70

6.1 Quantified Vertical and Horizontal Acceleration Components Using Second Order Regression of Data 77
6.2 Comparison of the Predicted SF_6 Concentration Time Series between the Steady Level Flight Case and the Climb Case under the Aircraft Normal Operating Conditions 78
6.3 Comparison of the Predicted SF_6 Concentration Time Series between the Steady Level Flight Case and the Descent Case under the Aircraft Normal Operating Conditions 79
6.4 Airflow Velocity Vectors Near the Aircraft Cabin Wall 84
6.5 Airflow Circulation on the $x - y$ Plane and its Four Quadrant Corners . . . 85
6.6 Concentration Contour Plots of SF_6 During Steady Level Flight 90
6.7 Concentration Contour Plots of SF_6 During Climb under Aircraft Extreme Operating Conditions 92
6.8 Concentration Contour Plots of SF_6 During Descent under Aircraft Extreme Operating Conditions 95
6.9 Predicted SF_6 Concentration Time Series for the Three Flight Legs Investigated; steady level flight, climb and descent legs under aircraft extreme operating conditions 97

7.1 Predicted SF_6 Concentration Time Series for the Steady Level Flight Leg and Climb Leg under Aircraft Extreme Operating Conditions Using the Default, 20°, and 30° Airflow Supply Angles During Climb 103
7.2 Predicted SF_6 Concentration Time Series for the Steady Level Flight Leg and Climb Leg under Aircraft Extreme Operating Conditions Using the Default and 60° Airflow Supply Angles During Climb 104
7.3 SF_6 Concentration Contour Plots During Climb Leg under Aircraft Extreme Operating Conditions at 350 s Using Airflow Supply Angles $\alpha = 30°$ and $\alpha = 60°$ 105

7.4 Predicted SF_6 Concentration Time Series for the Steady Level Flight Leg and Climb Leg under Aircraft Extreme Operating Conditions Using Supply Angles $\alpha = 30°$ and $\beta = 30°$ (to Front and Back) During Climb 106
7.5 SF_6 Concentration Contour Plots During Climb Leg under Aircraft Extreme Operating Conditions at 350 s Using Airflow Supply Angles $\beta = 30°$ to the Front and $\beta = 30°$ to the Back 107
7.6 Predicted SF_6 Concentration time Series between the Steady Level Flight Leg and Climb Leg under Aircraft Extreme Operating Conditions Using 100% More, 50% More, and 50% Less Supply Airflow Rates with respect to the Original Climb Flow Rate 108
7.7 SF_6 Concentration Contour Plots During Climb Leg under Aircraft Extreme Operating Conditions at 350 s Using 100% More Airflow Rate, 50% More Airflow Rate, and 50% Less Airflow Rate 110
7.8 Predicted SF_6 Concentration Time Series for the Steady Level Flight Leg and Climb Leg under Aircraft Extreme Operating Conditions Using the 30° Downwards, 40° Downwards, and 30° Upwards Cough Direction Angles During Climb 111
7.9 SF_6 Concentration Contour Plots During Climb Leg under Aircraft Extreme Operating Conditions at 350 s Using Cough Direction Angle $\theta = 30°$ Downwards and Cough Direction Angle $\theta = 30°$ Upwards 113
7.10 Predicted SF_6 Concentration Time Series for the Steady Level Flight Leg and Climb Leg under Aircraft Extreme Operating Conditions Using the 20 m s^{-1} and 5 m s^{-1} Cough Release Velocities During Climb 114
7.11 SF_6 Concentration Contour Plots During Climb Leg under Aircraft Extreme Operating Conditions at 350 s Using 5 m s^{-1} Cough Velocity, 20 m s^{-1} Cough Velocity, and 10.6 m s^{-1} Cough Velocity 116
7.12 Predicted SF_6 Concentration Time Series for the Steady Level Flight Leg and Climb Leg under Aircraft Extreme Operating Conditions with the Cougher Moved to the Center Row on the Left Side of the Cabin During Climb 117
7.13 Predicted SF_6 Concentration Time Series for the Steady Level Flight Leg and Climb Leg under Aircraft Extreme Operating Conditions with the Cougher Moved to the Front Row on the Right Side of the Cabin During Climb . . . 118
7.14 SF_6 Concentration Contour Plots During Climb Leg under Aircraft Extreme Operating Conditions at 350 s with the Cougher Located at the Center Row on the Left Side of the Cabin and with the Cougher Located at the Front Row on the Right Side of the Cabin 119

8.1 Comparison of the Volume-averaged Particle Concentration in the Cabin with Simulation Time between the Climb Leg under Aircraft Extreme Operating Conditions and the Steady Level Flight Leg for the Three Particle Sizes Studied 126

B.1 Vertical Acceleration Component of a Passenger Aircraft During Take-off and Climb under Normal Operating Conditions (Recorded by Volunteer A) . . . 156

B.2 Vertical Acceleration Component of a Passenger Aircraft During Descent and Landing under Normal Operating Conditions (Recorded by Volunteer A) . . 157
B.3 Vertical Acceleration Component of a Passenger Aircraft During Take-off and Climb under Normal Operating Conditions (Recorded by Volunteer B) . . . 158
B.4 Vertical Acceleration Component of a Passenger Aircraft During Descent and Landing under Normal Operating Conditions (Recorded by Volunteer B) . . 159

List of Abbreviations

ACH	Air Changes per Hour
AMDAR	Aircraft Meteorological Data Relay
AR	Aspect Ratio
ASHRAE	The American Society of Heating, Ventilating, and Air Conditioning Engineers
CDA	Continuous Descent Approach
CEV	Cough Expiratory Volume
CFD	Computational Fluid Dynamics
CPFR	Cough Peak Flow Rate
DAQ	Data Acquisition
DEHS	Di-ethyl-hexyl-sebacat
DES	Detached Eddy Simulation
DNS	Direct Numerical Simulation
DRW	Discrete Random Walk
ECS	Environmental Control System
ETS	Environmental Tobacco Smoke
FAA	U.S. Federal Aviation Administration
FB	Fractional mean Bias
GCI	Grid Convergence Index
GIT	Grid Independence Test
HEPA	High Efficiency Particulate Arrestance
HSA	Hot-Sphere Anemometer
HVAC	Heating, Ventilating, and Air Conditioning

HWA	Hot-Wire Anemometer
IMI	Interferometric Mie Imaging
LBM	Lattice-Boltzmann Method
LES	Large Eddy Simulation
Nd:YAG	Neodymium-doped Yttrium Aluminum Garnet
NMSE	Normalized Mean Square Error
NOAA	U.S. National Oceanic and Atmospheric Administration
OPC	Optical Particle Counter
PBL	Planetary Boundary Layer
PCR	Polymerase Chain Reaction
PIV	Particle Image Velocimetry
PLIF	Planar Laser-Induced Fluorescence
ppb	Parts per billion
ppbv	Parts per billion by volume
ppm	Parts per million
ppmv	Parts per million by volume
PTR-MS	Proton-Transfer-Reaction Mass Spectrometry
PV	Personalized Ventilation
RANS	Reynolds-averaged Navier Stokes
RH	Relative Humidity
RNG	ReNormalization Group
SARS	Severe Acute Respiratory Syndrome
SGDH	Standard Gradient Diffusion Hypothesis
SST	Shear Stress Transport
UA	Ultra-sonic Anemometer
VOC	Volatile Organic Compound
VPTV	Volumetric Particle Tracking Velocimetry

List of Mathematical Symbols

Latin Symbols

a	Acceleration
a_h	Aircraft Horizontal Acceleration Component
a_v	Aircraft Vertical Acceleration Component
A	Aircraft Wing Surface Area / Cross-sectional Area of the Cougher's Mouth
c_p	Specific Heat at Constant Pressure
C	Contaminant Concentration / Courant Number
C_o	Observed (Measured) Concentration
C_p	Predicted (Calculated) Concentration
D	Drag / Diffusion Coefficient
D_m	Mass Diffusion Coefficient
D_T	Thermal Diffusion Coefficient
F	Force
F_s	Factor of Safety for GCI Calculations
g/G	Gravitational Acceleration (9.81 m s^{-2})
G_k	Generation or Consumption of Turbulence Kinetic Energy Due to the Mean Velocity Gradients
G_b	Generation or Consumption of Turbulence Kinetic Energy Due to Buoyancy
h	Sensible Enthalpy / Grid (Mesh) Spacing
H	Height
J	Diffusion Flux
k	Turbulent Kinetic Energy / Lift-induced Drag Constant / Thermal Conductivity

k_{eff}	Effective Thermal Conductivity
k_t	Turbulent Thermal Conductivity
L	Lift / Length
m	Mass / Grid Refinement Level
M	Contaminant Mass
Ma	Mach Number
n	Nano / Grid Refinement Level
N	Number
p	Order of Convergence / Static Pressure
Pr_t	Turbulent Prandtl Number
r	Mesh Refinement Ratio
S	Source Term
Sc_t	Turbulent Schmidt Number
t	Time
T	Thrust / Temperature / Cough Time
T_{ref}	Reference Temperature
V	Velocity / Volume
W	Weight / Width
x	Distance / Coordinate
y	Distance / Coordinate
Y	Mass Fraction
z	Distance / Coordinate

Greek Symbols

α	Ventilation Airflow Supply Angle (in 2-D)
β	Ventilation Airflow Supply Angle (in 3-D)
Γ	Airflow Circulation
ε	Turbulent Dissipation Rate
ϵ	Relative Error

θ	Cough Inclination Angle
Θ	Aircraft Inclination Angle / Flight Path Angle
μ	Micro / Dynamic Viscosity
μ_t	Turbulent Viscosity
π	The Ratio of the Circumference of a Circle to Its Diameter (≈ 3.14)
ρ	Density
τ	Stress
Φ	Numerical Solution
ω	Specific Turbulent Dissipation Rate

Chapter 1

Introduction

Air travel has become one of the main pillars of the present globalized economy. It is estimated that more than 4.1 billon people used air travel for long-range transport in 2017 supporting about 10.2 million job opportunities in the aviation sector alone, with projected further annual increases [1]. The environment inside a commercial aircraft cabin provides a fertile ground for deterioration of air quality, disease transmission, and infection spreading among passengers if proper measures are not taken [28]. This is attributed to the high occupant density, wide range of passenger activity, and the inability of passengers to leave this closed space for prolonged periods of time [10]. On the other hand, disease transmission from a passenger or group of passengers to others can also occur off-board of aircraft, either before or after flights. This further complicates the task to assess aircraft cabin initiated infections and air quality issues [64].

In recent years, a wide range of symptoms and transmissible diseases due to poor air quality, inefficient ventilation systems, and improper contaminant control measures have been reported during aircraft flights, and sometimes after them. The symptoms and diseases range from nausea, dizziness, headaches and fatigue [43] to highly infectious epidemics such as Influenza A (H5N1 and H1N1), Severe Acute Respiratory Syndrome (SARS), and Tuberculosis. These diseases have infected large numbers of people, either aboard or off-board of aircraft and are the main cause of many mortality cases in the past few years [6, 74, 84, 85].

Different infectious diseases aboard aircraft have different modes of transmission compared to other closed spaces. Influenza, for example, is known to have three main modes of transmission, namely: airborne mode, droplet mode and contact mode of transmission [11, 84, 95]. Among these modes, the airborne route has gained a lot of attention in air quality studies in the last two decades. This is mainly attributed to the very small contaminant

aerosols and expiratory particles that can remain airborne in the space for extended times and distances, which significantly increase the probability of exposure and/or infection when compared to the other modes [6].

Many measures for controlling and improving air quality in aircraft cabins have been investigated in the literature. Aboard aircraft, ventilation and air circulation systems are capable of controlling air temperature, air velocity, and airborne pollutant dispersion resulting in the best possible indoor air quality. This is to maintain a clean and convenient environment for passengers by decreasing the amount of gaseous and particulate pollutants to levels below the permitted levels [60]. Despite this, infection rates can be accelerated in some cases with the uncontrolled use of ventilation and HVAC systems [11]. More broadly, aboard commercial aircraft, the Environmental Control System (ECS) provides air supply, thermal control, humidification and dehumidification, and cabin pressurization for the crew and passengers. Airflow recirculation, filteration, avionics cooling, smoke detection, and fire suppression are also usually considered part of an aircraft's ECS [10].

1.1 Motivation

The current study is motivated by the large number of studies in the literature that utilized different research approaches to investigate air quality in aircraft cabin environments by using air distribution systems as a control measure. These approaches range from purely experimental [43, 82, 94, 98] to entirely computational (or numerical) [27, 58, 108, 112], or combination of both [14, 37, 76, 101].

In spite of the extensive span of available studies in the literature, very few of those studies have systematically evaluated the exposure or infection risk of the occupants to airborne contaminant released from expiratory events, such as exhalations, coughs, and sneezes [35, 79]. Furthermore, less studies used and proposed airflow design strategies as means for mitigation utilizing limited approaches [42].

The study is also motivated by the fact that passenger aircraft are moving with high speeds and accelerations accomplishing distinct flight mission legs (or intervals) with different dynamic conditions, such as takeoff, climb, cruise, descent, and landing [47]. Despite that, no study in the literature, to the best of the author's knowledge, has considered the effect of the acceleration-induced body forces on the ventilation airflow patterns and contaminant dispersion behavior inside aircraft cabins.

The mentioned research gaps and others are filled in the current study as detailed later

in section 2.6.

1.2 Contributions to the Scientific Field

The current study effectively contributes to the scientific field concerned with investigating the ventilation airflow patterns and air quality conditions inside aircraft cabins in various ways.

First, the study closes the gap in the literature analogy of considering that aircraft are always at rest or under cruise conditions affected only by gravitational acceleration. This is achieved by introducing the acceleration-induced body forces and investigating their influence on airflow patterns and contaminant dispersion behavior in the cabin during different flight legs and under different flight conditions.

Second, the study provides in-depth analysis to the airflow patterns and structures in the cabin under the influence of body forces using airflow velocity, boundary layer separation from cabin walls, and airflow circulation as parameters. Those airflow patterns primarily act as the cause of the dissimilar airborne contaminant dispersion behavior in the passenger aircraft cabins for different flight legs and conditions. Such influence can be carefully analyzed and reverse-engineered to yield efefctive mitigation means for passenger exposure to airborne contaminants aboard passenger aircraft.

Third, the study proposes and applies novel and improved airflow design strategies and novel source control strategies for mitigating passenger exposure to the expiratory airborne contaminant in the passenger aircraft cabins. Those strategies can prove to be very practical and effective for commercial airliners to reduce passenger exposure and infectivity aboard their flights.

1.3 Thesis Structure

After this introductory chapter, there are eight more chapters in this thesis. Chapter 2 presents and analyzes the literature review in the field followed by the investigated research gaps in the current study and its objectives. Chapter 3 illustrates the aircraft cabin model created and modelled in this study, and provides the governing equations solved by the numerical solver ANSYS Fluent. Chapter 4 sheds the light on the process adopted for creating the grid (mesh) for the cabin model, the grid independence tests performed, and the validation of the model against experimental data from the literature. Chapter 5 discusses the very

first part of the results for the current study. This chapter is concerned with investigating the effect of the airflow design and source control strategies, previously mentioned, on reducing the passenger exposure to the cough-released contaminant during the steady level flight leg. Chapter 6 investigates the effect of the acceleration-induced body forces on the cough-released contaminant dispersion behavior in the aircraft cabin during the climb and descent legs subjected to normal and extreme aircraft operating conditions. The chapter investigates the influence of the acceleration-induced body forces during the passenger aircraft climb and descent under the normal operating conditions on the contaminant dispersion behavior in the aircraft cabin. Additionally, the effect of the body forces during the extreme operating condition of a gusty flight on the contaminant dispersion behavior and the ventilation airflow patterns in the cabin is studied in the same chapter. Chapter 7 discusses the capacity of the same ventilation airflow design and source control remedial strategies investigated in Chapter 5 to mitigate the increased passenger exposure to the airborne contaminant in the cabin space during the climb leg under the extreme aircraft operating condition of flying through gusts. Chapter 8 conducts a comparison of the particulate contaminant (or particles) dispersion behavior in the simulated aircraft cabin between the steady level flight leg and climb leg under aircraft extreme operating conditions. This is to complement the findings of the study using the gaseous SF_6 contaminant surrogate. Finally, Chapter 9 presents the overall conclusions for the current thesis, sheds the light on further research gaps that were not fully addressed in the current study, highlights the merits and limitations of the current study, and presents future research topics, which can be used as a reference for the future studies in the field.

Chapter 2

Literature Review and Objectives

In this chapter, studies concerned with air quality and contaminant management aboard aircraft in the past two decades are reviewed. The types of the airborne contaminants studied and the effect of different ventilation techniques adopted in regulating them are among the topics addressed. Additionally, recommendations are provided on the most appropriate approaches and practices for air quality research in aircraft cabins. The chapter ends with highlighting the investigated knowledge gaps in the literature and the objectives of the current study.

2.1 Airborne Contaminants Aboard Aircraft

The types of airborne contaminants that occupants encountered in aircraft cabins include odors generated from gaseous contaminants such as galleys and lavatories' effluents, pyrolyzed engine oil and hydraulic fluid, disinsection sprays, and other odourless and Volatile Organic Compounds (VOCs), and particulate contaminants. The particulate pollutants are either generated from human expiratory activities such as breathing, coughing, and sneezing, or other non-expiratory sources such as human skin shedding, dust contamination, and smoking (where permitted). Many studies have investigated the characteristics of particles originated from expiratory human activities and their spread in indoor spaces in the last century [31, 63, 70, 75, 114]. Coughing was and still is the most studied source for droplet generation, as it produces large amounts of droplets with elevated discharge velocities [39]. In the following subsections, the studies concerned with airborne contaminants in aircraft cabin environments are discussed.

2.1.1 Gaseous Contaminants

Studying the behavior of gaseous contaminants in closed spaces, and especially aircraft cabins, started long after the beginning of the research on dispersion of droplet media in air by medical experts in the mid 1930s and 1940s [26, 96, 97]. This is attributed to the relative simplicity of the investigation tools for particle media. However, the lack of adequate technologies to release and measure trace gases caused a fifty-year delay in their technology development [43, 94].

The concentrations for various gaseous contaminants found aboard eleven different types of commercial aircraft were measured in cabins during 36 different flights segments by Waters et al. [94]. Flight segments were chosen to obtain a range of flight durations and latitudes. Direct sampling and analysis methods were used under different flight conditions and durations. The concentrations for gaseous contaminants, such as VOCs, nitrogen oxides, carbon monoxide, carbon dioxide (CO_2), aldehydes, ethanol, ozone, and some particulate contaminants and nicotine were measured at two distinctive stations inside the economy section of the cabin: one at the coach front and one at the back. Temperature, relative humidity (RH) and barometric pressure were also monitored for their variations at the same two locations along different flights that ranged in duration from two hours to more than eight hour-long. Researchers found that no gaseous pollutant, except for CO_2, has shown any difference in concentration between the front and the rear stations. It was also noticed that no pollutant exceeded the permissible limits set by Federal Air Regulation standards, or exhibited any specific relation to the aircraft type, size, or route. Carbon dioxide, on the other hand, showed an increasing trend for higher passenger loading on aircraft, aircraft using recirculation ventilation, and shorter flights on smaller aircraft. Nevertheless, no statistical significance was found for any of the relationships made, and contaminants' health-related implications for occupants have not been discussed enough.

Disinsection pesticides are also commonly found as a type of gaseous contaminant aboard many commercial aircraft. Although standard 161-2013 issued by the American Society of Heating, Refrigeration and Air Conditioning Engineers (ASHRAE) strongly recommends the application of pesticides on unoccupied aircraft before boarding [10], these toxic pesticides are sprayed in the occupied passenger cabins by several airlines in compliance with the regulations of some countries, such as India, Panama, Madagascar, Uruguay, and Zimbabwe [88].

There are few studies in literature that have investigated the airborne transport of pesticides in aircraft cabins and their effect on the health of both passengers and crew members.

One study was conducted by Isukapalli et al. [48] who researched the dispersion and deposition of disinsection pesticides in an aircraft cabin using Computational Fluid Dynamics (CFD) simulations. The model was validated against some spraying experiments in a similar cabin mockup for a limited number of passenger seats. Different spraying techniques were used to apply the pesticide; either on each side of the cabin or in the overhead section. Cabin ventilation was investigated as the sole mechanism for pesticide spread and deposition in the cabin with air exchange rate switched from low to high, and vice versa. The deposition on cabin surfaces (seats and passengers) was found to decrease to about one half when air exchange rate was increased from 1 to 29 ACH, with both deposition values less than the permitted threshold. Moreover, an increase in pesticide concentration was noticed at some areas along the aisle and at the center of the cabin as compared to other areas, which can be attributed to the air flow pattern. On the other hand, the study overlooked the exposure of occupants to the sprayed pesticides, and the possible health risks.

Ethanol, ozone, and ozone-initiated chemistry products are among the toxic yet odorless pollutants that usually exist in aircraft cabin environments. Ethanol is introduced in the cabin by the wet wipes traditionally presented with meals aboard aircraft. Ozone, on the other hand, is a naturally occurring component in the atmosphere, which increases substantially at higher altitudes typical for commercial aircraft cruises (around 35,000 feet or more above sea level) to levels surpassing 100 parts per billion by volume (ppbv) in some cases [12].

The most cost-effective method suggested in the literature to reduce ozone-initiated compounds in the cabin is the use of a proper ventilation strategy with some specific ratios of outdoor to recirculated air. However, more outdoor air may result in more ozone entering the cabin, and consequently more compounds developed from its transformation [99]. Another effective technique is the use of ozone catalytic units and/or air purifiers. Different types of photocatalytic air purifiers were proved helpful for reducing in-cabin ozone and ethanol concentrations significantly [12, 98]. It is required by the U.S. Federal Aviation Administration (FAA) that an ozone catalytic converter be equipped by any aircraft flying on routes where ozone exposure is expected to be significant [10, 86].

Environmental conditions (temperature, pressure, and relative humidity) inside airliner cabins have also been investigated for their effects on gaseous contaminant concentrations and related symptoms experienced by occupants. In a study by Strøm-Tejsen et al. [81] performed in a full-scale Boeing 767 aircraft cabin mockup, the fresh air supply was varied from 1.4 L s^{-1} to 9.4 L s^{-1} per person, leading to a change in Relative Humidity (RH)

from 28% to 7%, correspondingly. Throughout each simulated 7-h flight, cabin occupants were asked to answer some set of questions three times to give their assessment of the air quality and to report any experienced symptoms and their intensity. It was concluded that raising the RH percentage in the cabin by lowering the fresh air supply, and especially to the minimum value of 1.4 L s^{-1}, does not reduce the symptoms usually associated with flights and sick building syndrome (SBS), but intensify them. The elevation of these symptoms, such as headache, wooziness and distress, at this low ventilation rate and high RH condition is mainly attributed to the increased concentration of contaminants in the cabin.

2.1.2 Particulate Contaminants

Expiratory Particulates from Human Activities

The number of studies that investigated the generation and dispersion of particles originated from human expiratory activities in aircraft cabin environments is limited in comparison to the studies performed in rooms and other confined spaces.

Wan et al. [90] performed an experimental investigation for the dispersion behavior of expiratory droplets released from a droplet generator (mimicking a coughing person) in a Boeing 767 aircraft cabin mockup. The researchers found that droplet dispersion was suppressed when the injection point was closer to the cabin wall, and when the ventilation air supply rate was increased at lower RH.

A later experimental study was performed by Sze To et al. [82] using the same cabin setup to investigate the dispersion of cough droplets and their deposition on the cabin surfaces. For this purpose, the Particle Image Velocimetry (PIV) and the Interferometric Mie Imaging (IMI) techniques were utilized. Following this work, a numerical simulation study [91] was performed, which added the infection risk associated with the droplets to the studied parameters. The investigated range of initial droplet sizes before evaporation into nuclei for both studies was between 2 and 225 µm. It was found that when the coughing person was placed near the wall to the side, very limited number of droplets were capable of dispersing to the other side of the cabin. Additionally, supplying ventilation air with a higher rate caused enhanced dilution of the droplets, but also improved their dispersion in the cabin. If the pathogens encountered in the aircraft cabin are highly infective, it was speculated that a high ventilation airflow rate may lead to more infections. However, if the pathogens have low infectivity, the higher airflow rate may reduce the number of infected passengers.

Using a different approach, J. K. Gupta conducted a series of studies on expiratory

droplets release and transport, their inhalation by passengers surrounding the infected person, and assessment of the airborne infection risk associated in aircraft cabins [40–42]. Three expiratory activities for the infected person were simulated using CFD methods, namely: breathing, coughing, and talking, with uniform droplet sizes of 0.4, 8.5, and 30 µm, respectively. It was found that the droplets released from the cough of one patient passenger followed the bulk ventilation air in the cabin. Moreover, as the amount of exhaled droplets from the cough(s) of one or more passengers increased, the risk to other passengers in the aircraft cabin also increased if those droplets carried live infectious agents.

Numerous medical studies and reviews also investigated the transmission mechanics of some of the most common infectious diseases by expiratory particles and the associated infection risk in aircraft cabin environments [64, 74, 89]. Those studies majorly agreed on that the environmental conditions aboard passenger aircraft cabins provide a suitable habitat for the dispersion and transmission of contaminants and infective pathogens from one passenger or crew member to the others. To counter that risk, control measures and safety precautions were suggested by the researchers. Examples for such measures and precautions are: using the Environmental Control System (ECS) aboard passenger aircraft (and mainly ventilation strategies) to contain the spread of airborne pathogens, regular cleaning of aircraft cabins, and isolating the patients who travel in the economy section of the cabin on long flights.

Non-expiratory Particulates

Contaminant particulates originating from non-expiratory sources inside aircraft cabin environments have been considered very rarely in the literature. The main sources of non-expiratory particles in aircraft cabins are smoking, human skin shedding, and dust contamination released from the clothing of the occupants and the furniture. Skin shedding and dust contamination sources inside aircraft cabins have been overlooked in the literature, probably because the concentration of such contaminants is too low inside the cabins to pose a health risk on the occupants. On the other hand, smoking, aboard some air flights that still permit so, has been considered by few researchers, and the concentrations of the produced nicotine-containing particles and Environmental Tobacco Smoke (ETS) have been measured.

Dechow et al. [23] measured the particle concentrations using counters set in the first class, the non-smokers section, and the smokers section of the economy-class aboard different Airbus A310 and A340 aircraft. Nicotine-containing particles, released from smoking, showed an elevated concentration of 26 ppb in the smoking section of the cabin, while it remained at a very low level 0f 0.2 ppb in the non-smoking sections. The concentrations

also exhibited temporal variations depending on the status of the smokers during the flight (awake, awake and smoking, sleeping, etc.). A similar result was reported by Drake and Johnson [25] when they conducted some measurements for nicotine and respirable particles aboard four different models of Boeing 747 aircraft during flight using mobile measurement devices. They found that all-daytime flights exhibited a greater concentration of environmental tobacco smoke than night-time flights, but exact numbers for those concentrations were not provided by the authors. Waters et al. [94] measured the concentration of respirable particles and smoking-generated nicotine-containing particles aboard six smoking-permitted flights. They found that the average concentration of inhalable particles (<30 µm in diameter) was almost the same between smoking and non-smoking flights with 0.119 µg L^{-1} and 0.123 µg L^{-1}, respectively. However, the mean concentration of total particles (inhalable and non-inhalable) in the cabin was higher aboard smoking-permitted flights than non-smoking flights with 0.11 µg L^{-1} and 0.08 µg L^{-1}, respectively.

In its most recent standard 161-2013 (Air Quality within Commercial Aircraft), ASHRAE necessitates installing High Efficiency Particulate Arrestance (HEPA) filters on all recirculated air inlets aboard all operating aircraft, and maintaining them according to the best practices specified by the manufacturer. Those filters can remove expiratory and non-expiratory particles, viruses and bacteria down to 0.3 µm in size with an efficiency up to 99.97% [10].

2.2 Aircraft Ventilation Strategies and their Effect on Air Quality and Airborne Infection Aboard

Different ventilation strategies have been investigated as measures to control infection transmitted via airborne route and other gaseous and particulate contaminants commonly found in the aircraft cabin envelop. Basically, the efficiency of each ventilation system is measured based on the ventilation effectiveness it provides. For aircraft cabins, ventilation effectiveness is defined as the ratio of the outside fresh air supplied to the cabin that reaches the breathing zone of the occupants [10]. In this section, major studies that examined the effect of one or more ventilation system, such as mixing, displacement, and personalized ventilation, on air quality and disease spread aboard aircraft are discussed. Figure 2.1 shows schematics for the three main aircraft ventilation systems.

Mixing ventilation is the primary technique used to provide a mixture of outside fresh air

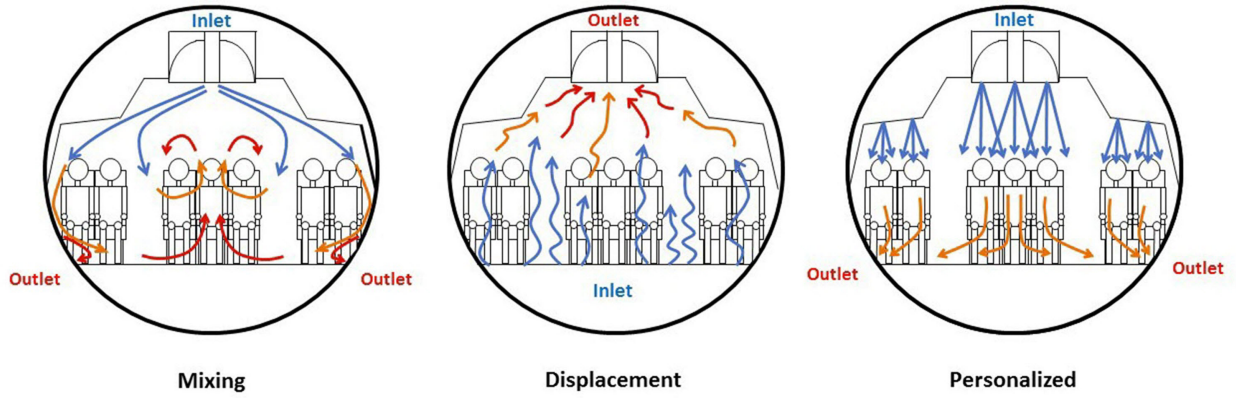

Figure 2.1: Aircraft Ventilation Systems.

and recirculated air from the cabin, with different ratios, to the aircraft occupants after being filtered. Air usually enters at specified volumetric rates from supply inlets located above or below the overhead luggage compartment in the cabin depending on aircraft type. It then circulates through the cabin under the influence of inertia and buoyancy forces induced by the thermal plumes from the occupants' bodies [59] and exits through the exhaust slots found at the floor level on the two sides of the cabin. This ventilation strategy creates a well-mixed environment that helps dilute and disperse infectious organisms and contaminants within the cabin [106, 110].

Zhang et al. [111] noticed that the mixing air motion generated by the Environmental Control System (ECS) inside a cabin mockup affected both the released gaseous and particulate pollutants' movement and enhanced their spread. Rydock [79] found that the proximity of the infecting person(s) to other occupants has more influence on disease spread than partial air recirculation in the diluted cabin scenario created by the well-mixed condition. A novel localized exhaust technique was proposed by Dygert and Dang [27] to be used in conjunction with mixing ventilation in the cabin. The setup consists of two air suction ports installed in the back of each seat and around the head of a sitting occupant, and was found to provide an average decrease of 40 to 50% in individual exposure risk to airborne infection from surrounding passengers.

Displacement ventilation was proposed and investigated as an alternative air supply strategy to the overall mixing scenario within the aircraft cabin space. Under-aisle and underfloor ventilation systems are usually used as other names for the displacement ventilation

system aboard aircraft. In such systems, air is supplied vertically from an under-floor plenum, usually located under the aisles, through perforated or nozzle vents. Supplied cool air heats as it travels up the height of the cabin due to the surrounding thermal loads primarily released from occupants' bodies. The buoyancy effect causes stratification, and the warm air is eventually removed through the exhaust vents located at the ceiling. Meanwhile, the different contaminants are trapped by this rising warm air in a thick layer close to the ceiling waiting to be pushed out of the cabin through the exhaust vents by clean air coming from below. Although this ventilation scenario significantly reduces the dilution of pollutants in the cabin air, the trapped contaminants in the upper air layer are not far from the breathing level of occupants and may pose health risks.

An under-floor displacement air distribution system was employed by Zhang and Chen [105] in a CFD model for a section of a Boeing 767 airliner cabin. It was observed that slight air mixing occurs at the center seats, which indicates that the possibility for contaminant spread and cross-infection exists to some extent with displacement ventilation. Zhang et al. [108] performed a numerical simulation for an enhanced displacement air distribution system in a section of a wide-body passenger airliner cabin. The novel displacement system was found to decrease the (CO_2) concentration in the cabin by 30% and increasing the relative humidity from 10% to 20% by supplying an amount of 0.05 kg h^{-1} per person of humidification water only.

As a latest addition to the ventilation technology, personalized ventilation has emerged as a high ventilation effectiveness alternative to the overall mixing and displacement air supply systems in different closed spaces [65]. In aircraft cabins, personalized ventilation vents (gaspers) have been installed for decades to act as an auxiliary ventilation system in addition to the existing mixing ventilation in the background. However, for research purposes, personalized ventilation has been recently employed in various forms as a measure to protect the micro-environment of occupants from the intrusion of contaminants and infectious organisms. One main advantage of personalized ventilation over other air supply systems aboard aircraft is that it usually delivers clean outside fresh air directly to the breathing zone of occupants. This helps make the air supplied to occupants free of cabin contaminants.

Aircraft personalized ventilation systems are classified into two categories: proposed and existing systems. Proposed personalized air supply systems had supply inlets installed in each seat armrest [106], in the seat-back in front of each occupant with ceiling exhaust vents [105], or in the seat-back with localized exhaust opening for each passenger located just below the inlet [116]. On the other hand, several studies [22, 33, 52, 102] investigated the use of

the overhead gaspers, commonly found in different models of passenger aircraft, as effective personalized ventilation supply inlets. Studies agreed that personalized ventilation provides better air quality and protection against contaminants when operated with the ceiling supply mixing system and/or the displacement system than when those systems operate solely. This occurs at the cost of draught risk noticed in some cases, which can be overcome by providing personal control over flow rate, flow direction, and temperature.

2.3 Research Approaches for Studying Airflow Distribution and Air Quality in Aircraft Cabins

Studies concerned with air distribution and quality in aircraft cabins have adopted various approaches. Research approaches range from pure experimental work to numerical simulations validated against experimental measurements, or combination of both. Table 2.1 shows a list of 38 studies performed on airflow distribution and air quality in aircraft cabin environments in the last twenty years. Similar collective tables have been included in other review studies [21, 60], but in the current investigation more and newer studies are considered, and more emphasis on the studied parameters and the used techniques is provided.

Table 2.1: Summary of the key airflow distribution and air quality studies performed in aircraft cabins in the last two decades (from 1999 to 2016).

Study	Aircraft setting	Studied parameter(s)	Experimental technique	Numerical technique
		EXPERIMENTAL		
Haghighat et al. (1999) [43]	Actual in-flight aircraft (Airbus A320, Airbus A340, Boeing 767, DC9)	Temperature, RH and Carbon dioxide concentration	On-board measurement using a portable air sampler	N/A
Waters et al. (2002) [94]	Actual in-flight aircraft (eleven different types)	Temperature, RH and contaminant levels	Direct-Reading Data Logging (DRDLI)	N/A
Rydock (2004) [79]	Actual in-flight Airbus A340	Concentration of tracer gas (SF_6) released as a cough puff	Sample collection using syringes for later analysis	N/A
Wisthaler et al. (2005) [99]	Mockup for a Boeing 767 aircraft cabin	Ozone-initiated products concentrations	Proton-Transfer-Reaction Mass Spectrometry (PTR-MS)	N/A
Strøm-Tejsen et al. (2007) [81]	Mockup for a Boeing 767 aircraft cabin	Effect of RH% on contaminant levels and flight symptoms	In-cabin detection, gas chromatography and mass spectrometry	N/A
Wisthaler et al. (2007) [98]	Mockup for a Boeing 767 aircraft cabin	Effect of using air purifiers on the levels of gaseous pollutants	Proton-Transfer-Reaction Mass Spectrometry (PTR-MS)	N/A
Bhangar et al. (2008) [12]	Actual in-flight aircraft (seven different types)	Ozone concentration in cabin during flight	In-flight sampling with an ozone photometer	N/A
Wang et al. (2008) [92]	Mockup for a Boeing 767-300 aircraft cabin	Ventilation Effectiveness Factor (VEF) and local mean age of air	Volumetric Particle Tracking Velocimetry (VPTV) and gas sampling	N/A
Kühn et al. (2009) [49]	Mockup for an Airbus A380 upper deck cabin	Airflow velocity and temperature fields for two cases of convection	PIV and temperature measurement by Type K thermocouples	N/A
Sze To et al. (2009) [82]	Mockup for a Boeing 767 aircraft cabin	Airflow and cough particles dispersion and deposition	PIV and Interferometric Mie Imaging (IMI)	N/A
Anderson (2012) [8]	Boeing 767 aircraft cabin simulator (mockup)	Effect of using personal gaspers on airflow and contaminants transport	Direct sampling of CO_2 using non-dispersive infrared sensors	N/A
Liu et al. (2012) [61]	Actual parked MD-82 aircraft	Airflow velocity field and cabin geometry to be used for CFD validation	T-scan laser tracking, hot-sphere anemometry, and ultra-sonic anemometry	N/A
Li et al. (2014) [53]	Actual parked MD-82 aircraft	Concentrations of gaseous (SF_6) and particulate (DEHS) contaminants	T-scan laser tracking, hot-sphere anemometry, and ultra-sonic anemometry	N/A

Zhai et al. (2014) [103]	Actual in-flight Boeing 737-800 aircraft	Concentrations of particles and (CO_2) in cabin air supply and return	Direct measurement using an airborne particle counter and (CO_2) detector	N/A
Dai et al. (2015) [22]	Simplified mockup for an aircraft cabin with an actual MD-82 gasper	Gasper-induced airflow velocity and turbulence intensity	Hot-wire anemometry	N/A
Fang et al. (2015) [33]	Mockup for an Airbus A320 aircraft cabin	Effect of using personal air supply ports (gaspers) on thermal comfort	Hot-wire anemometry and regular thermal sensation questionnaires	N/A
Li et al. (2015) [52]	Five-row section within an actual parked MD-82 aircraft	Effect of using gaspers on airflow and gaseous pollutant concentration	Hot-wire and ultra-sonic anemometry and photo-acoustic multi-gas analysis	N/A
Study	Aircraft setting	Studied parameter(s)	Experimental technique	Numerical technique
		NUMERICAL		
Lin et al. (2005) [58]	Numerical model for a Boeing 767-300 cabin section	Airflow patterns and air velocity magnitudes	N/A	RANS and LES simulations using Fluent code
Zhang and Chen (2007) [105]	Numerical partial model for a Boeing 767-300 cabin	Effect of novel ventilation systems on air velocity and (CO_2) concentration	N/A	RANS (RNG k-ε) simulations using Fluent
Wan et al. (2009) [91]	Numerical model for a Boeing 767 cabin section	Airflow and expiratory aerosols dispersion and deposition	N/A	RANS (RNG k-ε) simulations using Fluent with Lagrangian particle tracking
Dygert and Dang (2010) [27]	Numerical model for a Boeing 767 cabin section	Effect of localized exhaust on airborne contaminant removal	N/A	RANS (Realizable k-ε) simulations using a commercial solver
Zhang et al. (2010) [108]	Numerical partial model for a wide-body aircraft cabin	Effect of a new air supply system on airflow and contaminant concentration	N/A	RANS (RNG k-ε) simulations using Fluent
Gupta et al. (2011) [41]	Numerical partial model for a twin-aisle aircraft cabin	Airflow velocity field and transport of expiratory droplets	N/A	RANS (RNG k-ε) simulations using Fluent with Lagrangian particle tracking
Gupta et al. (2012) [42]	Numerical partial model for a twin-aisle aircraft cabin	Risk of infection due to influenza outbreak in a 4-h flight	N/A	RANS simulations using Fluent and a model for infection risk assessment
Liu et al. (2013) [59]	Numerical model for a MD-82 aircraft first-class cabin (empty or occupied)	Prediction of airflow pattern and turbulence by three turbulence models	N/A	RANS (RNG k-ε), LES and DES simulations using Fluent

Hassan (2016) [46]	Numerical partial model for an Airbus A340-600 aircraft cabin	Effect of using modified mixing air supply and gaspers on thermal comfort	N/A	RANS (RNG k-ε) simulations using Fluent
Study	Aircraft setting	Studied parameter(s)	Experimental technique	Numerical technique
NUMERICAL WITH EXPERIMENTAL OR ANALYTICAL VALIDATION				
Garner et al. (2004) [37]	Actual parked Boeing 747-100 aircraft	Airflow distribution and velocity	Three-dimensional sonic anemometry	Developed PICMSS code and the commercial Fluent code
Bosbach et al. (2006) [14]	Mockup for a part of a real aircraft cabin	Airflow turbulence and velocity fields	Particle Image Velocimetry (PIV)	RANS simulations with three turbulence models using Star-CD
Günther et al. (2006) [38]	Mockup for a part of a real cabin and a single-person sleeping bunk	Airflow turbulence and velocity fields	PIV and thermography	RANS simulations with three turbulence models using Star-CD
Yan et al. (2009) [101]	Mockup for a Boeing 767-300 aircraft cabin	Airflow pattern and airborne pollutant dispersion	VPTV and (CO_2) sampling using infrared sensors	RANS (Standard k-ε) simulations using Fluent
Zhang et al. (2009) [111]	Mockup for a half-occupied aircraft cabin	Air velocity and temperature, and gaseous and particulate pollutants dispersion	Ultrasonic anemometry, photoacoustic analysis and optical particle sizing	RANS (RNG k-ε) simulations using Fluent with Lagrangian particle tracking
Poussou et al. (2010) [76]	One-tenth scale aircraft cabin mockup	Effect of a moving body on airflow and contaminant transport	PIV and Planar Laser-Induced Fluorescence (PLIF)	RANS (RNG k-ε) simulations using Fluent
Zítek et al. (2010) [116]	Single seat experimental mockup and a sectional CFD Cabin model	Effect of a new personal ventilation system on air velocity and RH	PIV and airflow visualization using SAFEX fog	RANS (Standard k-ε) simulations using Fluent
Gupta et al. (2011) [40]	Numerical partial model for a twin-aisle aircraft cabin (semi-analytical validation)	Transport and inhalation of droplets generated from different expiratory events	N/A	RANS (RNG k-ε) simulations using Fluent with Lagrangian particle tracking
Zhang et al. (2012) [106]	Mockup for a twin-aisle aircraft cabin	Effect of a new personal ventilation system on cross-contamination	Ultra-sonic anemometry and direct (CO_2) sampling	RANS (RNG k-ε) simulations using Fluent
Isukapalli et al. (2013) [48]	Mockup for a Boeing 767 aircraft cabin	Dispersion and deposition of disinsection pesticides in cabin	Gas chromatography and mass spectrometry	RANS (RNG k-ε) simulations using Fluent
Li et al. (2016) [54]	Numerical partial model for a Boeing 737-200 aircraft cabin	Effect of airflow vortex structure on airborne contaminant transport	PIV, hot-wire and ultrasonic anemometry, and infrared thermal imaging	RANS (RNG k-ε) simulations using Fluent
You et al. (2016) [102]	Simplified aircraft cabin mockup	Gasper-induced airflow velocity and temperature distributions	PIV and hot-sphere anemometry	RANS (RNG k-ε and SST k-ω) simulations using Fluent

Out of the 38 studies, seventeen studies had only experimental work performed, while nine had pure numerical simulations validated by experimental data from other studies. Twelve studies did experimental measurements or analytical calculations to validate the numerical models created by one or more of the authors. Generally, all possible approaches of research have been used to investigate airflow characteristics and air quality in aircraft cabins.

Most studies that mimicked aircraft cabins, either in the form of experimental mockups or numerical models, used the actual dimensions and configurations for cabins as much as possible. However, it is essential to compare the airflow patterns between a mockup or model and a real cabin to assess the differences caused by simplifications [19].

Numerous experimental measurement techniques have been employed in the surveyed studies. Those techniques can be classified into two main categories: 1) flow measurement techniques, and 2) species or contaminants measurement techniques. Examples for the first category are: Particle Image Velocimetry (PIV), Planar Laser-Induced Fluorescence (PLIF), and fog or dye flow visualization. For the second category, detectors, lab analysis methods, such as chromatography and mass spectrometry, Proton-Transfer-Reaction Mass Spectrometry (PTR-MS), and the Interferometric Mie Imaging (IMI) techniques are some examples.

Conversely, the numerical simulation techniques and tools used for airflow and air quality investigations in aircraft cabins were limited. The codes, or software, used for simulations were mainly commercial, such as Fluent or Star-CD, with Fluent being used in about 90% of the investigated studies. Different turbulence models have been employed in the surveyed studies, such as Reynolds-Averaged Navier-Stokes (RANS), Large Eddy Simulation (LES), or Detached Eddy Simulation (DES) models.

2.4 Best Practices for Aircraft Airflow and Air Quality Research

There is no unique research approach, or set of research practices, that is most suitable for all aircraft airflow and air quality studies. This is attributed to the distinctive characteristics that each aircraft airflow and/or air quality research study possess.

In this section, the factors that influence the selection of a specific aircraft airflow and air quality research approach, are discussed. Moreover, recommendations for research practices extracted from the available literature are presented.

2.4.1 Attributes and Scope of the Research

Airflow and air quality research in airliner cabin environments can range in spatial scale from a single seat, or group of seats, to a full-scale section of the cabin, or a whole cabin in some cases. The parameters that can be considered for study are numerous; such as airflow velocity, air temperature, relative humidity, buoyancy effects, air turbulence and vorticity effects, gaseous and/or particulate contaminant dispersion, particulate contaminant deposition, and more. In addition, the general theme of the study can vary significantly. For instance, thermal comfort, comparison of ventilation systems' performance, effect of moving bodies on airflow patterns, influence of ventilation on contaminant dispersion and/or deposition rates, and infection risk assessment are among many research topics found in literature.

2.4.2 Experimental Work Difficulties and Advantages

The complexity in the aircraft cabin environment makes the experimental quantification of physical phenomena, such as buoyancy effects or simultaneous cabin-wide flow behavior, a very challenging task. Additionally, using experimental measurements to validate similar numerical models or experimental prototypes is extremely demanding [111]. Table 2.2 lists some of the most commonly used experimental measurement techniques for airflow and air quality studies in aircraft cabins. The measured quantity, cost, pros, and cons are highlighted for each.

Despite the difficulties encountered with performing experimental work in aircraft cabins, the experimental approach has many advantages. Firstly, performing systematic experimental measurements inside cabins provides an assurance of certainty about the quantified parameters. Second, true technological advancement results because of the emerging and everlasting need for more accurate experimental measurement techniques. Last, numerical and computational models need validation and verification, which makes the availability of high-resolution experimental measurements of critical importance.

Table 2.2: Experimental techniques commonly used for aircraft cabin airflow and air quality measurements.

Technique	Measured quantity	Measurement method	Cost*	Pros	Cons
Particle Image Velocimetry (PIV) /Volumetric Particle Tracking Velocimetry (VPTV)	Flow velocity magnitude and direction through flow visualization (2D or 3D)	Flow seeding using tracer particles, illuminated by laser sheet(s), and flow images are recorded by video cameras	Very high	Provides real-time flow field and velocity measurements	Small measurement area, seeding particles/fluid incompatibility issues
Planar Laser-Induced Fluorescence (PLIF)	Species transport and concentration in a background medium (2D or 3D)	Specific dye substances are illuminated using laser sheets. Dye flow in the background medium is recorded by video cameras	Very high	Can work with PIV to yield velocity and concentration profiles	Requires special dyes with specific optical resonance wavelengths
Fog/Dye Flow Visualization	Flow direction and velocity (2D or 3D)	Flow visualization by injecting specific types of fogs or dyes, such as SAFEX fog, into the flow	Low	Quick and easy way to determine flow direction and pattern	Fog or dye injection method may affect the accuracy of flow velocity quantification
Hot-Sphere Anemometer (HSA) /Hot-Wire Anemometer (HWA)	Gas flow velocity (1D, 2D or 3D)	Flow velocity is inferred from the amount of cooling of the electrically-heated sphere/wire probe placed in the gas flow through Newton's law of cooling	Low	Fast response and high spatial resolution	Need frequent calibration, hot-wires break often
Ultra-sonic Anemometer (UA)	Gas flow velocity (1D, 2D or 3D)	Flow velocity is interpreted from the time the generated sonic pulses take to travel between transducer pairs	Low to moderate	Suitable for extended time measurements, infrequent maintenance	Flow distortion can be caused by the structure supporting the transducer(s)
Gas Direct Sampling	Trace gas (contaminant) concentration in a background gaseous medium	In-cabin direct gas concentration measurement using portable or fixed samplers, sensors or photometers	Low to moderate	Simple and instantaneous species concentration quantification	Limited accuracy, inefficient for unsteady measurements in large spaces
Gas Chromatography	Concentrations of trace gases, such as VOCs, in a prepared mixture specimen	Different compounds in a mixture are separated and detected after dissolving them in a mobile phase due to different travel speeds and retention times	Moderate to high	High accuracy in determining trace gas concentrations even in very small amounts	Preparing a mixture specimen from the cabin can be difficult in some flow cases

Photoacoustic Spectrometry	Concentrations of trace gases in air with very high accuracy up to part per billion or part per trillion level	Gas sample is illuminated by a high-intensity laser or infrared light which allows the gas constituents to absorb different wavelengths of the light and generate sounds (photoacoustic spectrum) proportional to the light intensity. This spectrum is used to determine the absorbing constituents of the gas sample	Moderate to high	Evaluates samples in their original, in situ form without chemical or physical treatment	Prepared gas mixture specimen is needed, gas constituents can be confused if similar light wavelengths are absorbed
Mass Spectrometry	Mass concentration of VOCs in a prepared complex mixture specimen	Different compounds in a mixture are ionized and sorted according to their mass-to-charge ratio. Separated compound is then identified by comparing the mass spectra to known masses	Moderate to high	Highly accurate, can be used for any type of trace gases	Prepared sample is required, full mass spectra analysis can be difficult if multiple mixture components have the same mass
Proton-Transfer-Reaction Mass Spectrometry (PTR-MS)	Mass concentration of VOCs in air or fluid through online (real-time) monitoring	H_3O^+ ions, produced from ionizing supplied distilled water, react with VOC trace constituents through proton transfer reactions, and their absolute concentration is calculated directly without prior calibration	Moderate to high	No prepared specimen is needed, provides real-time measurements	Not all trace gas molecules are detectable, the maximum quantifiable concentration is limited ($\approx$ 10 ppmv)
Optical Particle Counting (OPC)	Number and size of liquid or solid particles in air through standard particle size bins	Each particle is illuminated by a high intensity light (laser or halogen light), and its size is inferred using either light scattering, light obstruction, or direct imaging methods before being counted and added to its respective size bin	Low to moderate	Easy to use, provides fast and detailed particle bin size distribution	Detectable particle size range can be limited, counters can be damaged by incompatible particles

Interferometric Mie Imaging (IMI)	Size of transparent and spherical liquid droplets scattered in air (cough or sneeze droplets). Velocity of droplets can also be measured if the system is integrated with a PIV system	The width of the interference fringes, resulted from the merged scattered light from two glare points on each droplet's surface, in addition to the refractive index of the droplet material and the view angle of the receiver are analyzed together to calculate the droplet size	Very high	Handles a wide range of droplet sizes, provides accurate droplet positioning	Limited to transparent and spherical liquid aerosols only

* Costs are provided in ranges that use the following criteria: very high for techniques that cost more than U.S. $100,000, high for the cost range from $10,000 to $100,000, moderate for the range from $1,000 to $10,000, while low is for the techniques that cost less than $1,000. Those cost ranges are approximate and differ between manufacturers.

2.4.3 Numerical Modelling Characteristics and Requirements

Validation and Error Quantification

One of the main pillars of numerical simulation is the validation and verification of the calculations performed using a specific code or technique. One cannot validate a whole numerical code, but only a specific set of calculations for a case study performed using the code [78].

Error quantification between the experimentally measured and the numerically predicted quantities is performed in various ways. Most commonly, the simple or Root Mean Square Error (RMSE) or difference percentage is quantified and used to report the amount of error between the measured and predicted values. However, this method may yield some exaggerated, unrepresentative and undefined error estimates in some cases, especially for ventilation, airflow and air quality studies [3]. Alternatively, Hanna [45] proposed two performance measures to express the error between the measured (observed) and predicted concentrations in atmospheric air quality models: the Fractional Mean Bias (FB), and the Normalized Mean Square Error (NMSE). The FB and NMSE are calculated using equation 2.1 and equation 2.2, respectively.

$$FB = \frac{2\left(\overline{C_o} - \overline{C_p}\right)}{\left(\overline{C_o} + \overline{C_p}\right)}, \tag{2.1}$$

$$NMSE = \frac{\left(\overline{(C_o \ - \ C_p)^2}\right)}{\left(\overline{C_o} \ * \ \overline{C_p}\right)}, \tag{2.2}$$

where, C_o and C_p are the observed and predicted concentrations, respectively, and the overbars represent time-averaging for the concentrations.

Unlike the Root Mean Square Error, FB and NMSE define some specific attributes for the calculated error. The FB represents the shift between the observed and predicted values, while the NMSE provides the spread of one side of the values with respect to the other. For a perfect model, FB and NMSE are both equal to zero [15]. Additionally, the FB and NMSE can be used with any physical quantity in air quality studies [44].

Meshing and Grid Independence

Meshing, or discretization, of the model domain is another crucial component for numerical simulation. The number of grid elements, or nodes, which can be created in one domain may vary significantly depending on the sizes of that domain and the grid elements. As the numerical solution of the governing equations is obtained for each single element or node of the created grid, the number of elements or nodes and the way they are arranged in the grid can notably affect the accuracy of the numerical results. For this reason, an accurate procedure is necessary for quantifying the degree of independence of the numerical solution from the grid size and configuration changes, which is called Grid Independence Test (GIT). This test is usually performed for three different levels of grid fineness: coarse, medium and fine. The methodology that was used for grid independence testing in the past consisted of a comparison between the obtained solution (velocity, temperature, concentration, etc.) on a continuous spatial segment, such as line or surface, for each grid level with the other two levels. The grid level that exhibits enough grid independency of its solution (shows no significant change in the solution with the change in mesh size to a finer level) is chosen for further use.

A more representative measure for grid refinement studies was proposed by P. J. Roache, called Grid Convergence Index (GCI). The GCI uses an asymptotic approach for calculating the amount of uncertainty in grid convergence [77]. Similar to the simpler grid independence test, the GCI makes use of the solution on three different grid size levels, such grids that can be created through grid coarsening and not necessarily by grid refinement [78]. The GCI reports a numeric value that shows how much convergence is achieved in the solution

between two successive grid levels, or between the coarsest grid level, taken as a reference, and each one of the two other grids. The GCI between two consecutive grid levels m and n is provided by equation 2.3,

$$GCI_{mn} = \frac{F_s|\epsilon_{mn}|}{r^p - 1}, \tag{2.3}$$

where, F_s is a factor of safety recommended to be 3.0 for comparisons of two meshes and 1.25 for comparison of three meshes, ϵ_{mn} is relative error between the two solutions obtained on each two consecutive grid levels, and p is the order of convergence. For more information on the GCI calculation procedure followed, refer to section 4.1 of the current thesis.

The GCI has been employed in many airflow and air quality studies to quantify the grid convergence, either in aircraft cabins [91], or other closed spaces [2, 4].

Turbulence Modeling

Accurate CFD modelling of airflow and air quality cannot be performed without defining a suitable turbulence model for the simulated type of flow. This is the case since turbulence cannot be exactly simulated economically for most practical applications. Additionally, CFD models tend to solve the partial differential equations that govern the flow and dispersion (including continuity, species, energy) locally at a point in the simulated domain. On the other hand, the nature of the generated flow turbulence is nonlocal, and the smallest change occurring at one point can affect the flow far away in the domain [80]. Due to this nature, different numerical turbulence models adopt various strategies in simulating the flow turbulence with distinguished accuracies that result at proportional computational costs. Table 2.3 shows a comparison among the four main categories of turbulence models.

Table 2.3: Categories of numerical turbulence models used for airflow and air quality studies in literature.

Modeling philosophy	Computational time/-cost	Usage problems	Studied models and conclusions
DIRECT NUMERICAL SIMULATION (DNS)			
Detailed and direct simulation of all turbulent eddies and length/time scales	Years/Extreme	Very complex for ventilation simulations	DNS model is impractical for indoor flow simulation [104]
LARGE EDDY SIMULATION (LES)			
Large eddies are solved in detail, but smaller eddies are modelled	Months/High	Highly fine mesh is required for the whole domain to resolve large eddies	• LES is best suited for natural convection flow with low Rayleigh (Ra) number, and for forced convection flow with low turbulence [112] • LES-DSL is the best for forced convection or mixed convection airflow in a room [93] • LES is better than DES and RNG k-ε (RANS) models for predicting mixed convection flow in occupied aircraft cabins [62] • LES is better than RANS models for urban and atmospheric airflows with heat transfer [5, 55–57, 69]
DETACHED EDDY SIMULATION (DES)			
Hybrid modelling using LES and RANS models simultaneously	Weeks/Moderate	Hard to apply in most ventilation models	DES is good for predicting mixed convection airflow in unoccupied aircraft cabins [62]
REYNOLDS-AVERAGED NAVIER-STOKES (RANS)			
Fluctuating and time-averaged components of flow are solved in a separate manner	Days or hours/Affordable	Accuracy is less, choosing the most suitable RANS model for the simulated case is challenging	• Standard k-ε model predicts airflow well in a model for an auditorium [51, 71] • The RNG k-ε model is better than the Standard k-ε model for simulations of indoor airflow [16]

Particle Tracking Models

For air quality models that have particulate contaminant(s) dispersion, a particle tracking (transport) model is required. The numerical particle tracking models are classified into two main categories: Eulerian models and Lagrangian models. The Eulerian models consider the particles as a continuous phase, exactly like the fluid in which they disperse, and solve their governing equations using a control volume scheme. The Lagrangian models, on the other hand, treat the particles as discrete phase, and equations are solved for each particle to yield

an individual trajectory for each [110, 113]. The most common Lagrangian particle tracking model is the Discrete Random Walk (DRW) model, which considers that the fluctuating components of velocity obey a Gaussian probability distribution [113]. On the other hand, the single fluid model, the mixture model and drift flux model represent the Eulerian particle tracking approach.

In the last two decades, many studies have investigated the performance of different numerical particle tracking models in closed spaces, and compared their predictions to experimental data [72, 110, 113]. Studies agreed on promoting the use of the DRW model for the Lagrangian approach, and the drift flux model for the Eulerian approach.

Although, the Lagrangian models are currently widely adopted in the numerical particle tracking simulations and are included in most of the available commercial CFD packages [50], new mixed Eulerian-Lagrangian models are beginning to attract the attentions of many investigators. In those models, the solved equations are split into two parts: advective and diffusive. The advective component is solved using the Lagrangian step to reduce the associated numerical errors and allow large Courant number (Co) for the flow, whereas the diffusive component can be solved easily as a symmetric diagonally dominant system [20, 24].

2.5 Conclusions

In Chapter 2, ventilation and air quality in aircraft cabin environments are reviewed systematically through a critical survey of key studies performed in the last two decades.

The main gaseous contaminants considered are ozone, carbon oxides, disinsection pesticides, ethanol, and Volatile Organic Compounds (VOCs) produced in the cabin environment. The main particulate contaminants are those originating from expiratory actions, such as breathing, coughing, and sneezing, with coughing considered the most in literature. The non-expiratory particulates, on the other hand, are produced from smoking, skin shedding and dust contamination. It was noticed that the lack of adequate technologies to release and measure trace gases in the middle of the last century made the research on particulate contaminants precede that on gases by fifty years. It was also found that the number of studies that investigated the generation and dispersion of expiratory particulates in aircraft cabin environments was much less than that performed in rooms and other closed spaces in the last years.

The available aircraft ventilation systems are based on the main three categories of airflow distribution that include mixing, displacement, and personalized systems. While

the scientific community continues to debate the pros and cons of operational systems such as mixing and displacement, there is consensus that the personalized ventilation systems provide improved air quality for the occupants in comparison to the traditional ventilation systems.

The research approaches for airflow and air quality studies in aircraft cabins have varied from fully experimental to fully numerical, or combination of both. Considering the literature, it can be seen that all possible research approaches have been used to investigate airflow patterns and air quality in aircraft cabins. Many experimental measurement techniques have been used in the surveyed studies, which can be classified into two main categories: 1) flow measurement techniques, and 2) species or contaminants measurement techniques. Conversely, the numerical techniques used were limited in comparison.

Generally, there is no unique research approach, or set of research practices, that is most suitable for all aircraft airflow and air quality studies. Consequently, some of the best practices for aircraft airflow and air quality research have been proposed based on the literature, and depending on the research scope and the chosen research approach.

2.6 Investigated Research Gaps and Current Study Objectives

The main objective of the work in the current study is to conduct an evaluation for the ventilation airflow capability of controlling and/or limiting the passenger exposure to the airborne contaminant released from expiratory events such as coughs. A sub objective of the current thesis is to fill the gap in the literature that has always considered that the passenger aircraft are at rest or under cruise conditions, and that the ventilation airflow, buoyancy effects due to the occupants-generated thermal plumes, and contaminants dispersion within their cabins are only influenced by the gravitational acceleration. To fill this gap, the effect of the acceleration-induced body forces acting on a typical passenger aircraft (Boeing 767-300) on the air distribution and gaseous contaminant dispersion inside an economy cabin section is to be investigated through Computational Fluid Dynamics (CFD) simulations using the ANSYS Fluent software. This is inspired by the existence of the body force term in the Navier-Stokes conservation equations, and which in turn can affect the airflow and contaminant dispersion in the aircraft cabin. The mission legs, during which the simulations are performed are: steady level flight (cruise), climb and descent under normal aircraft

operating conditions, and climb and descent under extreme aircraft operating conditions, and more specifically, the existence of gusts during those two legs. Another sub objective of the current thesis is to study different airflow design and source control strategies as mitigation or reduction means for the increased cough-released contaminant exposure in the passenger aircraft cabin during the steady level and accelerated flights. Airflow design strategies such as changing airflow supply direction and altering airflow rate are employed. On the other hand, the source control strategies considered are changing the cough (or contaminant release) direction, varying the cough velocity/volumetric flow rate, and moving the cougher to other locations in the cabin.

The main objective of the study is achieved through addressing and fulfilling the two sub objectives highlighted.

Chapter 3

Aircraft Cabin Model and Governing Equations

3.1 Simulated Cabin Geometry

The aircraft cabin model used for the current study is adopted from the literature, and more specifically an experimental study [82], and the numerical simulation follow-up work [91].

The cabin mock-up resembles an actual size sectional economy-class cabin of a Boeing 767-300 passenger aircraft with 21 seats arranged in three rows (the seven abreast or 2-3-2 seat arrangement). The external dimensions of the cabin mock-up are 4.9 m $\times$ 3.2 m $\times$ 2.1 m (W, L, H). The cabin mock-up is located at the International Center for Indoor Environment and Energy, Technical University of Denmark, Lyngby, Denmark. The cabin mock-up appeared for the first time in the literature in [81] where more details about its configuration and control systems can be found.

The experiments conducted by Sze To et al. [82] were concerned with the dispersion and deposition of expiratory particles in the aircraft cabin mock-up after being released under different cabin airflow rates. For this sake, they positioned fifteen heated cylinders on the seats to mimic passengers, and they developed an in-house droplet generator to simulate the coughing person (droplet release point). The size distribution of released cough droplets was measured using the Interferometric Mie Imaging (IMI) technique combined with an aerosol spectrometer (GRIMM, model 1.108). Additionally, expiratory droplets' deposition in the cabin was measured by the fluorescence dye technique employing several bright dyes depositing on sheets of aluminum foil and polyethylene film. On the other hand, airflow

patterns were characterized using the Particle Image Velocimetry (PIV) technique with a double-pulsed Nd:YAG illumination laser source of 532 nm wavelength and a dual-frame CCD camera.

Figure 3.1 shows a three-dimensional view for the created cabin model in the current study to the exact dimensions using the design software DesignModeler included in the ANSYS 17.0 CFD package, and a plan view for the seats.

3.2 Model Boundary and Initial Conditions

The model's boundary and initial conditions found in the reference studies [82, 91] were closely followed and implemented in the numerical solver ANSYS Fluent 18.2 for the case of 200 L s^{-1} supply airflow rate. This corresponds to an airflow rate of 9.5 L s^{-1} per person and 22 Air Changes per Hour (ACH), which are well in the range recommended by ASHRAE standard 161-2013 [10] and similar to the airflow rates used in other studies in the literature [53, 111]. This airflow supply rate was the only one considered through the conventional mixing ventilation system used in the current study.

For more information on the conventional mixing ventilation system strategy in commercial aircraft cabins, the reader is referred to section 2.2 of Chapter 2 of the current thesis, and to more detailed studies [28, 64].

For simulation, Sulfur Hexafluoride (SF_6) gas was released in the cabin to mimic the injection and transport of the cough's smallest size droplets (typically 1.6 to 3.0 µm), and which formed the largest number concentration of the injected droplet ensemble in the experiments. This was performed for the sake of model validation and considering that the current study is a preliminary concept study and not an exact one. This is to avoid the high computational burden that results from simulating particle motion (see subsection 4.2.1). Table 3.1 shows the boundary and initial conditions for the current model.

The simulation time for the transient airflow part is 350 s at the start of which the cough (SF_6 release) was introduced for 1 s with released air volume of 0.4 L. Before this transient run, the airflow domain was completely solved in the steady mode.

Additionally, the standard wall functions were used for near-wall flow treatment with all the turbulence models employed, and the SIMPLE solution algorithm was used for the pressure-velocity coupling.

For the spatial discretization scheme, the least square cell-based method was used for gradient, the second order method was employed for solving the pressure, while the second

order upwind method was used for solving all other equations (momentum, species, turbulence, energy, etc.). On the other hand, for the temporal discretization, the first-order implicit method (implicit backward Euler method) was employed for the transient part of the simulation following a fixed time stepping procedure with a time step size of 0.1 s while allowing 10 solution iterations per time step.

Table 3.1: Boundary and initial conditions for the model.

Boundary/initial condition	Value
Supply air temperature	24 °C
Supply air flow rate	200 L s^{-1} (corresponds to a supply velocity of 2.61 m s^{-1} from each one of the two supply slots)
Air changes per hour and airflow supply rate per person	22 ACH and 9.5 L s^{-1} per person
Inlets and outlets type, and dimensions	Slot, 12 mm (width) and 0.038 m^2 (cross-sectional area)
Supply air absolute humidity	0.92 g kg^{-1} (corresponds to 5% RH at supply air temperature)
Cabin wall temperature	18 °C
Heating cylinder heat release	60 W per cylinder (occupant)
SF_6 (cough) injection location	Seat C4 (at the center of the very back row)
Air velocity at injection location	10.6 m s^{-1}
SF_6 density and molecular weight	6.14 kg m^{-3} and 146.06 grams mol^{-1}

To accurately simulate cough particle deposition on walls and surfaces, the SF_6 gas was not allowed to bounce-off the walls and surfaces in the cabin model. This was accomplished by setting a surface reaction boundary condition at every wall and surface to dissociate SF_6 upon contact to Sulfide (S_2) and Fluorine (F_2) gases according to the following reaction,

$$2\,SF_6 \xrightarrow{\text{at wall}} S_2 + 6\,F_2. \tag{3.1}$$

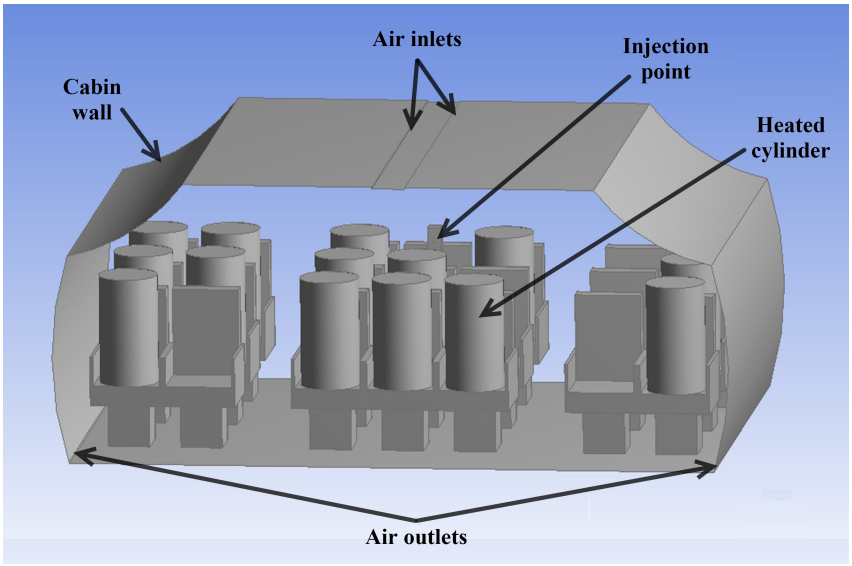

(a)

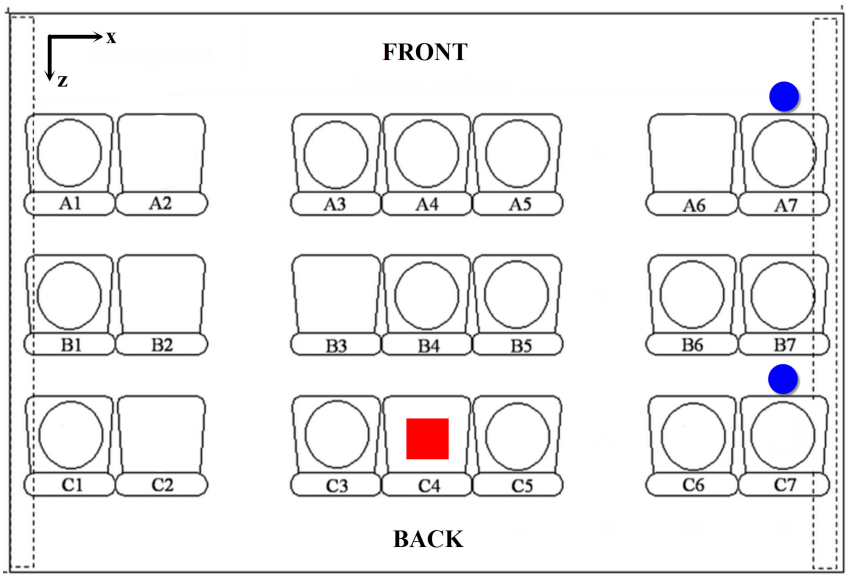

(b)

Figure 3.1: The computational cabin model used in the current study; (a) three-dimensional view of the geometry built in ANSYS, and (b) plan view for the cabin with the cougher/injector position (red square), and the SF_6 concentration monitoring points (blue circles).

As the released SF_6 in the cabin is already at very low concentrations, the concentrations of the Sulfide and Fluorine gases produced from its dissociation are extremely low and do not affect the air composition, fluid properties, or the monitored SF_6 concentration in the cabin.

This method allows a surrogate simulation of small particles that behave like gases very computationally economically. The assessment of this method versus experimental data is carried out later in Chapter 4 of this thesis.

3.3 Governing Equations

The equations governing airflow and contaminant dispersion in the current cabin model solved by the ANSYS Fluent 18.2 software are as follows,

The Mass Conservation (Continuity) Equation

$$\frac{\partial \rho}{\partial t} \; + \; \nabla . \left(\rho \vec{V} \right) = 0, \tag{3.2}$$

where ρ is the in-cabin air density, t is the time , and $\vec{V}$ is the flow velocity vector. As the density ρ in the model is constant (independent of space and time), except where buoyancy effects are accounted for, the continuity equation simplifies to the kinematic condition that the velocity field should be solenoidal or divergence-free [3],

$$\nabla . \left(\vec{V} \right) = 0. \tag{3.3}$$

This is because the airflow in the cabin can be safely considered incompressible as verified by considering the dimensionless Mach number. Even with the highest velocity in the domain equal to the cough velocity of $10.6\,\mathrm{m\,s^{-1}}$, the highest Mach number (Ma) in the cabin is $10.6/343 = 0.03$, which is much less than the incompressibility assumption limit ($Ma = 0.3$).

The Momentum Conservation Equation

$$\frac{\partial}{\partial t} \left(\rho \vec{V} \right) \; + \; \nabla . \left(\rho \vec{V} \vec{V} \right) = -\nabla p \; + \nabla . \left(\overline{\overline{\tau}} \right) \; + \; \rho \vec{g} \; + \; \rho \vec{a}, \tag{3.4}$$

where p is the static pressure, $\overline{\overline{\tau}}$ is the stress tensor, and $\vec{g}$ and $\vec{a}$ are the gravitational and external body accelerations, respectively [9].

The Energy Equation

$$\frac{\partial}{\partial t}(\rho E) + \nabla.\left(\vec{V}(\rho E + p)\right) = \nabla.\left(k_{eff}\nabla T - \sum_j h_j \vec{J}_j + \left(\overline{\overline{\tau}}_{eff}.\vec{V}\right)\right) + S_h, \quad (3.5)$$

where k_{eff} is the effective conductivity $= k + k_t$ (k_t is the turbulent thermal conductivity), T is the temperature, $\vec{J}_j$ is the diffusion flux of species j, and S_h is an additional volumetric heat source (e.g. passenger bodies). E is defined as,

$$E = h - \frac{p}{\rho} + \frac{V^2}{2}, \quad (3.6)$$

where h is the sensible enthalpy of the fluid flow, which is defined for ideal gases (i.e. air) as, $h = \sum_j Y_j h_j$, where Y_j is the mass fraction of species j and,

$$h_j = \int_{T_{ref}}^{T} c_{p,j}\, dT. \quad (3.7)$$

For the pressure-solver used, T_{ref} is taken as 298.15 K [9].

Species Transport Equation

$$\frac{\partial}{\partial t}(\rho Y_i) + \nabla.\left(\rho\vec{V}Y_i\right) = -\nabla.\vec{J}_i + S_i, \quad (3.8)$$

where Y_i is the local mass fraction of each species i in the domain, and S_i is the rate of creation (or consumption) of species by addition (or removal) from the dispersed phase plus any user-defined sources. $\vec{J}_i$ is the diffusion flux of species i, which for mass diffusion in turbulent flows is defined as,

$$\vec{J}_i = -\left(\rho D_{i,m} + \frac{\mu_t}{Sc_t}\right)\nabla Y_i - D_{T,i}\frac{\nabla T}{T}, \quad (3.9)$$

where $D_{i,m}$ is the mass diffusion coefficient for species i in the mixture, $D_{T,i}$ is the thermal (Soret) diffusion coefficient, μ_t is the turbulent viscosity, and Sc_t is the turbulent Schmidt number.

Turbulence Kinetic Energy (k) and Turbulence Kinetic Energy Dissipation Rate (ε) Equations (for the RNG $k-\varepsilon$ Model)

$$\frac{\partial}{\partial t}(\rho k) + \frac{\partial}{\partial x_i}(\rho k u_i) = \frac{\partial}{\partial x_i}\left(\alpha_k \mu_{eff} \frac{\partial k}{\partial x_i}\right) + G_k + G_b - \rho\varepsilon + S_k, \tag{3.10}$$

$$\frac{\partial}{\partial t}(\rho \varepsilon) + \frac{\partial}{\partial x_i}(\rho \varepsilon u_i) = \frac{\partial}{\partial x_j}\left(\alpha_\varepsilon \mu_{eff} \frac{\partial \varepsilon}{\partial x_j}\right) + C_{1\varepsilon}\frac{\varepsilon}{k}(G_k + C_{3\varepsilon}G_b) - C_{2\varepsilon}\rho\frac{\varepsilon^2}{k} - R_\varepsilon + S_\varepsilon, \tag{3.11}$$

where α_k and α_ε are the inverse effective Prandtl numbers for k and ε, respectively, S_k and S_ε are user-defined source (or sink) terms, and $C_{1\varepsilon}$, $C_{2\varepsilon}$ and $C_{3\varepsilon}$ are constants defined by the RNG k-ε model theory. Also, G_k represents the generation (or consumption) of turbulence kinetic energy due to the mean velocity gradients, and G_b is the generation (or consumption) of turbulence kinetic energy due to buoyancy, which is formulated using the Standard Gradient Diffusion Hypothesis (SGDH) as,

$$G_b = -g_i \frac{\mu_t}{\rho Pr_t}\frac{\partial \rho}{\partial x_i}, \tag{3.12}$$

where g_i is the component of the gravitational vector in the i^{th} direction, μ_t is the turbulent viscosity, and Pr_t is the turbulent Prandtl number.

3.4 Conclusions

In Chapter 3, the simulated aircraft cabin model built using ANSYS DesignModeler according to actual dimensions for a similar mockup in literature is presented. Also, the experiments performed by Sze To et al. [82] in the cabin mockup were introduced to be used for model validation (as illustrated later in Chapter 4).

The model was initially run in the steady state mode to completely solve the airflow domain, then it was switched to the transient mode once the contaminant (SF_6) was introduced into the cabin space in the form of a cough puff from the mouth of one occupant.

The SF_6 contaminant was utilized to mimic the injection and transport of the smallest cough droplets size in the range from 1.6 µm to 3.0 µm, for which a heavy gas such as SF_6 can be a suitable surrogate. The concentration of SF_6 was monitored with time at two locations in the cabin; namely seat A7 and seat C7. Additionally, and to simulate the condition of

cough particle deposition on walls and surfaces, the SF_6 gas was not allowed to bounce-off the walls and surfaces in the model. This was achieved by embedding a wall reaction at every wall and surface that dissociates SF_6 to Sulfide (S_2) and Fluorine (F_2) gases on contact.

Chapter 4

Grid Creation and Model Validation

4.1 Grid Properties and Independence Test

The unstructured grid (mesh) created for the cabin model consists mainly of tetrahedron, wedge, and hexahedron elements. The tetrahedron elements were used to fill the majority of the cabin interior volume, while the wedge and hexahedron-shaped elements were mainly used for creating seven layers of inflation mesh adjacent to the cabin walls, and around the seats and cylinders to capture the flow boundary layer more efficiently at these positions. The y^+ value was kept between 300 and 400 at the walls by forcing an average thickness for the first inflation mesh layer of 0.1 m. This is backed by several studies in the literature [7, 13].

For defining the degree of independence of the obtained solution (airflow velocity and time-averaged SF_6 concentration) from the grid size changes, a grid independence test was conducted. In the present work, four levels of grid fineness (sizes) were created, namely: coarse grid (4,704,751 elements), medium grid (5,522,517 elements), fine grid (7,375,800 elements), and very fine grid (9,761,227 elements) in the order of grid element size decrease or fineness increase. The grid refinement ratio (r) between each two consecutive grid levels was kept constant at 1.1, which was the maximum ratio possible due to the complex cabin geometry adopted.

Transient simulation runs were performed for airflow and SF_6 dispersion in the cabin on each grid level with the identical boundary conditions mentioned previously in section 3.2. Figure 4.1 presents the normalized SF_6 concentration time series (real-time concentration divided by time-averaged concentration) as they change with the simulation time for the four grid levels with respect to the experimental data (see section 4.2). The real-time SF_6

concentration was monitored at the breathing level of the occupants (1.17 m from the floor) at seats A7 and C7 (blue circles in Figure 3.1).

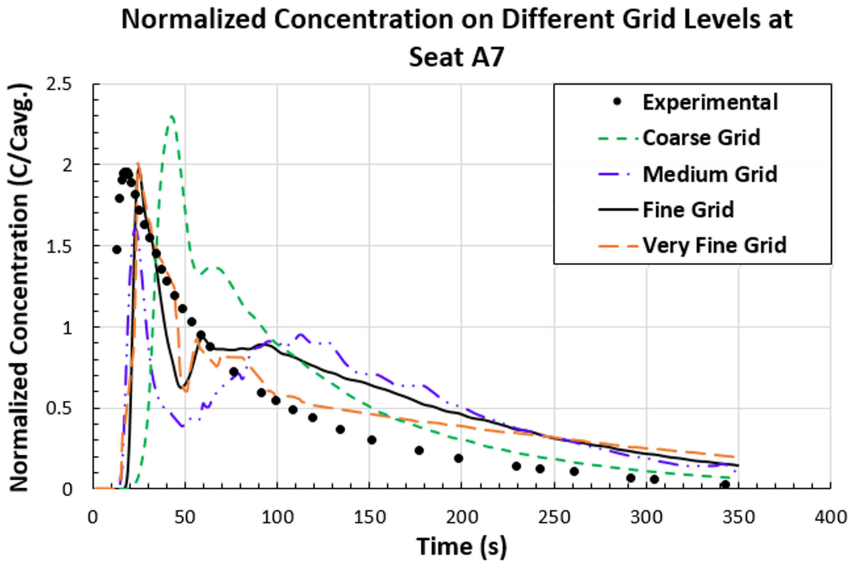

(a)

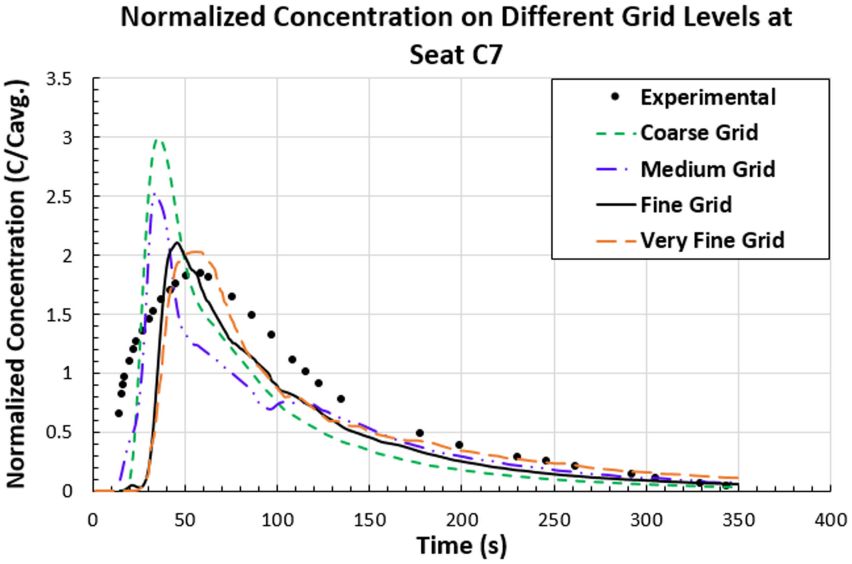

(b)

Figure 4.1: Normalized SF_6 concentration change with the simulation time on the four grid levels used; (a) at seat A7, and (b) at seat C7.

In addition to the graphical comparison of solution on the four grid levels, the Grid Convergence Index (GCI) is calculated to indicate the amount of asymptotic convergence

that the solution achieves through determining the uncertainty in solution between two consecutive grid levels [3, 77].

In the current study, the GCI is calculated between two consecutive grid levels m and n using equation 2.3 previously shown. The GCI calculation procedure followed is presented in detail in [2, 3]. The steps of this procedure are as follows,

First, a representative cell mesh size, or mesh spacing, h is calculated for each mesh level using the following formula,

$$h = \left(\frac{1}{N} \sum_{i=1}^{N} \Delta V_i \right)^{\frac{1}{3}}, \tag{4.1}$$

where ΔV_i is the volume of cell i, and N is the total number of cells.

Second, the mesh refinement ratio r_{mn} from one mesh level m to the next n is quantified as $r_{mn} = \frac{h_m}{h_n}$. This refinement ratio is kept constant $r = r_{32} = r_{21}$ assuming that $h_1 < h_2 < h_3$. Next, the change in the solution (velocity, temperature, concentration, etc.) between each two consecutive mesh levels is calculated as $\Phi_{mn} = \Phi_m - \Phi_n$.

Then, the order of convergence p is determined as follows,

$$p = \frac{\ln\left(\frac{\Phi_{32}}{\Phi_{21}}\right)}{\ln(r)}. \tag{4.2}$$

The relative error ϵ_{mn} is then calculated using the formula,

$$\epsilon_{mn} = \frac{\Phi_m - \Phi_n}{\Phi_n}. \tag{4.3}$$

Finally, the GCI is quantified between each two consecutive grid levels from the following equation,

$$\mathrm{GCI}_{mn} = \frac{F_s |\epsilon_{mn}|}{r^p - 1}. \tag{4.4}$$

The GCI calculated for the SF_6 concentration from coarse to medium grid was 3.13%, from medium to fine grid was 1.26%, and from fine to very fine grid was 0.34% at seat A7. On the other hand, at seat C7, the GCI was 3.55% from coarse to medium grid, 1.41% between medium and fine grids, while it was equal to 0.29% between fine and very fine grids. Based on these results, and as the change in the solution between the fine and very fine grid levels is minimal, the fine grid level was found to exhibit enough grid independency of the

solution while preserving the computational economy. Therefore, the fine grid level was used further.

4.2 Model Validation and Error Estimation

The data used for the aircraft cabin model validation are divided into two categories. The first category is mainly extracted from the original study of Sze To et al. [82] considering the smallest particle size range (1.6-3.0 µm) to be compared with the SF_6 gas (passive tracer) concentration time series monitored at the two seats A7 and C7 over the simulation time.

The second category validates the model by comparing the ventilation airflow velocities at multiple locations in the cabin between the experiments and simulations. The airflow velocity predictions of the current model are compared to PIV measurements from the experimental study by Sze To et al. [82], and numerical predictions of the follow-up CFD model by Wan et al. [91].

4.2.1 Validation using Contaminant Concentration Time Series

The SF_6 gas was chosen as a surrogate to the smallest size cough particles because of its high density and molecular weight (about 6.14 kg m^{-3} and 146.06 grams mol^{-1}, respectively), which make it capable of mimicking the movements of those particles in the cabin. Additionally, this choice is based on the findings of multiple studies in literature that indicate that the smallest size droplets (3 µm in diameter and less) behave like the heavy gaseous substances (especially SF_6) when dispersing in the cabin space [53, 111]. To mimic particle deposition at the walls, it was necessary to have an SF_6 sink at the walls by implementing a dissociation mechanism at the wall boundary. Such need was confirmed by comparing the results without a dissociation mechanism, in which case the SF_6 concentrations in the domain were too high.

Figure 4.2 depicts the comparison of normalized SF_6 concentration time series at seats A7 and C7 using the numerical solution obtained on the fine grid only and employing different turbulence models from the Reynolds-averaged Navier-Stokes (RANS) group that can simulate buoyancy effects on the production and dissipation of turbulence kinetic energy (k and ε, respectively).

The error estimation in the current CFD model predictions for concentration time series are calculated using the FB and NMSE measures previously presented in equations 2.1 and 2.2, respectively. Those measures were first proposed by Steven Hanna [45], and used by him

and others later in multiple studies to express the error between the observed and predicted concentrations in atmospheric air quality models [5, 15, 44].

Table 4.1 provides the FB and NMSE values calculated for the normalized SF_6 concentration time series between the experimental measurements and the numerical predictions of the same turbulence models as in Figure 4.2.

Table 4.1: FB and NMSE values for the numerical predictions of the turbulence models used.

Turbulence model	Seat A7		Seat C7	
	FB	NMSE	FB	NMSE
Standard k-ε	0.67455	1.25019	0.55768	0.58504
RNG k-ε	**0.31867**	**0.71138**	**0.39909**	**0.37711**
Realizable k-ε	0.69038	1.53628	0.50152	0.58732
SST k-ω	0.60606	1.19904	0.31138	0.25556
Standard k-ω	0.49237	0.97809	0.51303	0.55494

From Table 4.1, it can be concluded that the ReNormalization Group (RNG) k-ε turbulence model exhibits the overall lowest values for FB and NMSE at both seats (shown in bold text) among all other models. Consequently, the RNG k-ε model provides the most accurate SF_6 concentration predictions at both seats, A7 and C7, and therefore will be used further. This result also agrees with the recommendations for similar airflow simulation cases in closed spaces found in the literature [16, 62, 93, 104, 112]. On the other hand, the NMSE values for normalized concentration at seat C7 are about 50% less than at seat A7, while FB values are almost the same at both seats. This shows that the shift between the observed and predicted concentration values is similar, but the spread of the predicted data with respect to the observed ones is two times higher at seat A7, which indicates less accurate predictions.

For all turbulence models used, the decrease in prediction accuracy from seat C7 to seat A7 can very well be attributed to the condition of airflow, and therefore that of the surrogate SF_6 gas, from the emission source (at seat C4) to each seat. From C4 to C7 the flow direction is mainly lateral (latitudinal) which is less susceptible to the airflow turbulence and circulation (see subsection 6.2.2) than the primarily longitudinal flow experienced from C4 to A7 (see Figure 3.1).

Such decrease in the accuracy of predictions inside aircraft cabins are common because

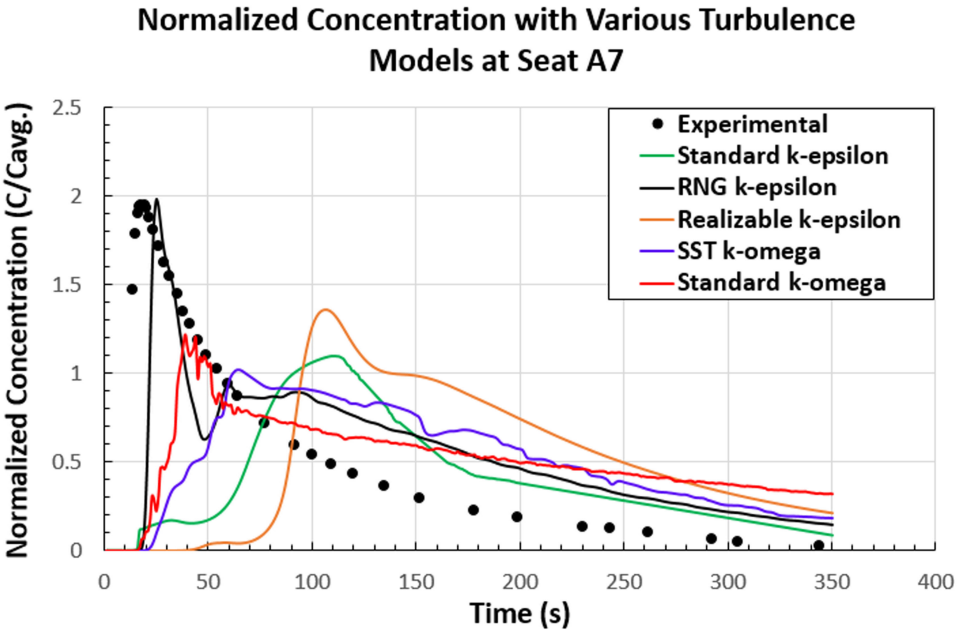

(a)

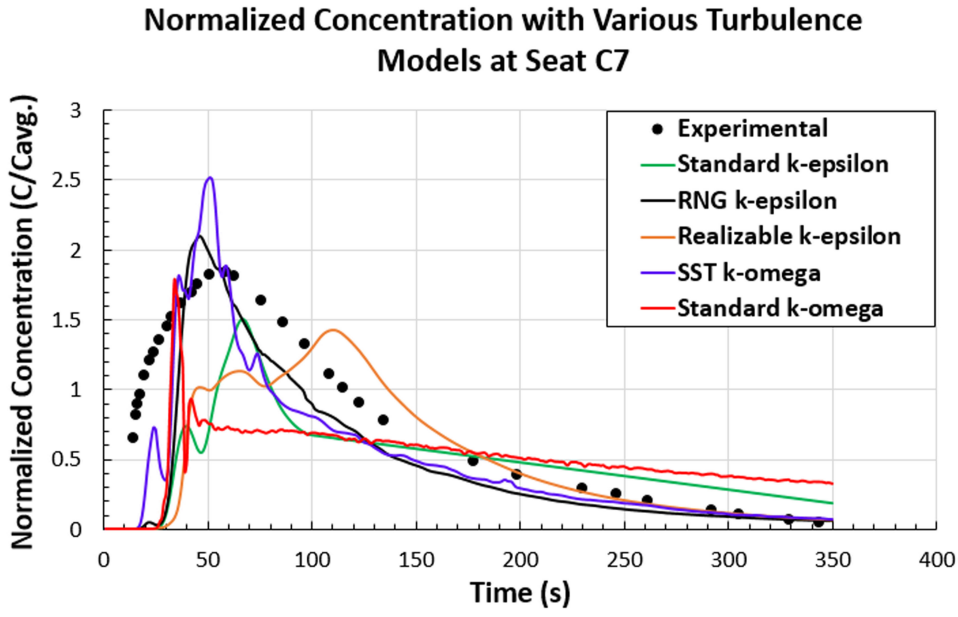

(b)

Figure 4.2: Comparison of the normalized SF_6 concentration time series between the experiment and numerical simulations on the fine grid level using different turbulence models; (a) at seat A7, and (b) at seat C7.

of the very complex and highly turbulent airflow field and contaminant dispersion behavior in the cabin. This is evidenced by the majority of the numerical simulation studies in the field allowing a large margin of error (50% RMSE or more) for the validation of contaminant concentration, airflow velocity field and temperature variations with experimental data in aircraft cabin environments [37, 48, 54, 111].

Generally, the calculated FB and NMSE figures agree well with the graphical presentation for the measured and calculated concentration time series (see Figure 4.2).

The experimental measurements of droplet concentration, and the resulting exposure of passengers, were not free from error and uncertainty. This uncertainty was mainly caused by the limited resolution of the aerosol spectrometer used and that of the liquid flow meter in the droplet generator. The uncertainty in exposure was estimated to be $\pm 9.63 \times 10^{-6}$ mL for droplets $\leq$ 15 µm in diameter, which formed the majority of droplets captured in the experiments [82]. In spite of those estimations, no error bars were provided for the experimental droplet concentration time series (shown as black dots in Figures 4.1 and 4.2) by the authors of the original study.

4.2.2 Validation using Ventilation Airflow Velocities

Airflow velocities predicted in the current cabin model are compared to experimental measurements using PIV in the cabin mockup performed by Sze To et al. [82] and to the calculations of the CFD model by Wan et al. [91] to validate the current CFD model. The three locations in the cabin at which the airflow velocities are compared, namely: A, B, and C are on a lateral plane set at the center of the cabin. Location A is at the left-side supply air slot (looking to the front), location B is above the head of the passenger on the left side close to the wall, and location C is above the head of the passenger at the center of the cabin.

Table 4.3 lists the airflow velocity values at locations A, B, and C for the experimental PIV measurements and the numerical predictions of both the CFD model by Wan et al. and the CFD model in the current study.

Table 4.3: Airflow velocities at locations A, B, and C in the cabin between experiment and numerical predictions.

Locations	Airflow Velocity (m s^{-1})		
	Experimental (PIV) [82]	Numerical Prediction [91]	Numerical Prediction (Current Study)
A	2.9	2.6	2.61
B	0.2 - 0.5	0.2 - 0.6	0.13 - 0.6
C	0.1 - 0.3	0.2 - 0.3	0.13 - 0.3

Looking at Table 4.3, it can be noticed that the airflow velocity predictions of the current model at the three locations are slightly closer to the predictions of the CFD model by Wan et al. than to the experimental PIV measurements. However, the airflow velocity predictions of both CFD models are well within the range of the measured values.

The most accurate predictions for both CFD models are at location C at the center of the cabin with 0.2 to 0.3 m s^{-1} and 0.13 to 0.3 m s^{-1} for the models compared to 0.1 to 0.3 m s^{-1} for the PIV measurements. This resemblance in airflow velocities at this location can be attributed to the ability of the CFD models to capture the larger airflow eddies and circulation at the center of the cabin than the smaller airflow eddies near the wall at location B, or the airflow stream from the left-side supply slot close to the cabin ceiling at location A. Those small airflow eddies near the walls are mainly influenced by the viscous shear forces in the viscous sublayer making them more challenging to be predicted using the RANS RNG k-ε model with standard wall function employed in both CFD models. This invites the need for more detailed and optimized wall functions and near-wall treatments, such as the integrated Werner-Wengle wall function and the van Driest near-wall treatment [3].

To complete the validation of the current model using ventilation airflow velocities, the FB and NMSE indices are calculated using equations 2.1 and 2.2 between the current model's airflow velocity predictions and the experimental PIV measurements.

On average among the three locations, the FB and NMSE were found equal to 0.0797 and 0.0274, respectively. As these FB and NMSE values are very close to zero, this indicates that the shift and spread between the experimental and numerical values are very small and, therefore, airflow velocity predictions are valid.

4.3 Conclusions

In Chapter 4, the properties of the unstructured grid created for the simulated cabin model were presented. The grid is comprised of tetrahedron elements for the majority of the cabin volume, and wedge and hexahedron elements for the grid inflation layers set at the walls and around the cabin seats and cylinders mimicking the passengers. The y^+ was kept around 300 to 400 at the walls.

The grid convergence testing was performed using two methods. First, graphical comparison of normalized SF_6 concentration time series on four grid levels was performed, and then, the Grid Convergence Index (GCI) between each two successive grid levels was calculated to indicate the amount of asymptotic convergence that the solution achieves between two consecutive grid levels. The two methods agreed on that the fine grid level (third grid level in the order of grid fineness) exhibits enough grid independency of the solution while preserving the computation economy, and consequently, is used for further simulations.

The validation of the model's numerical SF_6 concentration predictions was performed against two categories of data in the literature. First, the experimental data for the concentration time series of the smallest cough particles in the size range from 1.6 µm to 3.0 µm after being normalized. Different Reynolds-Averaged Navier-Stokes (RANS) turbulence models that can simulate buoyancy effects on the production and dissipation of turbulence kinetic energy (k) were employed for simulations, such as the Standard k-ε, RNG k-ε, Realizable k-ε, SST k-ω, and Standard k-ω. The error between the experimental measurements and the numerical predictions was shown graphically using the normalized concentration time series, and estimated using two common measures in the atmospheric air quality models, namely: the Fractional Mean Bias (FB) and the Normalized Mean Square Error (NMSE). Both methods indicated that the RNG k-ε model is the most accurate turbulence model for the simulated case, and therefore, is used for further simulations.

Second validation of the model was performed using ventilation airflow velocities at three locations in the cabin. The predictions of the current study model were compared to PIV measurements from the experimental study by Sze To et al., and numerical predictions of the follow-up CFD model by Wan et al. Generally, the numerical predictions of the current model were found to lie well in the measured airflow velocity ranges with FB and NMSE equal to 0.0797 and 0.0274, respectively, between the two sides.

Chapter 5

Airflow Design and Source Control Strategies for Reducing Airborne Contaminant Exposure in the Aircraft Cabin During the Steady Level Flight Leg

In the current chapter, different airflow design and source control strategies are investigated as mitigation or reduction means for the cough-released contaminant exposure in passenger aircraft cabin during the steady level flight leg using numerical simulations. Airflow design strategies such as changing airflow supply direction and altering airflow rate are employed. On the other hand, the source control strategies considered are changing the cough (or contaminant release) direction, varying the cough velocity/volumetric flow rate, and moving the cougher to other locations in the cabin.

5.1 Airflow Design Strategies

5.1.1 Airflow Direction

In the current investigation, the direction of the supply airflow was changed using two-dimensional and three-dimensional approaches. In 2-D, the airflow direction was tilted downwards from the cabin ceiling by an angle α. However, in 3-D, an angle β was added

to direct the airflow either to the front or to the back of the cabin while still being tilted downwards with the angle α. Figure 5.1 shows examples of using those angles in 2-D and 3-D views for the cabin model.

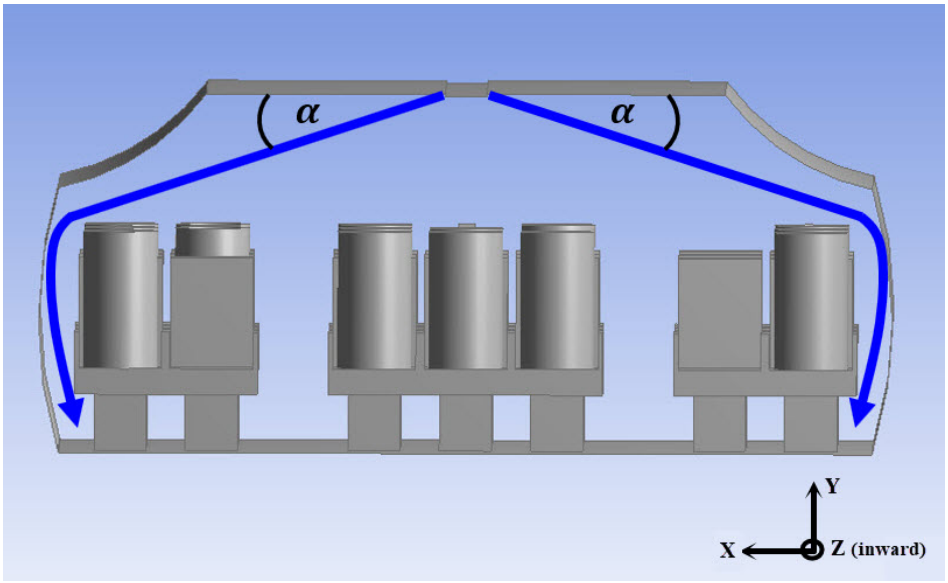

(a)

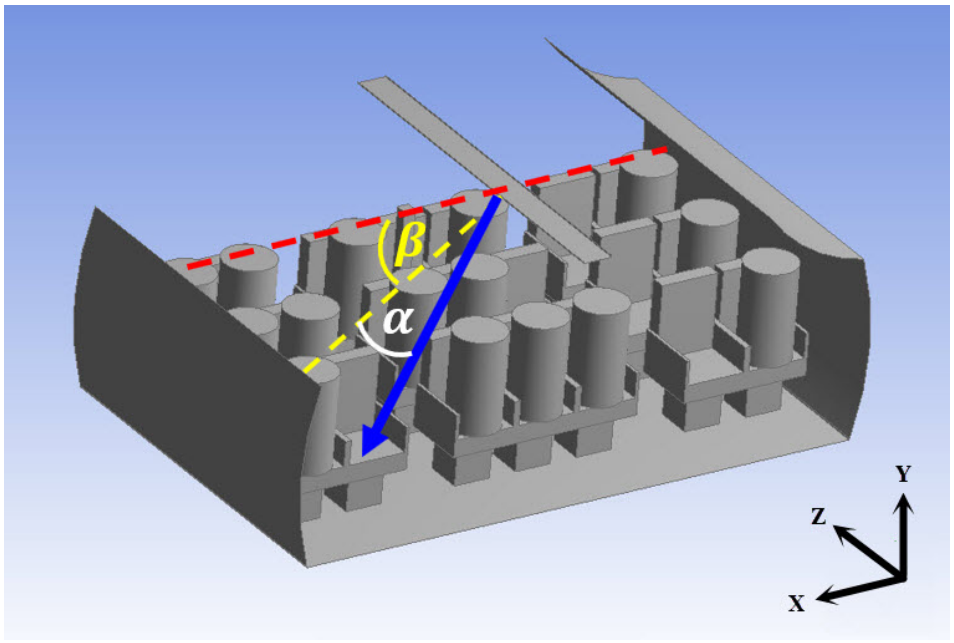

(b)

Figure 5.1: Redirecting the supplied airflow to the aircraft cabin; (a) in 2-D using angle α only, and (b) in 3-D using angles α (downwards) and β (front or back) together.

Changing Angle α Only

First, only the change of the supply airflow direction angle α in 2-D is considered. Three airflow supply angles were investigated for their ability to reduce the SF_6 concentration exposure in the cabin during the steady level flight leg: 20°, 30°, and 60°. The SF_6 concentration time series for the 20° and 30° airflow supply scenarios during steady level flight leg versus that for the standard steady level flight at seats A7 and C7 are shown in Figure 5.2. However, for the readability of the figures, the same comparison for the 60° supply case is shown separately in Figure 5.3.

From Figures 5.2 and 5.3 it can be noticed that there is a considerable difference in the calculated SF_6 concentration time series using each of the three airflow supply angles. The airflow supplied at 20° had the peak SF_6 concentration, and consequently the exposure of occupants, reduced to almost 50% of the original concentration during steady flight at seat A7. However, at seat C7, the 20° air supply yielded a SF_6 concentration time series which is nearly coincident to that for the baseline steady flight air supply case. On the other hand, the airflow supplied at 30° was not able to provide better air quality conditions at the two monitoring locations, and the exposure of passengers to the contaminant was almost the same as, or higher than, that for the original steady flight air supply scenario.

Nevertheless, from Figure 5.3, it can be seen that supplying air at 60° to the cabin produced the worst air quality conditions at the two locations. This is backed by the very high passenger exposure to SF_6 under this air supply condition, especially at seat C7, where the exposure was around 2000% of the original case.

To put this comparison in a more graphical way, SF_6 concentration contours are shown at the breathing level of the occupants for the 20° (the best case) and 60° (the worst case) airflow supply in Figure 5.4. Due to the transient nature of the simulations, the best representative time window was chosen to show the contours, which is at 350 s in this case. As can be seen in the two contour plots, with $\alpha = 60°$, the area covered by the supplied air is very limited at the cabin central area around the two rear seat rows. This leaves most of the seats on the two cabin sides exposed to the contaminant. Conversely, the airflow supplied at 20° efficiently reached the cabin sides and lead to reduced passenger exposure at most cabin seats. However, with $\alpha = 20°$, a very minor increase in the SF_6 concentration is seen at the back of the cabin to which the contaminant is gradually pushed back by fresh air as time passes during the steady flight leg.

As the supply airflow direction angle α solely changes, it can be noticed that when the angle α increases from 20° to 60°, the average SF_6 concentration in the cabin, the

concentration at seat A7, and at seat C7 all increase. However, the increase in the SF_6 concentration at seat C7 is more evident. This increase in contaminant concentration at the back of the cabin can be attributed to the lateral mode of contaminant dispersion from seat C4 (location of the cougher) to seat C7. This makes the turbulent airflow circulation (eddies) enhanced by the thermal plumes from the bodies of the occupants carry the majority of the contaminant to seat C7 shortly after release before it can be directed to the front rows after being diluted in the cabin air by the longitudinal airflow eddies. Such a contaminant transport trend is intensified under the steady level flight condition when the airflow angle α increases leaving the cabin sides less protected by the fresh ventilation airflow currents, which enhances the contaminant spread on each of those sides especially at the back rows as can be noticed in Figure 5.4 (b).

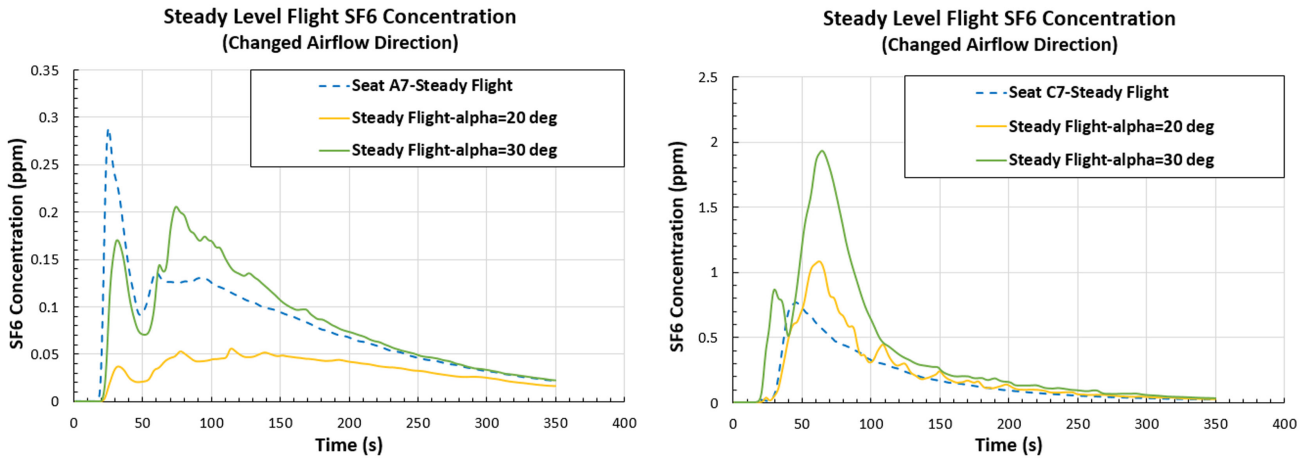

(a) (b)

Figure 5.2: Comparison of the predicted SF_6 concentration time series during the steady level flight leg using the default, 20°, and 30° airflow supply angles; (a) at seat A7, and (b) at seat C7.

Changing Angles α and β Simultaneously

In this alternative airflow redirection approach, angle β is simultaneously changed with angle α to add a three-dimensional approach to this investigation. As $\alpha = 20°$ provided a better cabin air quality condition relative to the other two airflow supply angles in 2-D, $\alpha = 20°$ will be used again here with β also chosen to be equal to 20° with supply airflow either directed to the front or to the back of the cabin. This was performed to provide a clear comparison

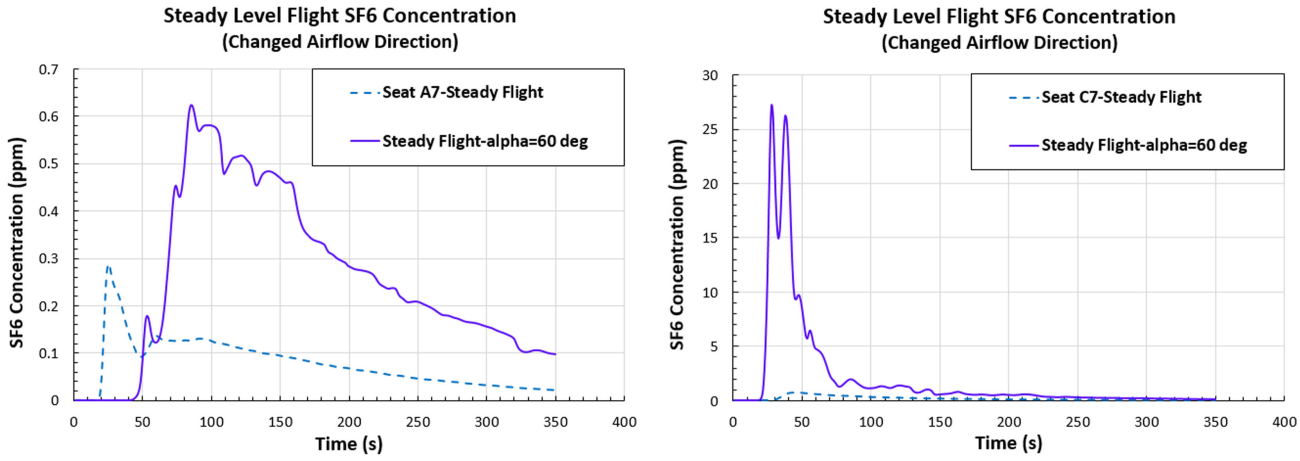

(a) (b)

Figure 5.3: Comparison of the predicted SF_6 concentration time series during the steady level flight leg using the default and 60° airflow supply angles; (a) at seat A7, and (b) at seat C7.

between those two scenarios while limiting the number of simulations required. Figure 5.5 depicts the SF_6 concentration time series at the two monitoring locations using $\beta = 20°$ to the front and to the back.

Comparing the SF_6 concentration time series at the two locations from Figure 5.5, it can be seen that the $\beta = 20°$ airflow supply to the back of the cabin was able to consistently reduce the time-integrated passenger exposure from the original steady flight case either at seat A7 or seat C7. More specifically, at seat C7, the peak exposure was reduced to about 25% of that for the steady flight condition. Conversely, in case of the $\beta = 20°$ airflow supply to the front, the passenger exposure was approximately 400% higher at seat A7 than the original steady flight case, but, at seat C7, the exposure was almost the same as that for the steady flight case. Such complex response in concentration time series can be understood when the SF_6 contour plots for the mentioned two airflow supply cases at 350 s are compared as shown in Figure 5.6.

As noticed from the figure, directing airflow to the front of the cabin leads to an opposite response by the SF_6 contaminant surrogate, which disperses primarily in a longitudinal manner under the effect of the turbulent airflow eddies to the back of the cabin and eventually settle there at the end of simulation time (350 s). Before this happens, however, and for a brief period of time (first 100 s after contaminant release in the cabin), the airflow moves the majority of the contaminant to the frontal rows. This explains the very high contaminant

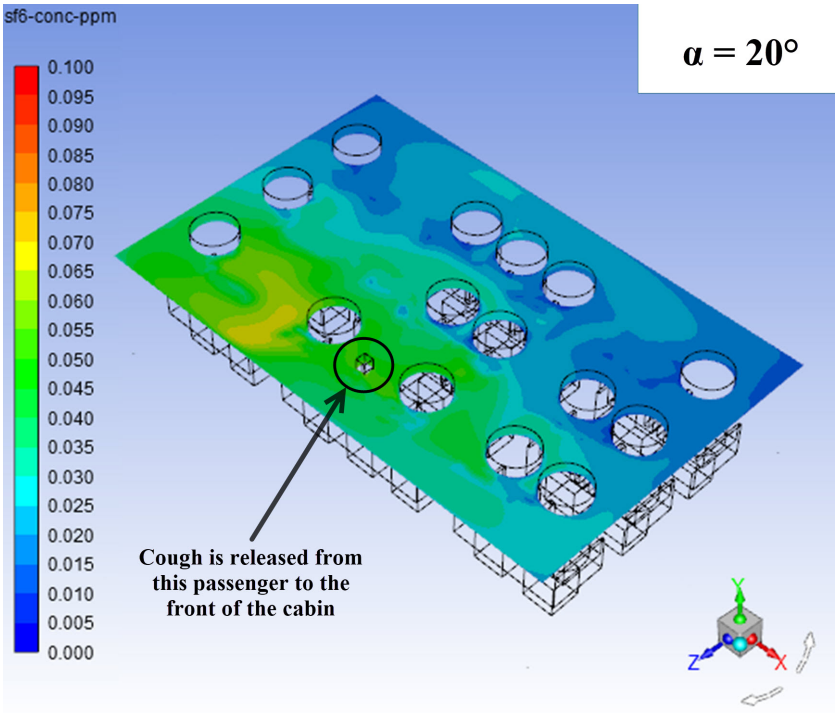

(a)

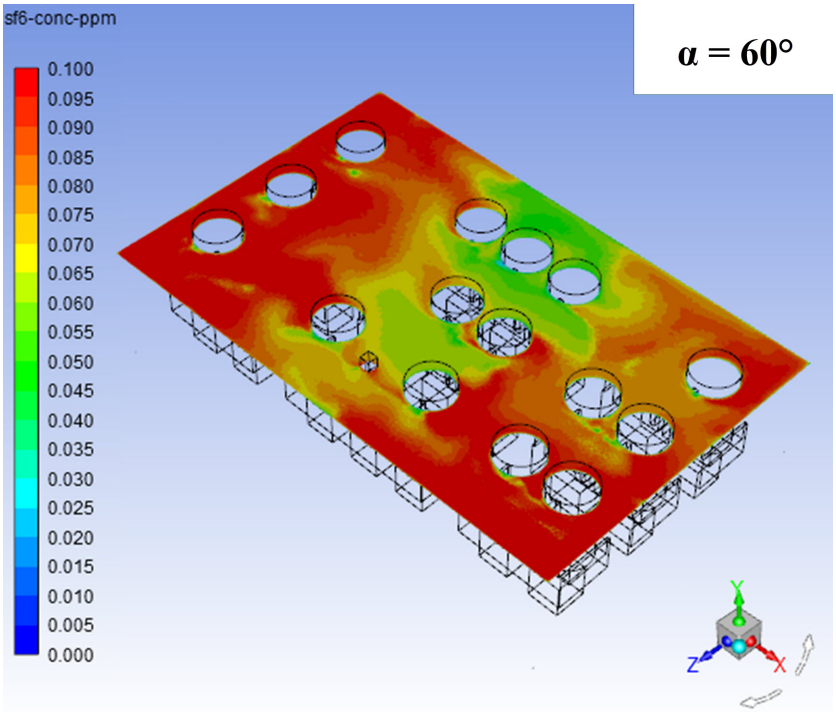

(b)

Figure 5.4: SF_6 concentration contour plots at passenger breathing level during steady level flight at 350 s; (a) using airflow supply angle $\alpha = 20°$, and (b) using airflow supply angle $\alpha = 60°$.

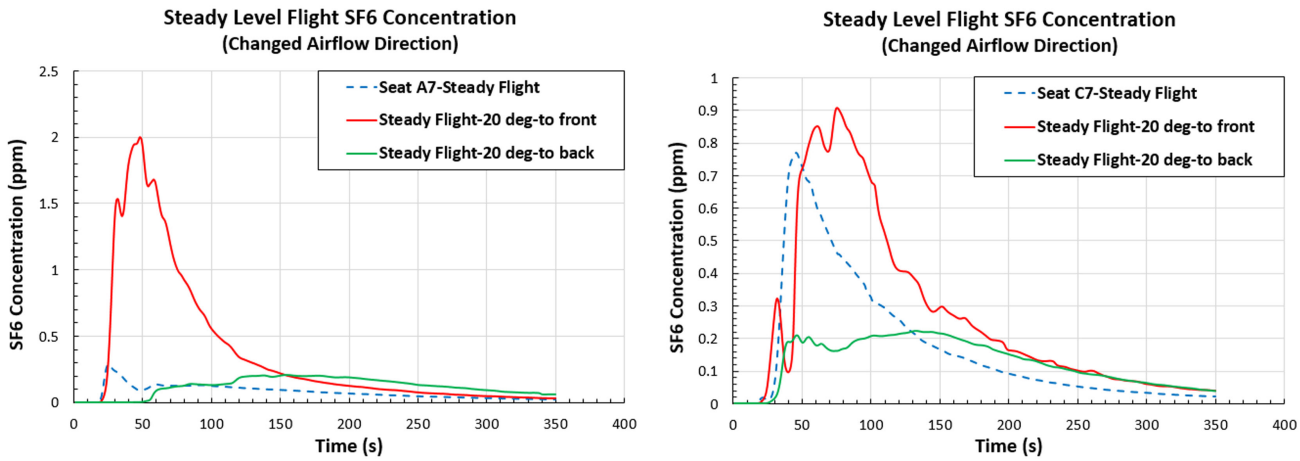

(a) (b)

Figure 5.5: Comparison of the predicted SF_6 concentration time series during the steady level flight leg using supply angles $\alpha = 20°$ and $\beta = 20°$ (to front and back); (a) at seat A7, and (b) at seat C7.

concentration at seat A7 at the front of the cabin around this time.

On the other hand, supplying airflow to the back of the cabin leads to a steady push of the contaminant to the front of the cabin by the airflow currents, which provide appropriate dilution of the contaminant in the cabin air with no major dispersion patterns in the back rows. This can be attributed to the overall ventilation airflow direction in this case being in the same direction of the cough flow. The contaminant dilution provided by the back-directed airflow makes the overall passenger exposure to the contaminant consistently low at most cabin seats as seen in Figure 5.5.

5.1.2 Airflow Rate

Changing the airflow rate is also investigated as an airflow design strategy to reduce the dispersion of the airborne contaminant in the cabin. The original cabin airflow rate adopted in [29] is 200 L s^{-1} with each of the two inlets providing an equal rate of 100 L s^{-1}. Two cases for airflow rate increase are considered: 100% increase (airflow rate = 400 L s^{-1}) and 50% increase (airflow rate = 300 L s^{-1}), while a single case of airflow rate decrease of 50% (airflow rate = 100 L s^{-1}) is investigated. This is inspired by multiple studies in the literature that investigated the increase and/or the decrease of the ventilation airflow rate supplied to commercial aircraft cabins as means of controlling airborne contaminant dispersion and

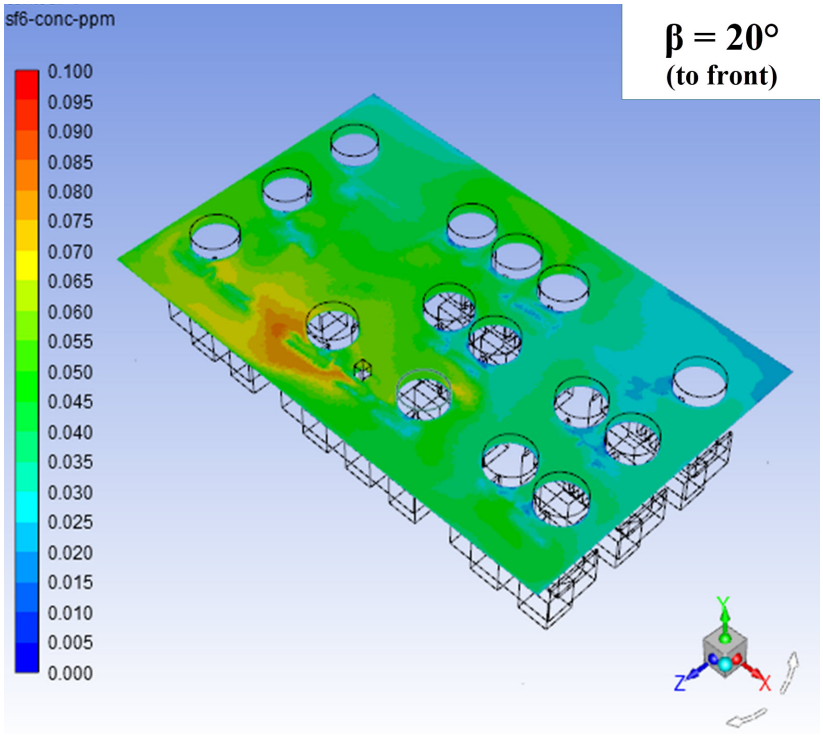

(a)

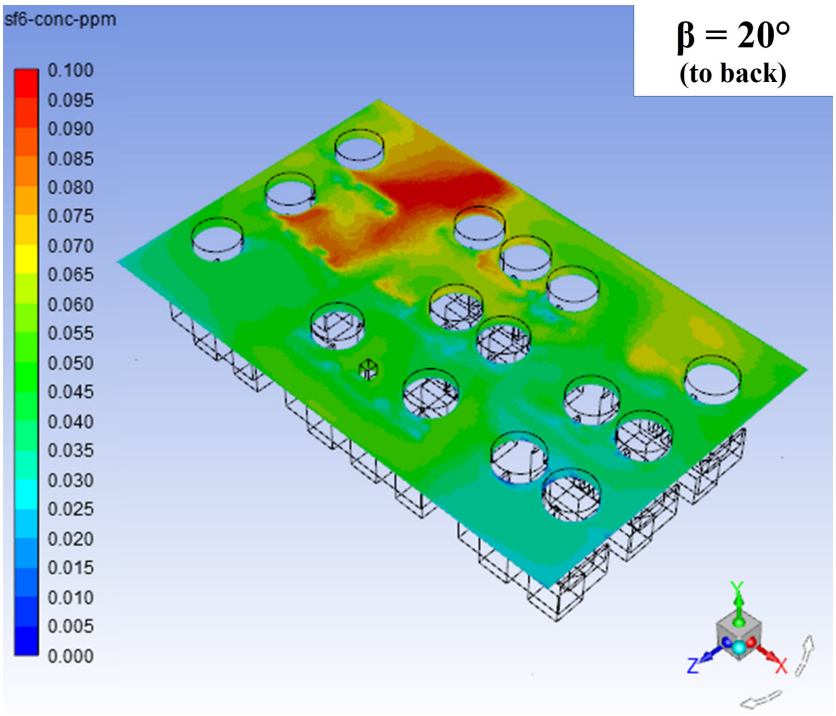

(b)

Figure 5.6: SF_6 concentration contour plots at passenger breathing level during steady flight at 350 s; (a) using airflow supply angle $\beta = 20^\circ$ to the front, and (b) using airflow supply angle $\beta = 20^\circ$ to the back.

enhancing the air quality conditions [91, 92, 101]

Figure 5.7 shows a comparison of the three SF_6 concentration time series under the modified airflow rate conditions with the default 200 L s^{-1} case during the steady level flight leg.

As can be noticed from comparing the concentration time series, none of the three airflow rate change cases provided consistent air quality enhancement at the two monitoring locations. The 100% more airflow led to reduced peak concentration at seat A7, but it increased the exposure more than three-fold its counterpart during the steady flight case at seat C7. The 50% less airflow led to nearly the same exposure as of that for the steady flight case at the two seats with a tendency of exposure increase at later simulation times. Nevertheless, the 50% more airflow case was only able to reduce the passenger exposure to about 50% of that for the original steady flight case at seat C7, but at seat A7, it increased the exposure more than three-fold its original level.

This controversy in results provided by the three different airflow rates is caused by the non-uniform contaminant concentrations induced by the complex airflow patterns and highly turbulent vortex shedding in the heavily occupied aircraft cabin space motivated by the strong vertical thermal plumes released from occupants' bodies [66]. This condition perfectly describes the dispersion behavior of the cough-released contaminant in the aircraft cabin where using a higher airflow rate may not always lead to decreased average concentration for an airborne contaminant [34, 91], but it could increase the dispersion of such contaminant instead [82]. Figure 5.8 illustrates the relative dispersion of the contaminant in the cabin at 350 s after release using contours of the three studied cases.

From Figure 5.8, it can be seen that both the 100% more airflow and the 50% more airflow tend to push the contaminant to the back of the cabin as time passes after its release. However, and although the 100% more airflow exhibit longitudinal contaminant dispersion from one row to the other, the 50% more airflow causes a mixed longitudinal and lateral dispersion behavior for the contaminant motivated by the less airflow velocities in the cabin in this case. On the other hand, the 50% less airflow favor to disperse the contaminant evenly in the cabin space with tendency to push it to the front rows at the end of simulation time. This is mainly attributed to the cough dispersion direction (to the front of the cabin) being more dominant over the overall airflow direction with the very low airflow velocities in the cabin under the 50% less airflow rate condition. Those contaminant dispersion mechanisms can be evidently noticed by analyzing the SF_6 concentration contour plots and the time series at seats A7 and C7 shown in Figure 5.7.

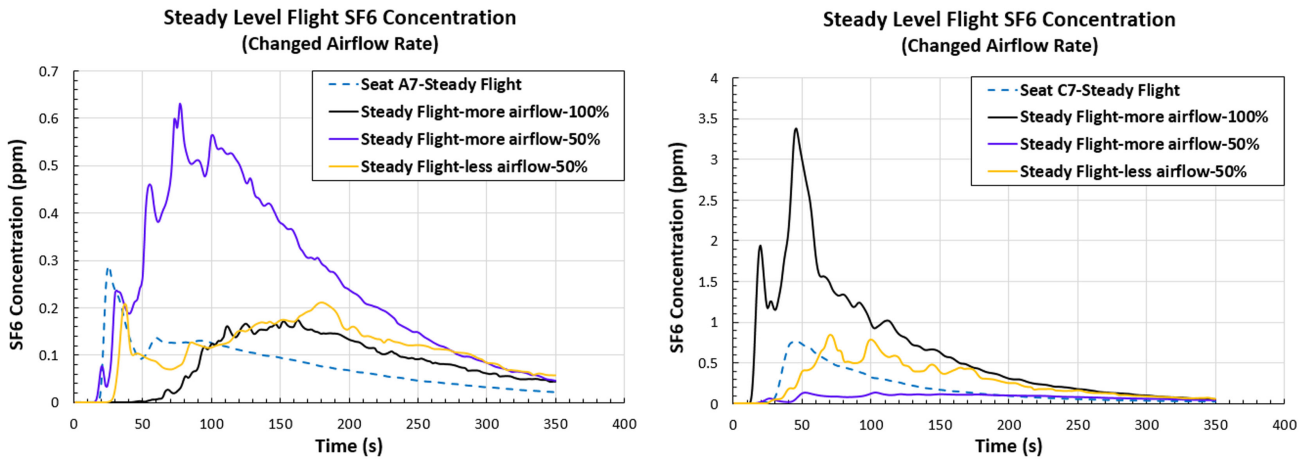

(a) (b)

Figure 5.7: Comparison of the predicted SF_6 concentration time series during the steady level flight leg using 100% more, 50% more, and 50% less supply airflow rates with respect to the original steady level flight flow rate; (a) at seat A7, and (b) at seat C7.

Similar results have been reported by Wang et al. [92] when they changed the base ventilation airflow rate in the Boeing 767 aircraft cabin mock-up model from 1052 $m^3\ h^{-1}$ (292 L s^{-1}) to 736 $m^3\ h^{-1}$ (204 L s^{-1}), 816 $m^3\ h^{-1}$ (226 L s^{-1}), 949 $m^3\ h^{-1}$ (264 L s^{-1}), and 1259 $m^3\ h^{-1}$ (349 L s^{-1}). This corresponds to 70%, 80%, 90%, and 120% of the base airflow rate. The researchers found that the increase or decrease of the supplied ventilation airflow rate did not affect the overall CO_2 airborne contaminant surrogate concentration in the cabin space, and therefore, did not contribute to better air quality condition for the passengers.

In an analogous manner, Yan et al. [101] changed the rate of the supplied airflow to a 767-300 cabin mock-up model to 80% and 120% of the original 1052 $m^3\ h^{-1}$ (292 L s^{-1}) airflow rate as recommended by the Boeing company guidelines. They found that increasing or decreasing the airflow rate in the cabin did not necessarily benefit the passengers in terms of better air quality conditions or decreased CO_2 contaminant surrogate concentration. They also noticed that the air quality condition was completely unchanged for the receptor(s) close to the contaminant release source with the airflow rate changes.

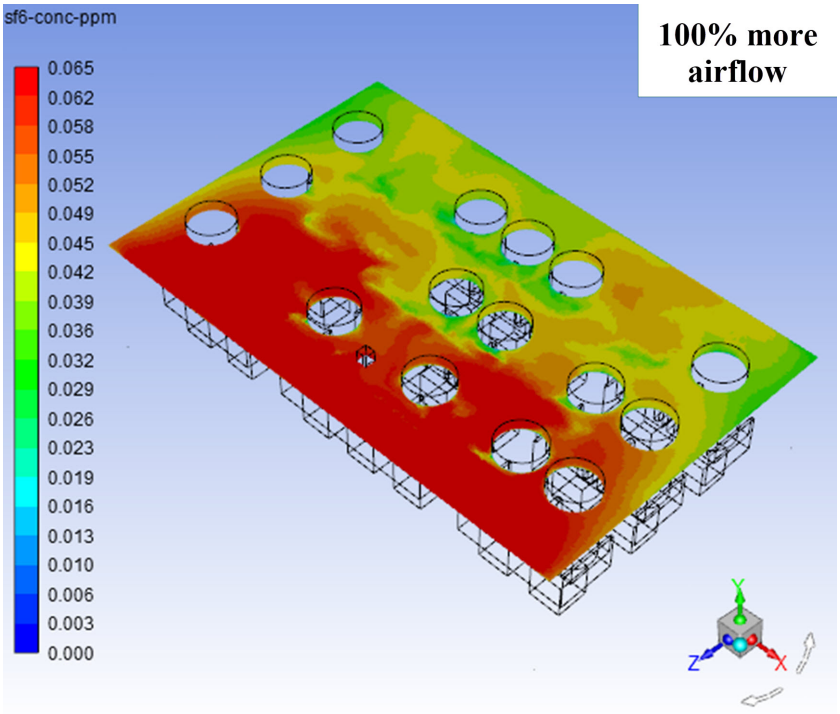
sf6-conc-ppm
0.065
0.062
0.058
0.055
0.052
0.049
0.045
0.042
0.039
0.036
0.032
0.029
0.026
0.023
0.019
0.016
0.013
0.010
0.006
0.003
0.000
100% more airflow
Y
Z
X

(a)

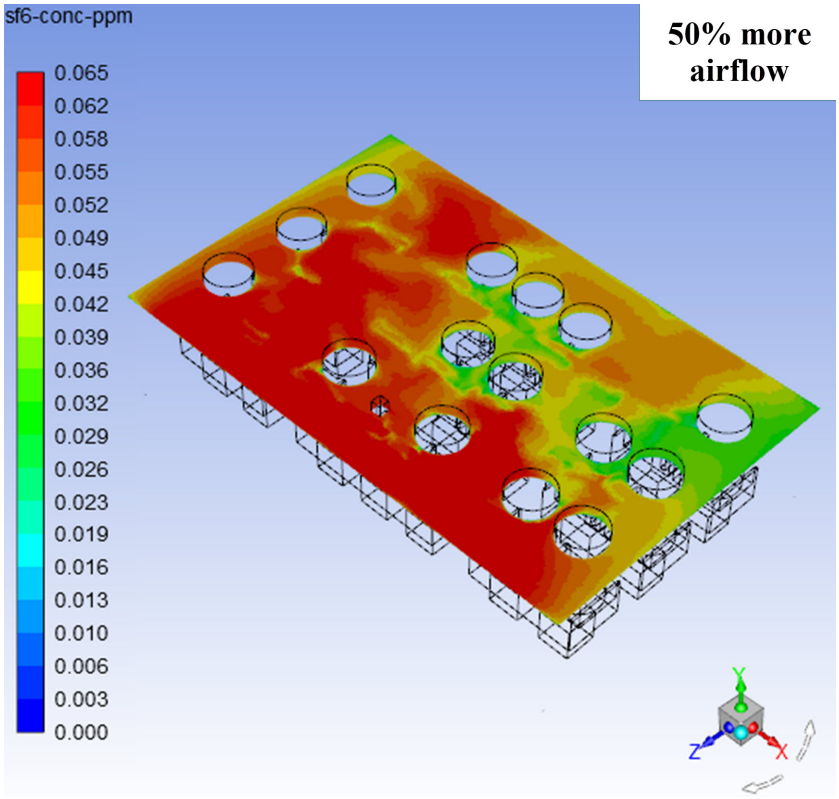
sf6-conc-ppm
0.065
0.062
0.058
0.055
0.052
0.049
0.045
0.042
0.039
0.036
0.032
0.029
0.026
0.023
0.019
0.016
0.013
0.010
0.006
0.003
0.000
50% more airflow
Y
Z
X

(b)

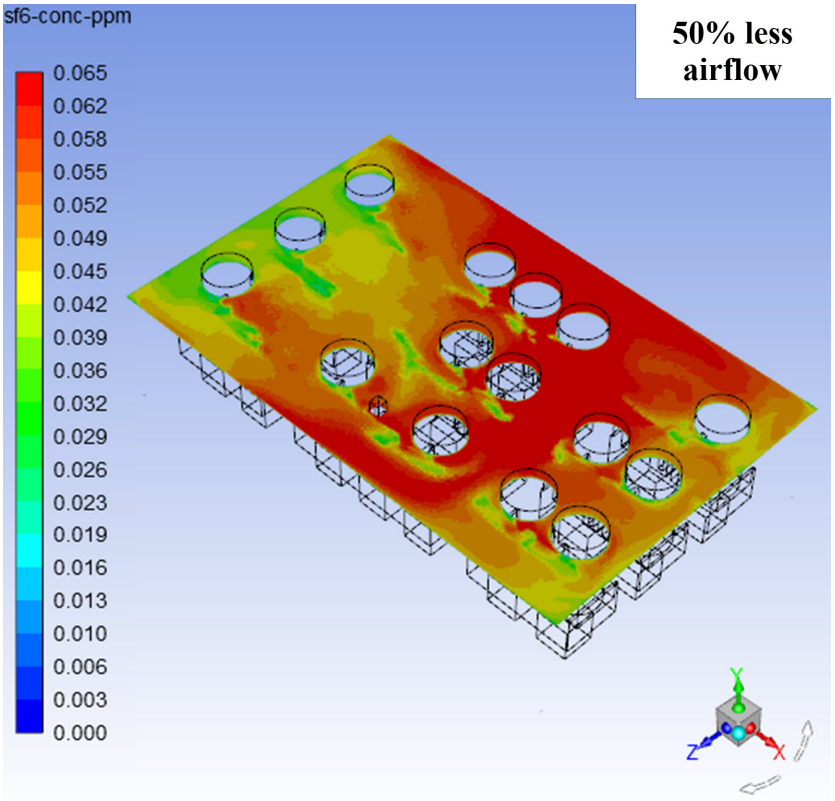

(c)

Figure 5.8: SF_6 concentration contour plots at passenger breathing level during steady flight at 350 s; (a) using 100% more airflow rate, (b) using 50% more airflow rate, and (c) using 50% less airflow rate.

5.2 Source Control Strategies

5.2.1 Cough Direction

Altering the direction of the cough leads to changing the injection orientation for the airborne contaminant in the cabin and can significantly affect its dispersion behavior based on the different surfaces and/or walls the cough stream would encounter with every different orientation. In this investigation, the cough direction will be tilted vertically with specified angles either downwards or upwards from the horizontal, but not sideways. This is supported by multiple studies in the literature [39, 42] that suggest that most of the coughs are directed downwards at the human mouth with two angles ranging from 10° to 20° for the upper angle (between the cough stream and upper lip), and from 36° to 44° for the lower one (between the cough stream and lower lip).

The angles used in this study are 30° and 40° downwards, in addition to 30° upwards. The 30° downwards angle is used as an average to the reported angles by Gupta et al. [39]. However, the other two angles are utilized to investigate the effect of increasing the cough downward tilt angle and the effect of directing the cough upwards on the contaminant dispersion behavior in the cabin, respectively. Figure 5.9 graphically illustrates the two cough orientations; downwards and upwards, employed in the current investigation. Next, Figure 5.10 shows the SF_6 concentration time series calculated at the two monitoring positions in the cabin for the three cough direction angles used.

From Figure 5.10, the calculated concentration time series for the 30° downwards and 40° downwards are almost fully coincident. This indicates that increasing or decreasing the cough direction angle for the same cough orientation has no substantial effect on the dispersion pattern of the released contaminant in the cabin. However, when the cough was directed upwards using $\theta = 30^\circ$ the exposure was higher than the ones for the downwards cough direction, especially at seat A7 at the front of the cabin. Figure 5.11 clearly shows the difference between the SF_6 contour plots in the cabin under the 30° downwards and 30° upwards cough release conditions.

The outcome from the comparison in Figure 5.11 agrees well with the concentration time series in Figure 5.10.

Releasing a cough with 30° upwards leads to higher concentration of the delivered contaminant at the breathing level of the passengers in the majority of the cabin space especially on the left side (looking to the front). In comparison, the cough released by the same index person at 30° in the downward direction created a minor intensification pattern of the

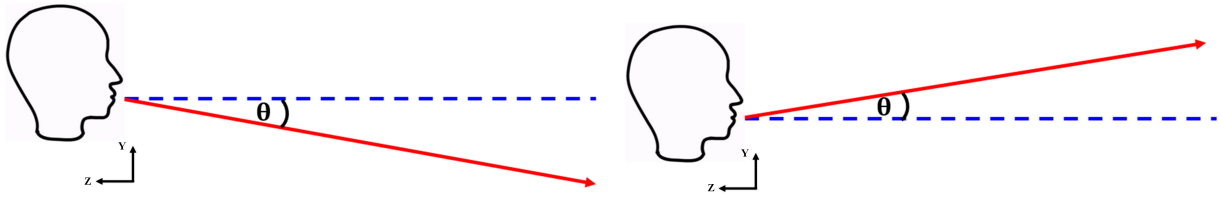

(a) (b)

Figure 5.9: The two cough orientations used in the current study; (a) downwards cough, and (b) upwards cough, where θ is the cough inclination angle.

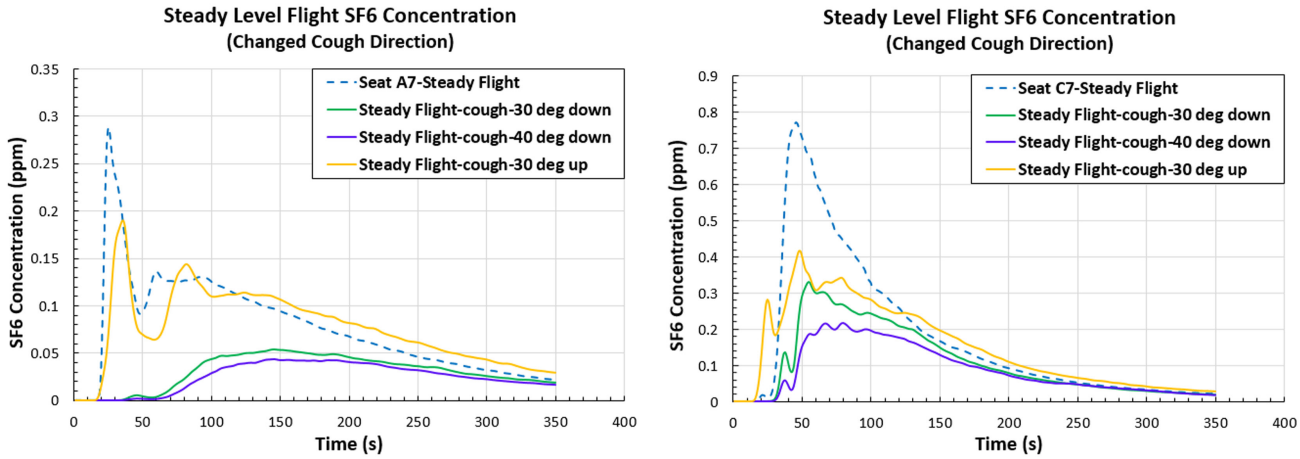

(a) (b)

Figure 5.10: Comparison of the predicted SF_6 concentration time series during the steady level flight leg using the 30° downwards, 40° downwards, and 30° upwards cough direction angles; (a) at seat A7, and (b) at seat C7.

contaminant at the back of the cabin on the left side, as well, but with much diluted concentrations everywhere else.

This increase in the SF_6 concentration, and consequently the passenger exposure, for the upward-directed cough is attributed to that the cough encounters almost no obstacles on which the released contaminant may impact in this case. Also, in this manner, the contaminant is primarily dispersed from the top of the cabin to the bottom. This significantly enhances the contaminant dispersion and mixing in the cabin aided by the stronger airflow eddies located close to the ceiling induced by the thermal plumes released from the bodies of the occupants leading to a mixed convection (natural convection plus forced convection) condition in the cabin. These findings can render directing the cough at the release point as one of the most effective source control strategies for the reduction of expiratory airborne contaminants in enclosed spaces such as aircraft cabins.

5.2.2 Cough Velocity (Volumetric Flow Rate)

Another source control strategy investigated in the current study is the cough velocity or volumetric flow rate. Such variances in cough attributes are naturally existent among people of different body sizes, age, gender, and health conditions.

For example, males have a higher Cough Peak Flow Rate (CPFR) and Cough Expiratory Volume (CEV) on average than females. In a thirteen-male and twelve-female sample, the CPFR ranged from 3 to 8.5 L s^{-1} for males and from 1.6 to 6 L s^{-1} for females, while the CEV was anywhere from 400 to 1600 mL and 250 to 1250 mL for males and females, respectively [39].

Additionally, the cough velocity or volumetric flow rate can be effectively altered at the source using simple habits, such as putting a hand on a person's mouth while coughing or using napkins to obstruct the cough from releasing in the space.

In this study, the investigation of the effect of altering the cough velocity/volumetric flow rate on the dispersion behavior of the released contaminant in the cabin is conducted using two approaches: variable cough release velocity, and fixed released contaminant mass.

The first approach concentrates on changing the cough volumetric flow rate by changing the release velocity of the cough only as the mouth opening area is kept fixed in all cases. The cough velocity is set to two quantities; a low velocity of 5 m s^{-1} and a high velocity of 20 m s^{-1} as compared to the cough velocity in the original studies [29, 91] of 10.6 m s^{-1}. Such high and low cough outlet velocities have been reported and employed in multiple studies in

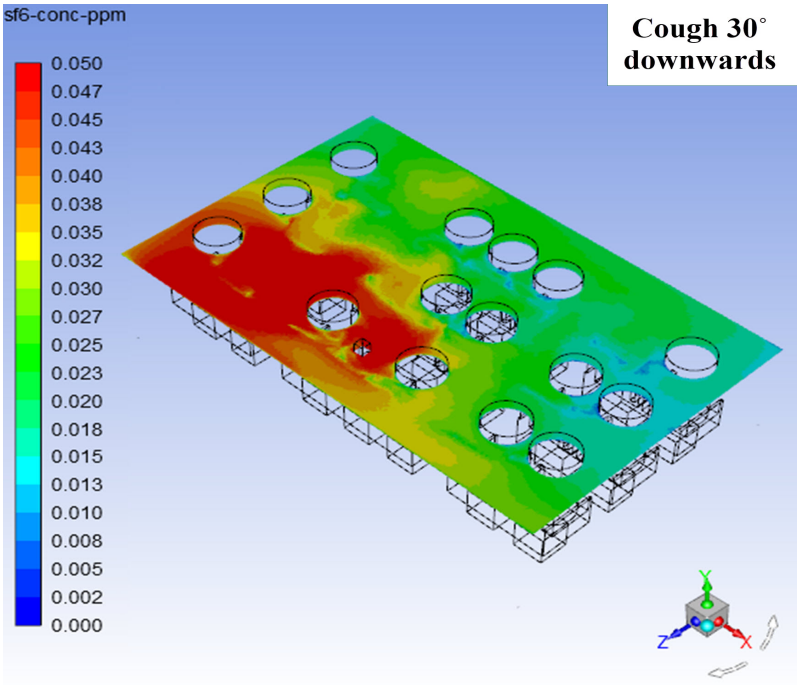

(a)

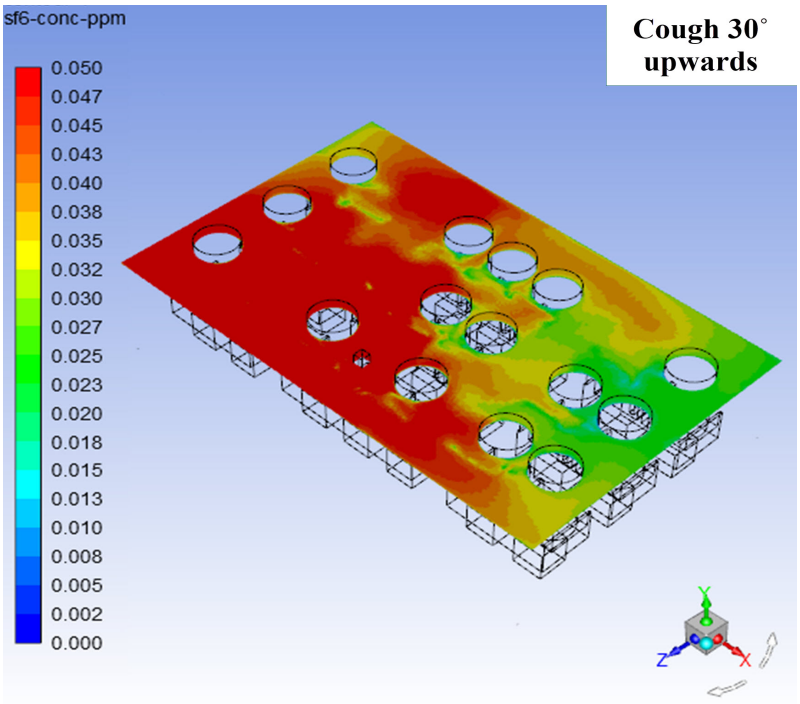

(b)

Figure 5.11: SF_6 concentration contour plots at passenger breathing level during steady flight at 350 s; (a) using cough direction angle $\theta = 30°$ downwards, and (b) using cough direction angle $\theta = 30°$ upwards.

the literature [35, 39, 115]

Alternatively, through the fixed released SF_6 mass approach, the mass of the injected SF_6 in the cabin is kept fixed between the new and original cases. This is achieved by changing any two or more variables on the right-hand side of equation 5.1 together to keep the contaminant mass (M) on the left-hand side constant,

$$M = C\ A\ V\ T, \tag{5.1}$$

where C is the contaminant concentration at the release point (mouth), A is the cross-sectional area of the mouth (≈ 0.4 cm^2), V is the cough release velocity, and T is the cough time duration. Because C and A are not changed between cases, T is only to be altered with V in an inversely proportional manner. The results for each approach are shown in the following subsections.

Variable Cough Release Velocity

Figure 5.12 depicts the concentration time series resulting from the high cough release velocity (20 m s^{-1}) and the low cough release velocity (5 m s^{-1}) in comparison to the baseline steady flight case with 10.6 m s^{-1} cough velocity.

Releasing the cough with the high velocity of 20 m s^{-1} during the steady level flight leg led to decreased contaminant concentration compared to the original velocity of 10.6 m s^{-1} for the majority of the simulation time. This decrease can be attributed to the ability of the higher velocity coughs to quickly disperse in the cabin space, impact the cabin envelop, and reach the exhaust slots in considerably less time than the lower velocity coughs. In this manner, the released contaminant from high velocity coughs is less likely to settle in a specified location in the cabin for long time causing lower local concentrations to be predicted at different locations.

On the other hand, the contaminant concentrations resulting from the lower cough release velocity (5 m s^{-1}) are noticed to be less than that for the higher cough velocities at earlier times after release. However, after 100 to 150 s following the contaminant release, the concentrations surpass that for the 20 m s^{-1} at the two monitoring locations. This can be caused by the weak momentum of the lower velocity cough, which makes the dispersion of the released contaminant slow, and allows it to remain longer in the cabin. This indicates that a delayed increase in the passenger exposure to the contaminant after release may occur under the steady flight condition with lower velocity coughs.

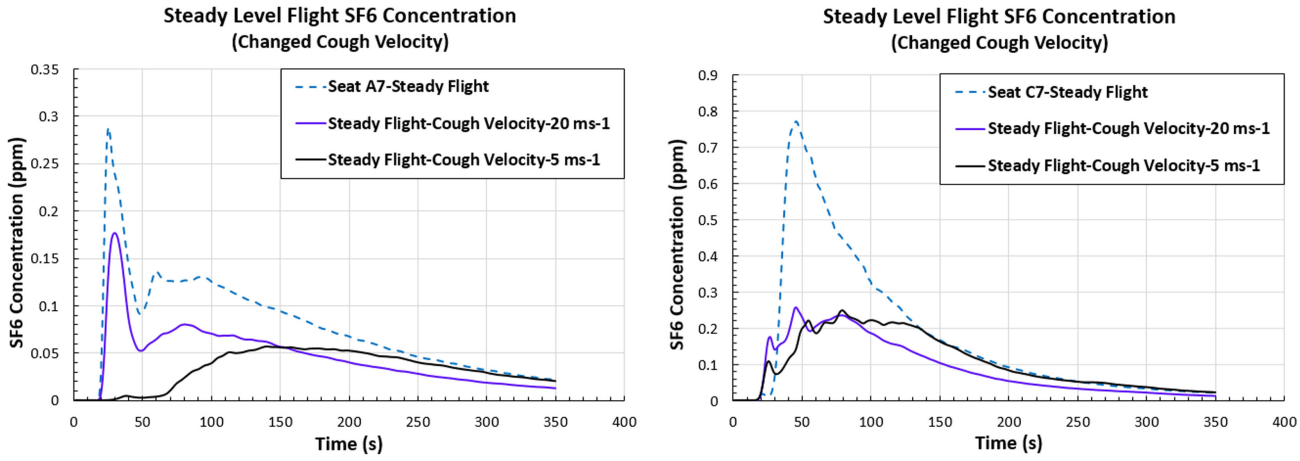

(a) (b)

Figure 5.12: Comparison of the predicted SF_6 concentration time series during the steady level flight leg using the 20 m s^{-1} and 5 m s^{-1} cough release velocities; (a) at seat A7, and (b) at seat C7.

The cabin-wide contaminant concentration contours under the three cough velocity conditions are shown in Figure 5.13. It can be noticed that the dispersion pattern of the contaminant in the cabin is almost identical between the 5 m s^{-1} and 10.6 m s^{-1} cough velocity cases after 350 s following the cough release. For both cases, the contaminant concentration is mainly intensified at the back row and in the whole left side of the cabin (looking to the front). This major contaminant intensification pattern follows the strong dilution of the contaminant in the cabin air induced by the potent ventilation airflow circulation and high velocities, which are dominant over the low contaminant dispersion velocities under the 5 m s^{-1} and 10.6 m s^{-1} cough velocity conditions.

On the other hand, for the 20 m s^{-1} cough, the overall concentration of the contaminant in the cabin space was low (under 0.02 ppm) at the end of simulation time. However, some minor contaminant concentration pattern is noticed at the back-left side of the cabin following the venting of most of the contaminant mass out of the cabin space through exhaust slots.

Among the three cough velocity cases, and under the steady flight condition, the higher velocity cough (20 m s^{-1}) provided a slightly enhanced air quality in the cabin over the other two cases. This is based on the short-lived peak increase in the contaminant concentration after release, and its rapid decrease with time afterwards.

Fixed Released SF_6 Mass

With an alternative approach, the mass of the released SF_6 from the cough in the cabin, as per equation 5.1, is kept fixed. This is attained by doubling the cough release velocity from the baseline case of 10.6 m s^{-1} to 21.2 m s^{-1}, and reducing the cough release duration to 0.5 s instead of 1 s. In this way, the effect of changing the contaminant mass in the cabin can be ruled out. Figure 5.14 shows the SF_6 concentration time series at the two monitoring locations, and the SF_6 contour plots in the cabin for this approach.

From the concentration time series, it can be seen that the contaminant concentration at the two measuring points was extremely low for the whole simulation time when the cough release velocity was doubled and its duration was halved. Moreover, the contour plots for the same condition show a small concentration as low as 0.005 parts per million (ppm), which is about 20% only of the average contaminant concentration predicted in the cabin for the 5 m s^{-1} and 20 m s^{-1} cough velocity cases in the previous subsection (Variable cough release velocity).

Although this approach fixes the released contaminant mass from the cough whatever the release velocity, the uncommon reduction in the average contaminant concentration in the cabin can be attributed to the weak cough impulse and momentum at the release point. In spite of the increased cough velocity, this weak cough impulse is caused by the significantly decreased cough duration to 0.5 s. This creates a cough that is not fully developed, and therefore, can be quickly diminished by the strong and ventilation airflow eddies in the cabin.

Based on these findings, the simulated cough in this case cannot be considered a practical representation of the actual coughs released in the aircraft cabin space. However, if such coughs exist, they would pose minimal risk on the health of the occupants upon exposure.

5.2.3 Cougher Location in the Cabin

In this investigation, the location of the cougher was initially evaluated from the back row in the center. To investigate the effect of cougher location on the cough-released contaminant dispersion in the cabin, two additional locations are utilized; at the central row on the left side (LC) and the front row on the right side (RF), looking from the back of the cabin to the front. The new cougher locations with respect to the original case are shown in Figure 5.15.

This source control approach based on changing the location of the source in the cabin is

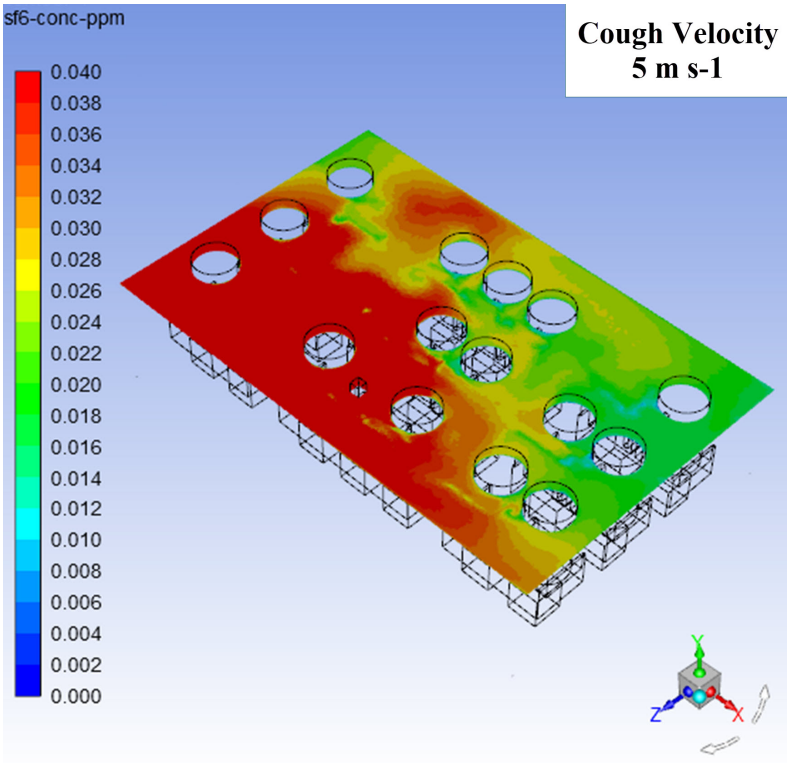
sf6-conc-ppm
0.040
0.038
0.036
0.034
0.032
0.030
0.028
0.026
0.024
0.022
0.020
0.018
0.016
0.014
0.012
0.010
0.008
0.006
0.004
0.002
0.000
Cough Velocity
5 m s-1
Y
Z
X

(a)

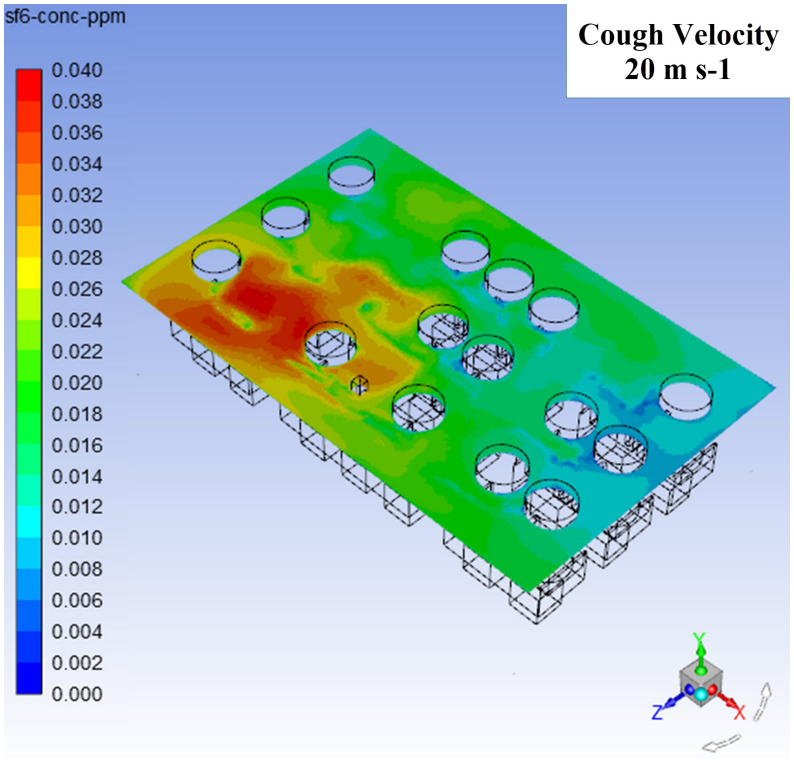
sf6-conc-ppm
0.040
0.038
0.036
0.034
0.032
0.030
0.028
0.026
0.024
0.022
0.020
0.018
0.016
0.014
0.012
0.010
0.008
0.006
0.004
0.002
0.000
Cough Velocity
20 m s-1
Y
Z
X

(b)

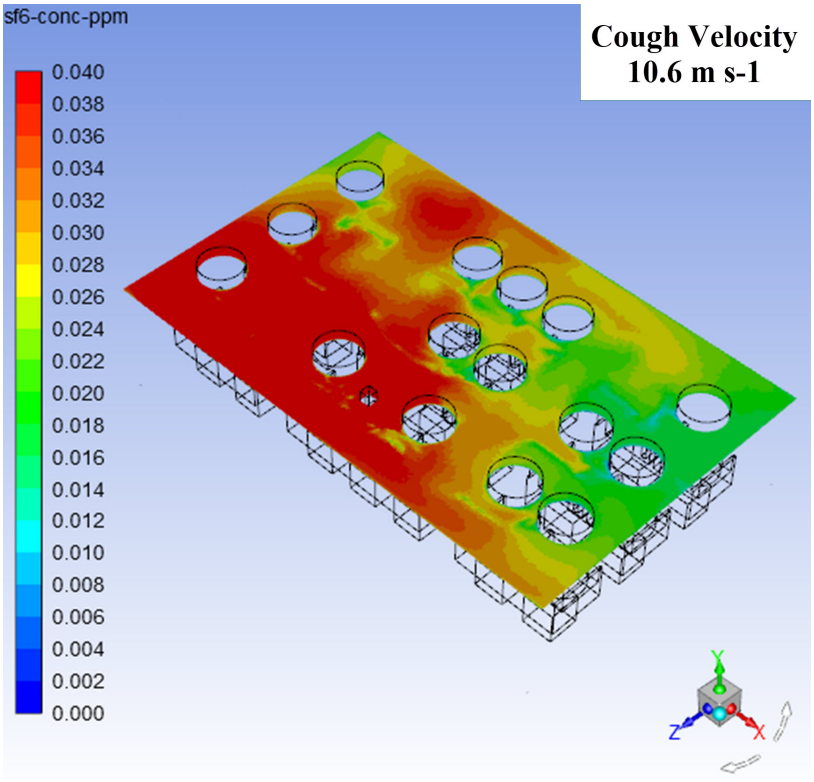

(c)

Figure 5.13: SF_6 concentration contour plots at passenger breathing level during steady flight at 350 s; with (a) 5 m s^{-1} cough velocity, (b) 20 m s^{-1} cough velocity, and (c) 10.6 m s^{-1} cough velocity.

inspired by similar investigations performed in aircraft cabin models in the literature [53, 54].

Figures 5.16 and 5.17 depict the SF_6 concentration time series at the two seats A7 and C7 with the cougher positions at locations LC and RF, respectively. The series for the two cases were separated to enhance their readability.

Based on the concentration time series, the contaminant concentration at each monitoring point is significantly affected by the cougher location. For example, as the cougher moves to the LC location, the concentration at seat C7 for the full simulation time was significantly reduced to the 0.1 ppm level. At seat A7, however, a sharp decrease in the contaminant concentration from the original case is noticed early after release, but it quickly bounces back around 100 s to a higher concentration (almost the double) till the end of the simulation time.

On the other hand, as the cougher set at the RF location is very close to the monitoring point at seat A7, the contaminant concentration increased very substantially to about eighty-fold its maximum value during the baseline climb case as shown in Figure 5.17(a). While, at seat C7, the contaminant time-averaged concentration was much lower in the RF cougher location scenario than the baseline case (about one-third of it) because the cougher was moved further away from its location.

In addition to the effect of cougher proximity to other occupants, the ventilation airflow patterns in the cabin and/or the existence of walls or surfaces close to the cougher location have significant influence on the dispersion behavior of the released contaminant in the cabin by impacting or redirecting the cough. Such influence can be inferred from the SF_6 concentration contour plots for the two cougher location cases illustrated in Figure 5.18.

Looking at the contour plot for the LC cougher location, the contaminant is noticed to be evenly distributed in the cabin space with limited spots of some relatively higher concentration at the front and the back of the cabin on the left side where the cougher was relocated.

On the other hand, the contaminant released from the cougher in the RF position follows along the frontal cabin separator (wall) to the left before it disperses to the back rows with the help of airflow mixing. This leads to higher contaminant concentration regions in the frontal section of the cabin, and consequently, more exposure of the occupants to the contaminant. According to this finding, a coughing person aboard an aircraft may not only cause higher probability of exposure to the passengers nearby, but also to most occupants in the cabin if this person is coughing in close proximity to a wall or surface.

Looking at the literature, similar contaminant surrogate dispersion behavior has been

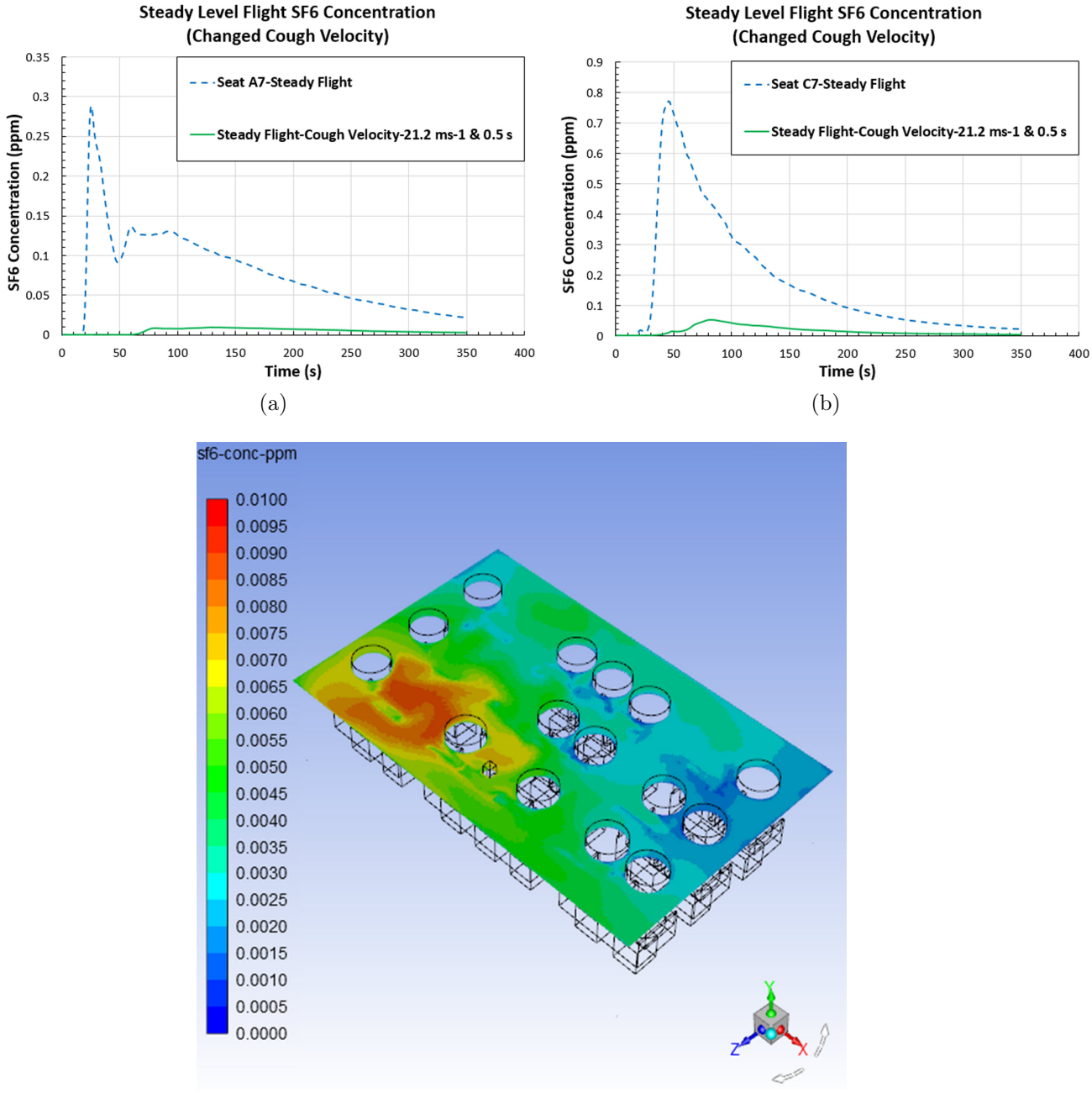

Figure 5.14: Predicted SF_6 concentration time series during the steady level flight leg using the 21.2 m s^{-1} cough release velocity for 0.5 second duration; (a) at seat A7, and (b) at seat C7, and (c) the SF_6 contour plot at passenger breathing level during steady level flight at 350 s for the same case.

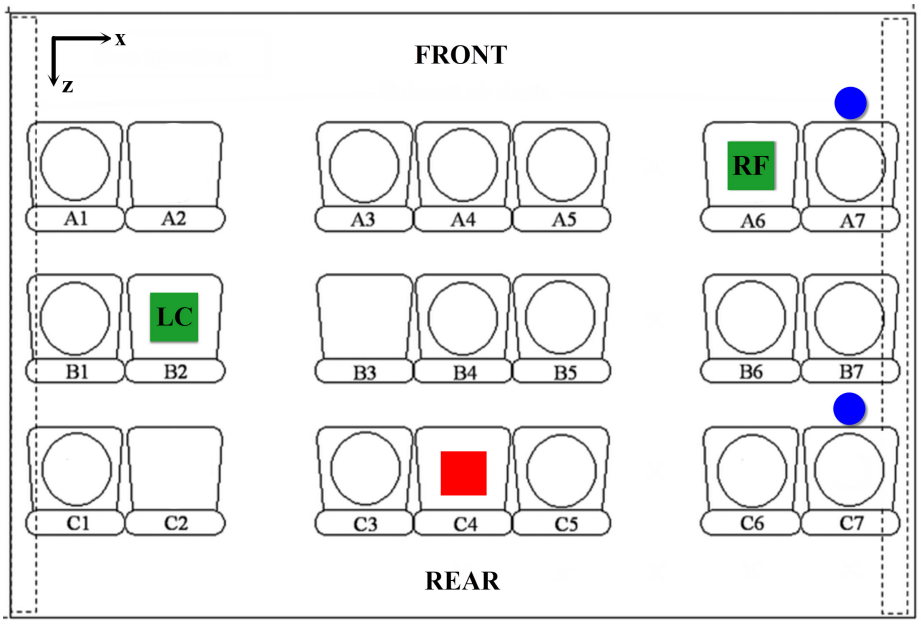

Figure 5.15: New cougher locations with respect to the original location (red square). First location is on the left side at center row (LC), and the second is on the right side at the front row (RF).

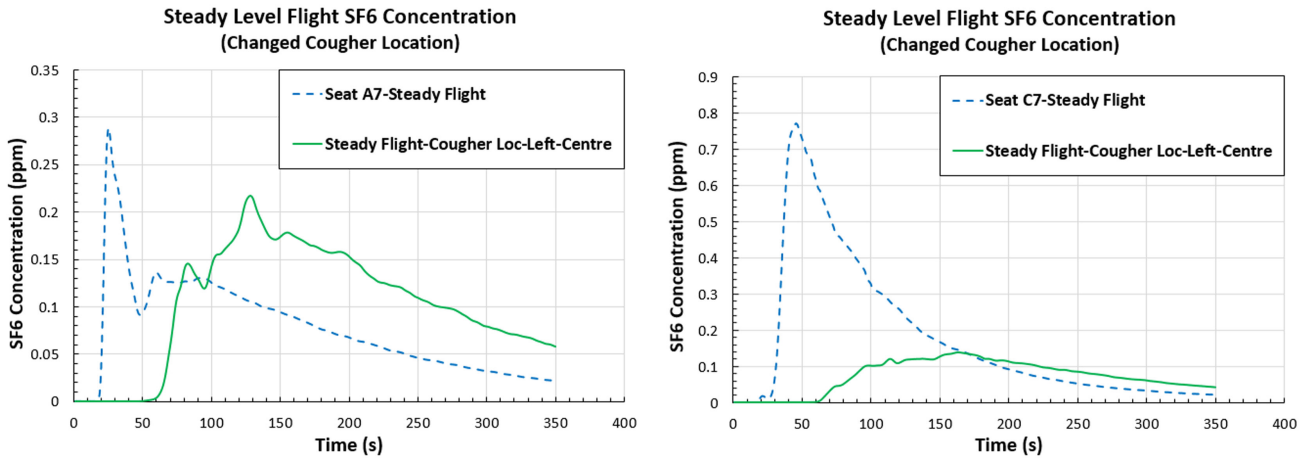

(a) (b)

Figure 5.16: Comparison of the predicted SF_6 concentration time series during the steady level flight leg with the cougher moved to the center row on the left side of the cabin; (a) at seat A7, and (b) at seat C7.

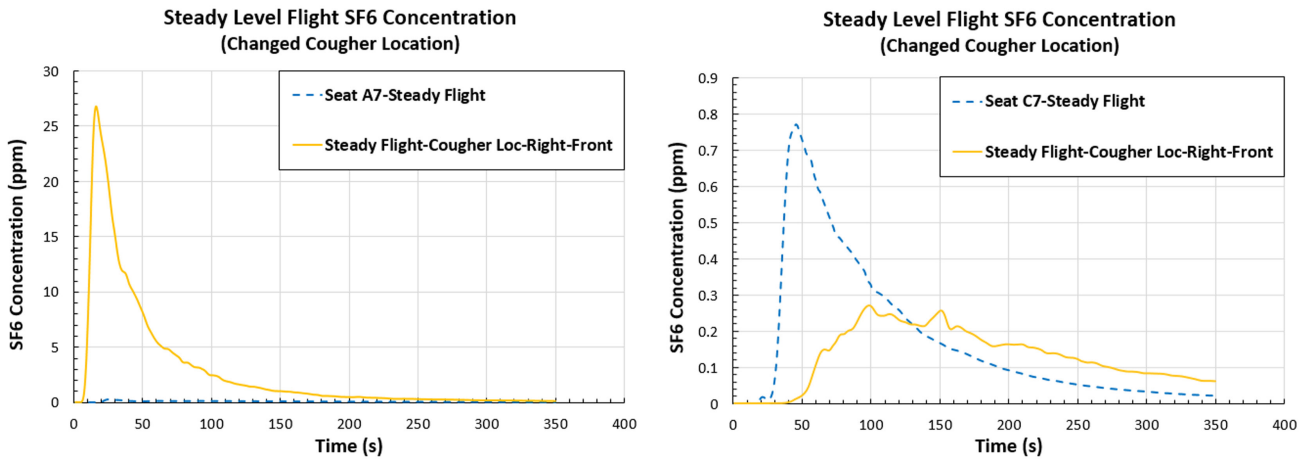

(a) (b)

Figure 5.17: Comparison of the predicted SF_6 concentration time series during the steady level flight leg with the cougher moved to the front row on the right side of the cabin; (a) at seat A7, and (b) at seat C7.

reported by different investigators when the location of the contaminant release source was changed during the steady level flight leg.

Li et al. [53] reported that the simulated SF_6 contaminant surrogate majorly settled on the left side at the back of the MD-82 aircraft cabin (looking to the front) close to the contaminant release source at this location some time after release. Similarly, when the contaminant release source was moved to the front of the cabin on the left side, the contaminant concentration was the highest at the left side of the cabin on a lateral plane passing through the contaminant release point.

Also, in a different study for the effect of airflow vortex structures on airborne contaminant transport, Li et al. [54] placed three point sources for the SF_6 contaminant surrogate release at different locations in the aircraft cabin model. They found that the contaminant concentration tends to intensify on the side of the cabin (right or left) at which the release source is located. Moreover, when the source was set at the center of the cabin close to the back row, the contaminant concentration was higher on the left side of the cabin (looking to the front).

Those findings align well with the contaminant dispersion behavior for the two cases of cougher location change in the cabin. Also, the last finding by Li et al. [54] agrees with the majority of cases in the current chapter during the steady level flight leg in which the SF_6 contaminant surrogate was released from the center seat at the back row and led to major

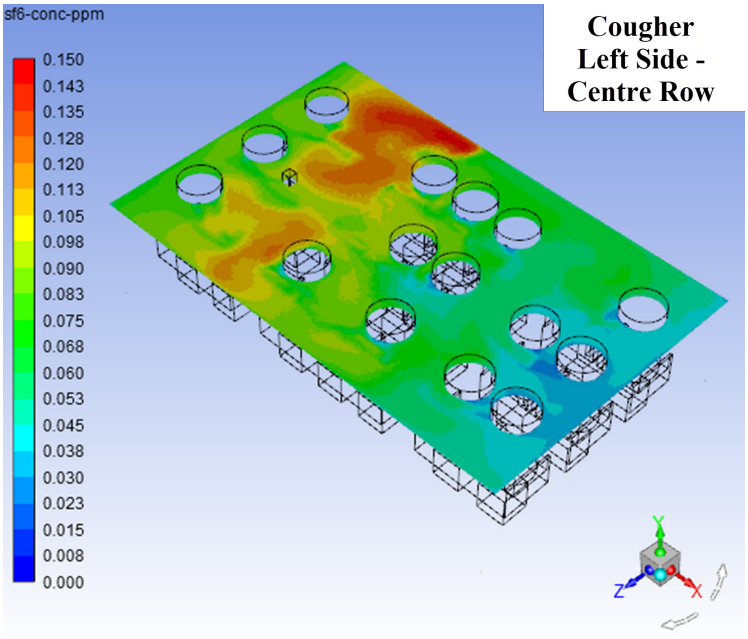

(a)

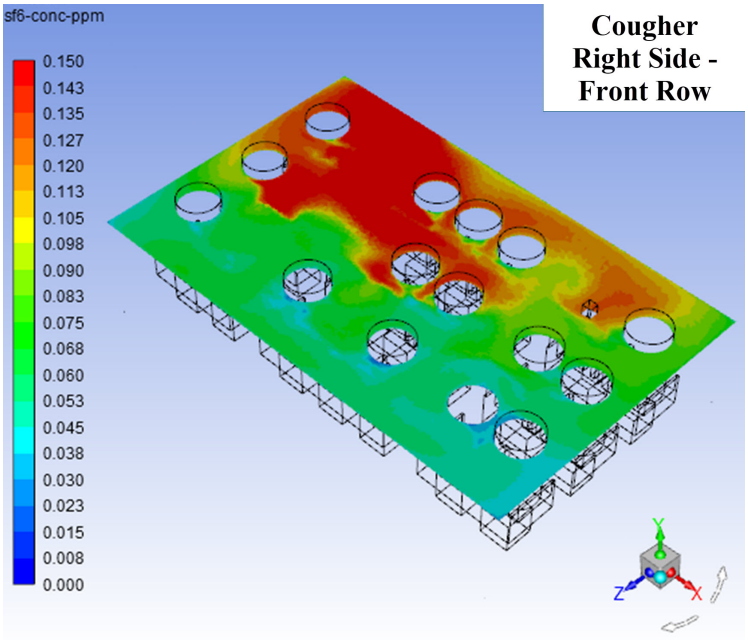

(b)

Figure 5.18: SF_6 concentration contour plots at passenger breathing level during steady flight at 350 s; with (a) the cougher located at the center row on the left side of the cabin, and (b) the cougher located at the front row on the right side of the cabin.

concentration intensification pattern on the left side of the cabin (looking to the front).

Finally, Table 5.1 lists the passenger exposure ratio between the various cases studied in the current chapter and the baseline steady level flight case. The lowest exposure ratios are in bold font.

The passenger exposure to the contaminant over time is assessed by calculating the area under the curve corresponding to each case at seats A7 and C7 using the following integral,

$$\text{Exposure} = \int_0^{350s} C_{SF_6}(t)\ dt, \tag{5.2}$$

where $C_{SF_6}(t)$ is the time-dependent SF_6 concentration for each case in ppm, and the unit for the calculated exposure is ppm s.

Both the composite trapezoidal rule and composite Simpson's rule were employed to obtain approximate solutions for the exposure integral being applied to each of the irregular concentration time series previously shown.

From Table 5.1, the lowest average exposure ratio between the two seats is found for the case in which the cough was directed 40°downwards. This is followed by the 30°downwards cough, the 5 m s^{-1} cough velocity, and the 20 m s^{-1} cough velocity cases.

It can be easily noticed that all of the strategies that led to the lowest passenger exposure ratios during the steady level flight leg are source control strategies. However, no airflow design strategy contributed effectively to the enhancement of the air quality in the cabin during this leg. This can be attributed to the complex and dissimilar airflow patterns noticed among the investigated cases during the steady level flight leg.

Conversely, the highest exposure ratio is noticed for the case in which the cougher is moved to the front row on the right side of the cabin. This is followed by the airflow strategy in which the air supply direction is set to $\alpha = 60°$, and later by the $\alpha = 20°$ and $\beta = 20°$ to the front airflow direction scenario.

Table 5.1: Ratio of passenger exposure between different parametric sensitivity cases and the baseline steady level flight case at the two monitoring locations.

Case	Passenger exposure ratio to baseline steady flight	
	Seat A7	Seat C7
$\alpha = 20°$ airflow	0.4 : 1	1.2 : 1
$\alpha = 30°$ airflow	1.1 : 1	2.1 : 1
$\alpha = 60°$ arflow	3.4 : 1	12.5 : 1
$\alpha = 20°$ and $\beta = 20°$ to front	5.1 : 1	1.5 : 1
$\alpha = 20°$ and $\beta = 20°$ to back	1.6 : 1	0.7 : 1
100% more airflow rate	1.1 : 1	3.8 : 1
50% more airflow rate	3.3 : 1	0.5 : 1
50% less airflow rate	1.5 : 1	1.6 : 1
Cough 30° downwards	**0.4 : 1**	**0.6 : 1**
Cough 40° downwards	**0.3 : 1**	**0.5 : 1**
Cough 30° upwards	1 : 1	0.8 : 1
Cough velocity 20 m s^{-1}	**0.6 : 1**	**0.5 : 1**
Cough velocity 5 m s^{-1}	**0.4 : 1**	**0.6 : 1**
Cougher at left side-center row	1.4 : 1	0.4 : 1
Cougher at right side-front row	36.6 : 1	0.7 : 1

5.3 Conclusions

In chapter 5, airflow design and source control strategies were investigated for their potential for reducing cough-released airborne contaminant exposure in the cabin of a passenger aircraft (Boeing 767-300) during the steady level flight leg. The SF_6 dispersion behavior was analyzed by calculating the concentration time series at two monitoring locations, seats A7 and C7 in the cabin, in addition to SF_6 concentration contour plots at the breathing level of the occupants. The concentration time series were further used to infer the passenger exposure to the contaminant through determining the area under each curve.

The airflow design strategies researched involved altering the supply airflow direction and

changing the supply airflow rate. As well, the source control strategies employed involved changing the cough direction, varying the cough release velocity or volumetric flowrate, and moving the cougher to different locations in the cabin.

Changing the airflow supply angle from the ceiling only, or α, from 20° to 60° had different effects on the SF_6 dispersion behavior in the cabin. The angle $\alpha = 20°$ led to the lowest passenger exposure. However, the 30° and 60° angles, compared to passenger exposure of the baseline climb case with $\alpha = 0°$, resulted in higher passenger exposures. Further, when a three-dimensional approach was introduced to the airflow redirection scenario through the angle β, directing the airflow to the back of the cabin proved to be better than directing it to the front.

The supply airflow rate to the cabin was changed from the baseline 200 L s^{-1} case to 100% increase, 50% increase, and 50% decrease. None of the three airflow rate change scenarios provided consistent air quality improvement at the two monitoring locations: seat A7 and seat C7. The 100% more airflow led to reduced peak concentration at seat A7, but, at seat C7 it increased the exposure more than three time the original during the steady flight case. The 50% less airflow led to nearly the same exposure as of that for the steady flight case at the two seats with a tendency of exposure increase near the end of simulation time. Lastly, the 50% more airflow case was only able to reduce the passenger exposure to about 50% of that for the original steady flight case at seat C7, but it increased the exposure more than three-fold its original level at seat A7.

For the source control strategies, altering the cough direction was effective in reducing the exposure of the passengers to the released contaminant. This is true when the cough was directed downwards either with 30° or 40° from the horizontal direction, although no significant difference in exposure alleviation was noticed between the two angles for the same cough orientation. Conversely, directing the cough upwards led to passenger exposure which is almost identical to that for the baseline steady level flight case with a zero cough angle from the horizontal. This difference in the created exposure between the downwards and upwards cough orientation can be attributed to the ability of the surrounding surfaces and floor to absorb the released contaminant and block its dispersion for the downwards orientation.

Varying the cough release velocity or volumetric rate was achieved in this investigation in two ways: changing the cough release velocity without fixing the contaminant mass, and changing the cough release velocity while keeping the contaminant mass fixed. Adopting the first approach, and on local level at the two monitoring points, the higher cough velocity of 20 m s^{-1} led to reduced contaminant concentration and passenger exposure than the

original velocity of 10.6 m s^{-1}. Also, the lower cough velocity of 5 m s^{-1} led to less passenger exposure than the higher cough velocity case, but only for limited time after the release of the contaminant. At later time, however, the contaminant concentration for the 5 m s^{-1} cough case surpassed that for the 20 m s^{-1} cough case. Nevertheless, cabin-wide, the higher cough velocity of 20 m s^{-1} led to a marginally enhanced air quality condition over the other two cases. On the other hand, for the fixed contaminant mass approach, the produced exposure at the two monitoring locations was unrealistically low. This is because the cough released in 0.5 s instead of 1 s lacked the required impulse to propagate throughout the cabin space, and was too weak to penetrate the strong airflow currents efficiently.

Lastly, relocating the cougher to other locations in the cabin other than the original back-row-center-seat position had a quantifiable effect on the dispersion behavior of the contaminant, and consequently, the exposure. Moving the cougher to the left side of the cabin in the center row (LC location) led to decreased passenger exposure locally at seat C7, but it led to increased exposure at seat A7 after 100 s following the contaminant release from this changed location. On the other hand, moving the cougher to the right side of the cabin in the front row (RF location) caused a substantial increase in the exposure at seat A7, as it is very close to it, while it kept the exposure at seat C7 at a low value. In addition to the proximity of the cougher to specific passengers, the airflow patters in the cabin, and the existence of walls and/or surfaces near the cougher all have confounding effects on the resulted contaminant dispersion behavior from different cougher locations.

Generally, the cases that showed most promising reduction in passenger exposure as an average between the two monitoring locations at seats A7 and C7 with respect to the baseline steady level flight case are: the 40° downwards cough, the 30° downwards cough, the 5 m s^{-1} cough velocity, and the 20 m s^{-1} cough velocity cases. The exposure ratios are 0.3 : 1 at seat A7 and 0.5 : 1 at seat C7 for the first case, 0.4 : 1 at seat A7 and 0.6 : 1 at seat C7 for the second case, 0.4 : 1 at seat A7 and 0.6 : 1 at seat C7 for the third case, and 0.6 : 1 at seat A7 and 0.5 : 1 at seat C7 for the fourth case, respectively. On the other hand, the highest exposure in average between the two seats belongs to the right side-front row cougher relocation case with 36.6 : 1 at seat A7 and 0.7 : 1 at seat C7.

Chapter 6

Acceleration-Induced Body Forces on Passenger Aircraft During the Climb and Descent Legs under Normal and Extreme Operating Conditions

6.1 Aircraft Normal Operating Conditions

6.1.1 Method for Calculating the Acceleration Components for the Climb and Descent Legs under Normal Operating Conditions

A novel dataset based on satellite observations of aircraft positions and flight paths was utilized to estimate the acceleration components of passenger aircraft during climb and descent legs under the normal operating conditions. Those acceleration components were further used to simulate the effects on exposure to expiratory airborne contaminant inside the aircraft cabin.

The utilized actual commercial passenger aircraft traffic satellite data was extracted from the U.S. National Oceanic and Atmospheric Administration (NOAA) website, and more specifically their Aircraft Meteorological Data Relay (AMDAR) satellite system [73]. The AMDAR satellite system data has been successfully used by Zhang et al. [109] for investigation of the diurnal variation of Planetary Boundary Layer (PBL) physical characteristics.

The elevation, latitude, and longitude data for hundred different aircraft; fifty for climb and fifty for descent, have been extracted from NOAA and processed to produce the vertical and horizontal acceleration components during each flight leg. This was made possible by conducting second order curve-fitting (regression) for each aircraft dataset (versus time) and finding the acceleration components using a Python code (in appendix A.2) according to the following equation representing the kinematic equation of motion:

$$d = at^2 + bt + c, \tag{6.1}$$

where d is distance travelled from the origin (vertically or horizontally), t is the time, and a, b, and c are constants. Also, the constant $a = {}^1\!/_2\, a_c$ is related to the average acceleration during the analyzed time of motion, where a_c is either the average vertical (a_v) or average horizontal (a_h) acceleration components.

Figure 6.1 shows the distribution of acceleration components for each of the fifty aircraft during climb and fifty aircraft during the descent legs. The analyzed time of motion is 300 s.

The chosen values for the vertical and horizontal acceleration components used in the climb and descent simulations were taken as the mean values for the fifty aircraft for each type of flight leg (climb or descent). Those acceleration values are (also shown on Figure 6.1): -0.0164 m s^{-2} for the vertical component and 0.217 m s^{-2} for the horizontal component for climb, while for descent, the vertical component is 0.0156 m s^{-2} and the horizontal component is -0.107 m s^{-2}. Note that the gravitational acceleration is removed from these estimates. The signs of the acceleration components represent their direction with respect to the axes set. In the vertical direction, positive accelerations are acting upwards (opposite to gravity), and negative accelerations are acting downwards (with gravity). In the horizontal direction, however, positive accelerations are acting towards the tail of the aircraft, while negative accelerations are acting towards the head of the aircraft.

Appendix B presents examples for recorded passenger aircraft vertical acceleration component data with flight time by two different volunteers aboard actual flights with different aircraft models.

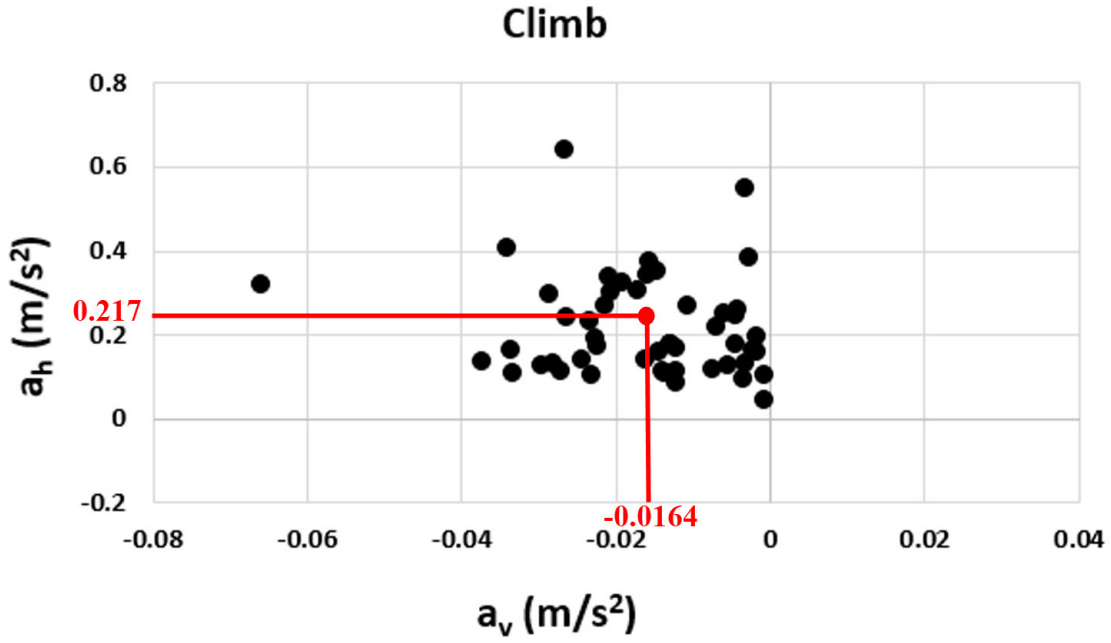

(a)

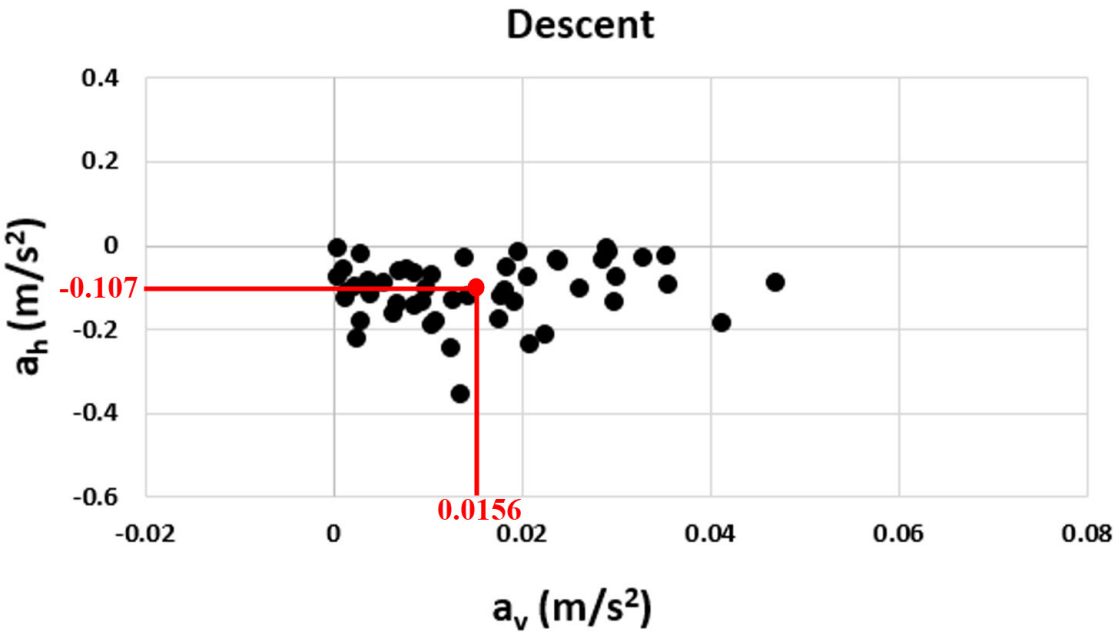

(b)

Figure 6.1: The quantified vertical (a_v) and horizontal (a_h) acceleration components from second order regression of data from fifty different aircraft flights; (a) during climb, and (b) during descent.

6.1.2 Effect on Contaminant Dispersion behavior in the Cabin under Normal Operating Conditions

Two simulations were run; one for the climb case and the other for the descent, using the calculated acceleration components employing the method described in section 6.1.1. This was made possible by defining the acceleration components in the vertical direction (after superimposing the gravitational acceleration with negative sign) and in the horizontal direction in the ANSYS Fluent solver.

The resulting concentration time series of the SF_6 contaminant surrogate in the cabin for the climb and descent legs from the simulations using those acceleration values are referred to as contaminant dispersion behavior under aircraft normal operating conditions at the two monitoring locations; seat A7 and seat C7.

Figures 6.2 and 6.3 depict comparisons of the SF_6 concentration time series in the simulated aircraft cabin model between the baseline steady level flight case (investigated in previous chapters) and the climb and descent cases under the aircraft normal operating conditions.

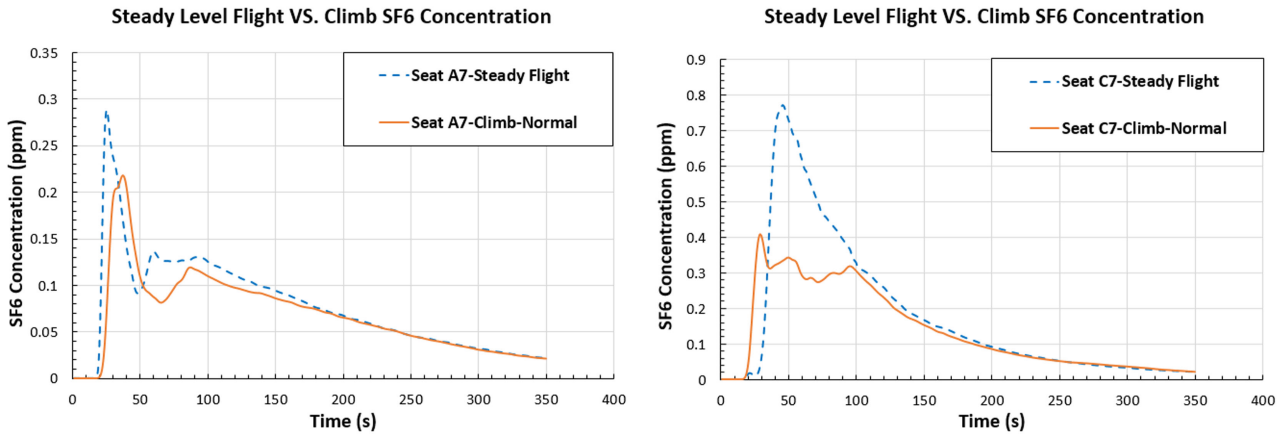

(a) (b)

Figure 6.2: Comparison of the predicted SF_6 concentration time series between the steady level flight case and the climb case under the aircraft normal operating conditions; (a) at seat A7, and (b) at seat C7.

From Figure 6.2, it can be noticed that the SF_6 concentration for the steady level flight leg is evidently higher than that for the climb leg under the aircraft normal operating conditions. This is especially clear at seat C7, at which the peak SF_6 concentration for the steady level

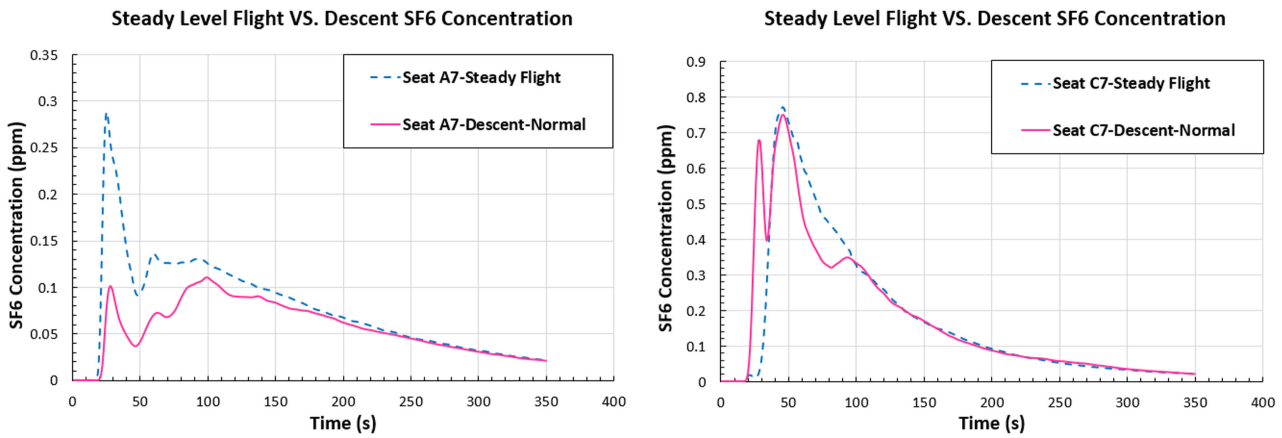

(a) (b)

Figure 6.3: Comparison of the predicted SF_6 concentration time series between the steady level flight case and the descent case under the aircraft normal operating conditions; (a) at seat A7, and (b) at seat C7.

flight case is approximately 50% higher than that for the normal climb case.

On the other hand, from Figure 6.3, the SF_6 concentration time series during descent under the aircraft normal conditions is different between the two locations when compared to that for the steady level flight case. At seat A7, the SF_6 concentration during aircraft normal descent is less than its counterpart for the steady level flight case for most of the simulation time. At seat C7, however, the normal descent's SF_6 concentration time series is very close to that for the steady level flight scenario with some higher SF_6 concentration noticed for the steady level flight between 50 and 100 s after release in the cabin.

The difference noticed between the SF_6 concentration time series for the steady level flight leg and that for the climb and descent legs under aircraft normal operating conditions is primarily influenced by the dissimilar SF_6 dispersion behavior in the cabin among the three flight legs. This is mainly attributed to the variations that occur in the ventilation airflow patterns and circulation in the aircraft cabin space between each of those flight legs affected by acceleration-induced body forces on the aircraft body (more details and in-depth analysis are to follow in section 6.2.2). Those acceleration-induced body forces exist during the climb and descent legs to different degrees depending on the quantities of the aircraft acceleration components.

To present the comparisons in numerical values, Table 6.1 lists the passenger exposure ratios of the climb and descent cases under the aircraft normal operating conditions to the

baseline steady level flight case. The passenger exposures are estimated by calculating the area under each concentration time series curve using equation 5.2.

From Table 6.1, the calculated passenger exposure ratios agree well with the graphical representation for the SF_6 concentration time series in Figures 6.2 and 6.3. Although some clear differences in the passenger exposure exist at seat C7 (at the back of the cabin) between normal climb and steady level flight, and at seat A7 (at the front of the cabin) between normal descent and steady level flight, close agreement is seen in other instances between the steady level flight leg and the normal climb and descent.

In general, the predicted SF_6 dispersion behavior in the cabin during the climb and descent legs under normal aircraft operating conditions does not considerably differ from that for the steady level flight case at some locations in the cabin. However, at other locations, minor change in contaminant exposure among the three legs can be noticed. Consequently, it can be concluded that the acceleration-induced body forces have limited but existent effect on the contaminant dispersion behavior in passenger aircraft cabins during the climb and descent legs under aircraft normal operating conditions.

Table 6.1: Ratio of passenger exposure between climb and descent cases under aircraft normal operating conditions and the baseline steady level flight case at the two monitoring locations: seat A7 and seat C7.

Case	Passenger exposure to baseline Steady Level Flight	
	Seat A7	Seat C7
Climb (Normal Conditions)	0.92 : 1	0.77 : 1
Descent (Normal Conditions)	0.75 : 1	0.99 : 1

6.2 Aircraft Extreme Operating Conditions

6.2.1 Defining the Acceleration Components for the Climb and Descent Legs under Extreme Operating Conditions

For passenger aircraft, extreme events, or extreme operating conditions, of turbulence, gusts, maneuvers, turns, or landings can commonly be encountered during flights. For such events, the load factor on the aircraft body (defined as the ratio between the lift force to the gross weight of the aircraft) can range all the way from less than 1 G to 6 G, where G is the

gravitational acceleration (9.81 m s^{-2}) [87]. Also, the Code of Federal Regulations (CFR) necessitate that any aircraft structure should be capable of withstanding one and one-half times those mentioned load factors without failure. This 1.5 load factor rule (or 1.5 load limit factor) is called the "factor of safety" for designing aircraft structures [87]. In spite of that, the range of expected load factors under extreme operating conditions up to 6 G is very wide, and more specific values should be picked for the aircraft acceleration components during the climb and descent legs under those conditions. Therefore, for the simulations performed in chapters 6 and 7, the vertical and horizontal aircraft acceleration components during the climb and descent legs are specified to simulate an extreme condition of gusty flight. For the climb leg under aircraft extreme operating conditions, the vertical acceleration component is taken as 2.5 G (including gravitational acceleration) and the horizontal component as 0.7 G. For the descent under the same conditions, on the other hand, the vertical acceleration component is assumed to be 0.5 G and the horizontal component to be 0.3 G. Those acceleration components correspond to load factors in the range previously indicated.

Although the time periods of air turbulence and gusts are usually limited (under a minute), the effect of such extreme conditions on commercial aircraft climb and descent can extend to two minutes or more making them bumpy and unstable [87]. For the current investigation, the simulations for the climb and descent legs under aircraft extreme operating conditions were run for the same time span of the steady level flight simulations (350 s), but with the new acceleration components implemented in the numerical solver ANSYS Fluent.

6.2.2 Effect on Airflow Patterns and Circulation in the Cabin under Extreme Operating Conditions

The acceleration-induced body forces on the aircraft directly affect the ventilation airflow patterns inside the cabin. Such patterns can be quantified using airflow velocity fields, airflow boundary layer separation from the walls (boundary layer thickness), and airflow circulation in the cabin. Figure 6.4 shows the airflow velocity vector field near the wall on a lateral plane at the middle of the cabin during the steady level flight leg, and the climb and descent legs under aircraft extreme operating conditions.

Mean airflow velocity magnitudes in all directions inside the cabin were in general greater during the climb and descent legs under aircraft extreme operating conditions than that throughout steady level flight. The monitored airflow velocity magnitudes for the simulated flight times increased anywhere between 1% and 45% during climb leg, and between 6%

and 42% during descent leg under aircraft extreme operating conditions with respect to the steady level flight air velocity magnitudes. On the other hand, the air velocity components in three dimensions (V_x, V_y, and V_z) exhibited different values of increase and decrease between the climb leg under aircraft extreme operating conditions and the steady flight leg, and the descent leg under aircraft extreme operating conditions and the steady flight leg, with no fixed trend.

The increase in airflow velocity magnitudes throughout the climb and descent legs under aircraft extreme operating conditions changed the airflow patterns in the cabin to some degree. The first form of this change is the increased air boundary layer thickness adjacent to the cabin walls due to the tendency of the air to separate earlier from the walls (or to have earlier seperation points on the walls) as it moves downward during the climb and descent under aircraft extreme operating conditions. In other words, the increased downward airflow velocities (0.9 m s^{-1} for the climb and 0.8 m s^{-1} for the descent legs under aircraft extreme operating conditions compared to 0.65 m s^{-1} during the steady level flight) led to reduced airflow attachment to the cabin walls under the no-slip boundary condition applied at them. Consequently, the strongest downward airflow separation (thickest airflow boundary layer) is noticed during the climb leg under aircraft extreme operating conditions exhibiting the highest downward airflow velocity.

The increased airflow velocities and boundary layer separation during the climb and descent legs under aircraft extreme operating conditions led to another effect on the airflow patterns represented by the alteration of the airflow circulation in the cabin. For circulating flows, such as the highly turbulent airflow in the cabin space, circulation (Γ) is defined as the line integral around a closed curve of the velocity field [3],

$$\Gamma = \oint_{\partial s} \vec{U}.d\vec{l}. \tag{6.2}$$

Figure 6.5 shows examples of arbitrary airflow circulation paths on the $x-y$ plane set at the middle of the cabin. Due to cabin symmetry along the longitudinal aircraft axis, these circulation paths are considered to represent the tendency of airflow to circulate throughout the cabin.

From the figure, it can be clearly seen that the airflow circulation can be considered on the full planes, such as $x-y$, $x-z$, and $z-y$ planes ($x-z$ and $z-y$ planes are not shown in the figure but correspond to circulations Γ_y and Γ_x, respectively) and also at the four quadrant corners of each plane, namely the upper-left, upper-right, lower-left, and

lower-right corners. This was made possible by calculating the average airflow velocities on separate line segments located at the top, bottom, right, left, and the center (horizontally and vertically) of each of the mentioned planes. Afterwards, the difference in magnitude between each pair of those velocities (ΔV_x, ΔV_y, ΔV_z), the distances between each two parallel lines on which they were calculated (Δx, Δy, Δz), and the surface area of the plane on which the circulation is quantified, are used to yield an approximate circulation on each plane as follows,

$$\Gamma_x = \left(\frac{\Delta V_z}{\Delta y} - \frac{\Delta V_y}{\Delta z} \right) \Delta y \Delta z, \tag{6.3}$$

$$\Gamma_y = \left(\frac{\Delta V_x}{\Delta z} - \frac{\Delta V_z}{\Delta x} \right) \Delta x \Delta z, \tag{6.4}$$

$$\Gamma_z = \left(\frac{\Delta V_y}{\Delta x} - \frac{\Delta V_x}{\Delta y} \right) \Delta x \Delta y. \tag{6.5}$$

Table 6.2 presents the calculated circulation on the full planes and the four quadrant corners of each plane during the steady level flight leg, in addition to the climb and descent legs under aircraft extreme operating conditions. Also, the percentage changes of those values when each of the climb and descent legs under aircraft extreme operating conditions is compared to the steady level flight case are shown.

Studying Table 6.2, it can be noticed that the circulation on the full planes, in the three directions, and their four quadrant corners exhibits both increases and decreases during the climb and descent legs under aircraft extreme operating conditions, with respect to the steady level flight case, with increases occurring more frequently. However, those increases are not exclusive to one flight leg and occur almost equally between the climb and descent legs under aircraft extreme operating conditions.

The increases in circulation that are majorly observed are mainly attributed to the increase in airflow velocity magnitudes everywhere in the cabin space when the steady level flight leg is either changed to the climb or descent legs under aircraft extreme operating conditions. This is because the increase in airflow velocity magnitudes leads to increasing the turbulent kinetic energy (TKE) in the cabin, which in turn results in stronger airflow vortex shedding and circulation.

One unique characteristic of circulation is that the change in the direction of rotation can be shown between steady level flight and climb leg under aircraft extreme operating

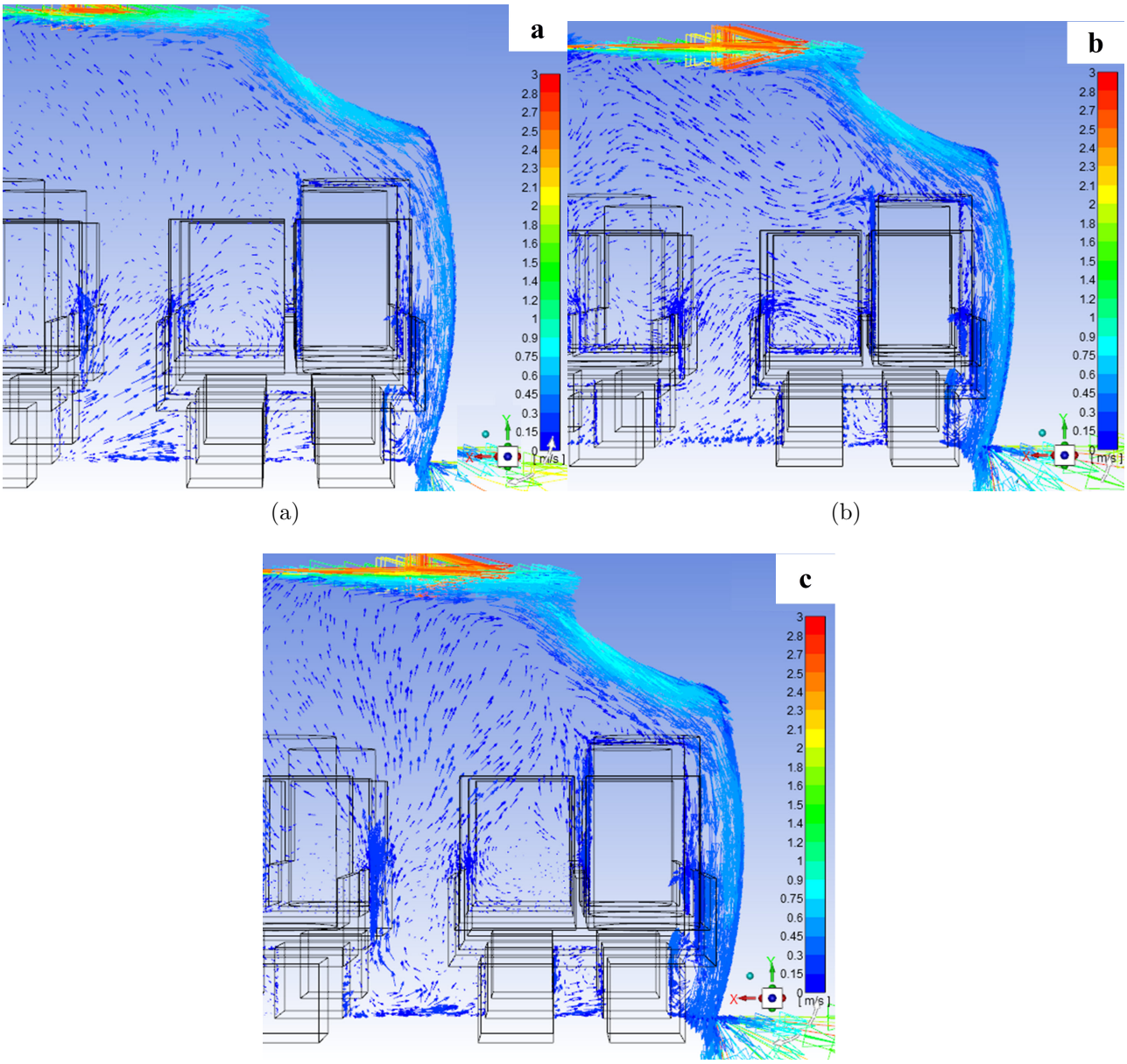

(a) (b)

(c)

Figure 6.4: Airflow velocity vectors near the wall; (a) during steady level flight, (b) during climb leg under aircraft extreme operating conditions, and (c) during descent leg under aircraft extreme operating conditions.

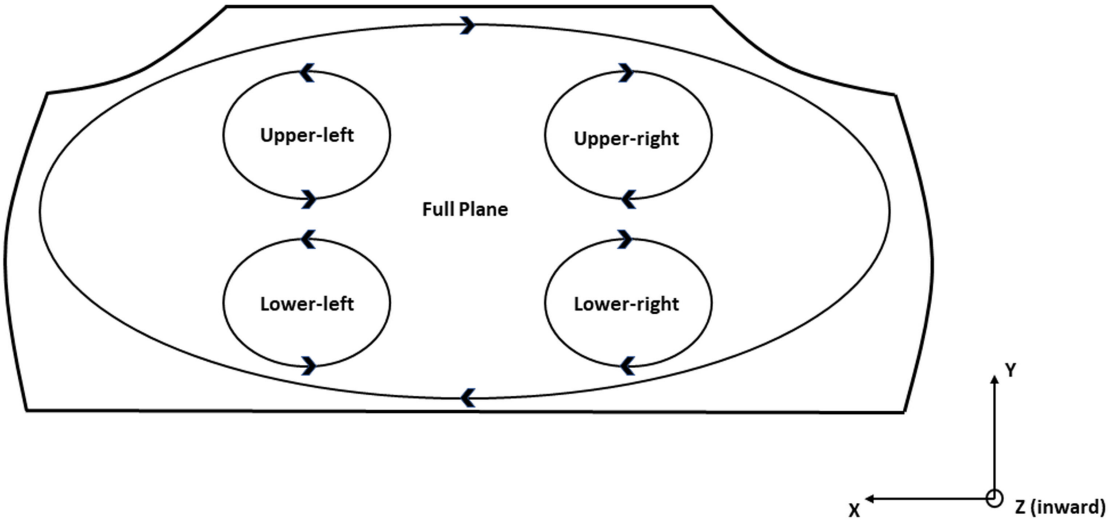

Figure 6.5: Example of the followed notation for estimating the airflow circulation on the full $x-y$ plane (Γ_z) and its four quadrant corners.

conditions, and steady level flight and descent leg under aircraft extreme operating conditions, in addition to the increase or decrease in the circulation strength (magnitude). This is exhibited by a change in the sign of the circulation from positive (clockwise direction) to negative (counter-clockwise direction), and vice versa, following the right-hand rule. Those cases are also clearly demonstrated in Table 6.2 tagged by the footnote (d) to show that a change in the direction of airflow rotation occurs whether the circulation magnitude increases or decreases.

The greatest increase in circulation, taking the steady level flight case as a reference, is seen on the upper-right corner during the descent under aircraft extreme operating conditions on the $x-z$ plane (Γ_y) with around 498% of increase. This is followed by the lower-left corner of both the $y-z$ and $x-z$ planes during the climb leg under aircraft extreme operating conditions with a 249.2% and a 243.9% increase, respectively.

One may also notice that on the full plane, and in every direction, the circulation strength during the climb and descent legs under aircraft extreme operating conditions simultaneously increase or decrease from the steady flight case, even if with different percentages, however, this is not a common trend on the four quadrant corners.

Another interesting observation is that the circulation on the $x-y$ plane (Γ_z) only exhibits a decrease during both the climb and descent legs under aircraft extreme operating conditions on the full plane, while on the four quadrant corners, it always shows an increase during those two legs. The decrease in circulation on the full $x-y$ plane during both the climb and descent legs under aircraft extreme operating conditions when changed from the steady level flight leg can be attributed to the nearly symmetrical airflow field on this plane on the two cabin sides. With the downward airflow velocities increasing on each side of the cabin during the climb and descent legs under aircraft extreme operating conditions, this symmetry in airflow field between the two sides leads to stronger interactions among the airflow currents coming from one side with the currents coming from the other side. This creates a resistance to the airflow circulation and results in lower overall circulation magnitude on the $x-y$ plane when compared to the standard steady level flight scenario.

Table 6.2: Airflow circulation values and changes between steady level flight, climb leg under aircraft extreme operating conditions, and descent leg under aircraft extreme operating conditions.

Plane/side corner	Flight leg	Circulation[a,b]			Change in circulation[c] (%)		
		Γ_x	Γ_y	Γ_z	Γ_x	Γ_y	Γ_z
Full plane	Steady flight	-0.0215	-0.0959	0.0419	—	—	—
	Extrm Climb	-0.0555	-0.1554	0.0148	**158.1***	62.05	-64.64
	Extrm Descent	0.0690	-0.2854	0.0392	**221.1[d,*]**	**197.7 ***	-6.45
Lower-right	Steady flight	0.0392	-0.0869	0.3846	—	—	—
	Extrm Climb	-0.0469	-0.0572	0.4522	19.64[d]	-34.13	17.59
	Extrm Descent	0.1024	-0.1022	0.4174	**161.3***	17.71	8.53
Lower-left	Steady flight	0.0326	-0.0254	-0.3260	—	—	—
	Extrm Climb	0.1137	-0.0872	-0.4275	**249.2***	**243.9***	31.12
	Extrm Descent	-0.0294	-0.0076	-0.3575	-9.83[d]	-70.06	9.64
Upper-right	Steady flight	-0.0433	-0.0226	0.3283	—	—	—
	Extrm Climb	-0.1414	0.0095	0.4118	**226.6***	-57.81[d]	25.42
	Extrm Descent	0.0639	-0.1351	0.3567	47.49[d]	**498.3***	8.64
Upper-left	Steady flight	-0.0499	0.0389	-0.3449	—	—	—
	Extrm Climb	0.0192	-0.0205	-0.4216	-61.66[d]	-47.39[d]	22.25
	Extrm Descent	-0.0679	-0.0405	-0.3774	35.94	3.99[d]	9.41

a. The unit for circulation is $m^2\ s^{-1}$.

b. (+) is in clockwise direction and (-) is in counterclockwise direction following the right-hand rule.

c. (+) indicates an increase and (-) a decrease from steady flight.

d. Accompanied with a change in the direction of rotation.

***** Values in bold face represent significant change percentages (>100%).

6.2.3 Effect on Contaminant Dispersion behavior in the Cabin under Extreme Operating Conditions

The change in airflow patterns and circulation under the influence of body forces subsequently affects the cough-released airborne contaminant dispersion behavior in the aircraft cabin and alters it from the baseline steady level flight leg. This is confirmed by multiple studies in the literature that investigated the effect of ventilation airflow patterns and structures on the airborne contaminant distribution behavior in aircraft cabins [53, 54, 92].

Li et al. [54] found that the ventilation airflow vortex structure has an important effect on the CO_2 airborne contaminant surrogate distributions in a model for an aircraft cabin mock-up. They noticed that when the contaminants were released from a location dominated by strong vortex shedding, they were more likely to be trapped in the vortex, resulting in 62% higher average concentration and 14% longer residual time in the cabin than that when the release source was in other locations. Similarly, Li et al. [53] concluded that the changing and complex ventilation airflow velocity field in the narrow cabin space has a significant effect on the contaminant distribution behavior in the cabin. Moreover, Wang et al. [92] noticed that the CO_2 airborne contaminant surrogate distribution behavior and residual time in the cabin space was affected not only by the airflow velocity magnitude, but also by the local airflow patterns such as jet and circulation.

Figures 6.6, 6.7, and 6.8 depict the SF_6 contaminant surrogate concentration contours in the cabin at different simulation times during the steady level flight leg, the climb leg under aircraft extreme operating conditions, and descent leg under aircraft extreme operating conditions, respectively.

Looking at Figure 6.6, one can notice that the SF_6 dispersion during the steady level flight leg starts from the central back area of the cabin, where the cougher is located, and then, the contaminant tends to disperse laterally to the two sides with a high concentration region preserved at the center. Afterwards, and specifically after approximately 200 s has passed since cough was released, the dispersion pattern changes from lateral to longitudinal where the SF_6 spreads to the front rows. This steady level flight dispersion scheme is clearly motivated only by the traditional airflow patterns in the cabin with no existent body forces (other than gravity) on the aircraft that can influence the contaminant dispersion, which kept it at the center of the cabin for most of the simulation time.

This central intensification behavior of the contaminant during the steady level flight leg is confirmed by the airflow circulation magnitudes, which are mainly equal among the

four quadrant sides on each plane in the cabin (Γ_x, Γ_y, and Γ_z) as shown in Table 6.2 in the previous subsection. This leads to a balance in the airflow circulation strength among the circulation regions on each plane, which tends to keep the highest SF_6 concentration at the center of the cabin. For example, on the $x-y$ plane (corresponding to Γ_z), the circulation magnitudes are almost constant among the lower-right, lower-left, upper-right, and upper-left quadrants of the plane during the steady level flight leg at 0.3846, 0.3260, 0.3283, and 0.3449 m^2 s^{-1}, respectively.

On the other hand, the body forces during the climb leg under aircraft extreme operating conditions influence the SF_6 to mainly disperse to the back of the cabin as seen in Figure 6.7. SF_6 moves to the back in a longitudinal pattern just after being released, then it disperses laterally to the sides while being restricted to the back rows. Later, a minor longitudinal dispersion pattern drives some of the released contaminant to the front rows starting from left to right while keeping the majority of the contaminant at the back-left corner where the highest risk of exposure exists.

To explain the contaminant intensification pattern at the back section of the cabin, especially on the left side (looking to the front of the cabin), during the climb leg under aircraft extreme operating conditions, the airflow circulation magnitudes during this leg are analyzed. Looking at table 6.2, one can notice that the airflow circulation is varied in strength among the four quadrants of the $y-z$ and $x-z$ planes (corresponding to Γ_x and Γ_y), while it was almost equal among the four quadrants on the $x-y$ plane during the climb leg under aircraft extreme operating conditions. This is because on each of the first two planes, less airflow circulation strengths are noticed at the quadrant corner closer to the back of the cabin than the other three quadrants (i.e. the upper-left corner on the $y-z$ plane and the upper-right corner on the $x-z$ plane). This motivates the contaminant to transport from the quadrant corners with high airflow circulation strengths (high dispersion resistance) to the corners with low circulation strengths (low dispersion resistance) on the two planes and eventually residing at the back of the cabin on the left side. However, on the $x-y$ plane, the absence of such variances in the circulation magnitudes is because of the lateral nature of the plane set at the middle of the cabin away from the contaminant intensification pattern at the back.

In a similar manner to the climb leg under aircraft extreme operating conditions, the body forces during the descent leg under aircraft extreme operating conditions were also effective on the SF_6 dispersion pattern in the cabin as seen in Figure 6.8. The contaminant is pushed to the back of the cabin for short time due to its own inertia before the body forces

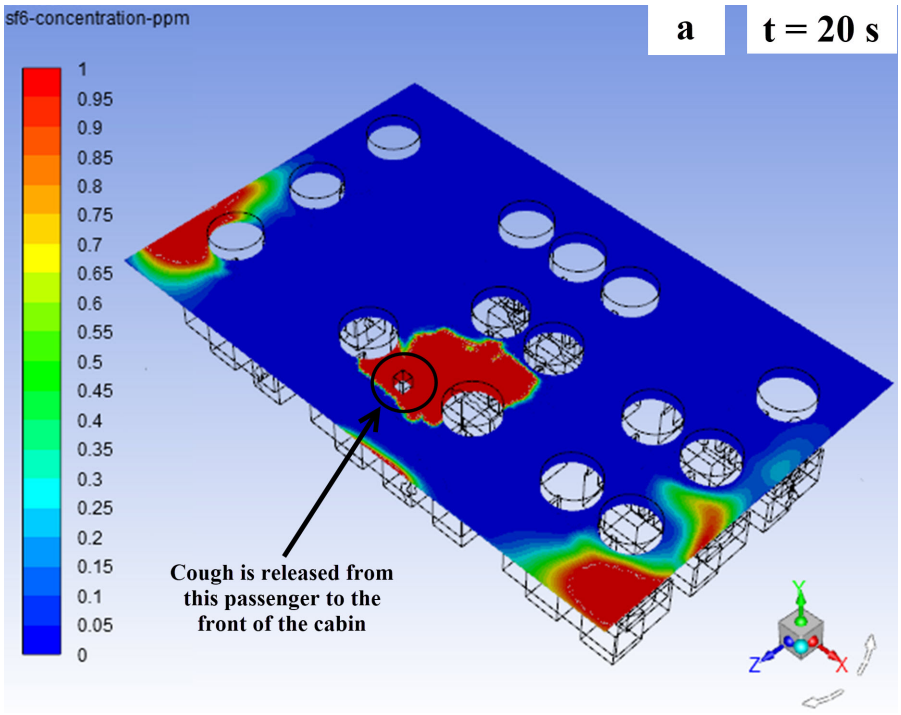
sf6-concentration-ppm
1
0.95
0.9
0.85
0.8
0.75
0.7
0.65
0.6
0.55
0.5
0.45
0.4
0.35
0.3
0.25
0.2
0.15
0.1
0.05
0
a
t = 20 s
Cough is released from this passenger to the front of the cabin
Y
Z
X

(a)

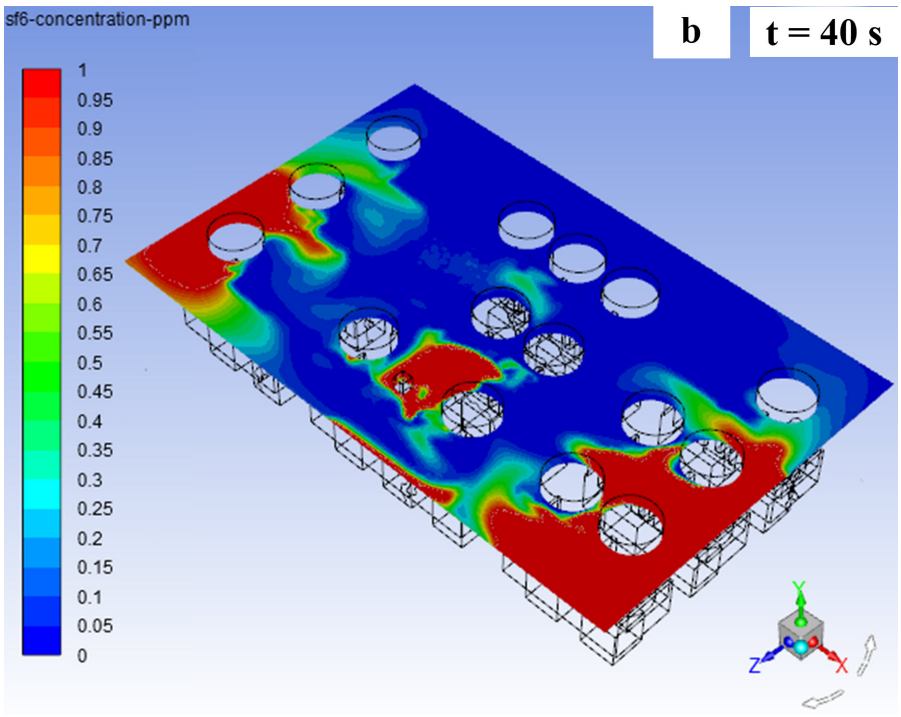
sf6-concentration-ppm
1
0.95
0.9
0.85
0.8
0.75
0.7
0.65
0.6
0.55
0.5
0.45
0.4
0.35
0.3
0.25
0.2
0.15
0.1
0.05
0
b
t = 40 s
Y
Z
X

(b)

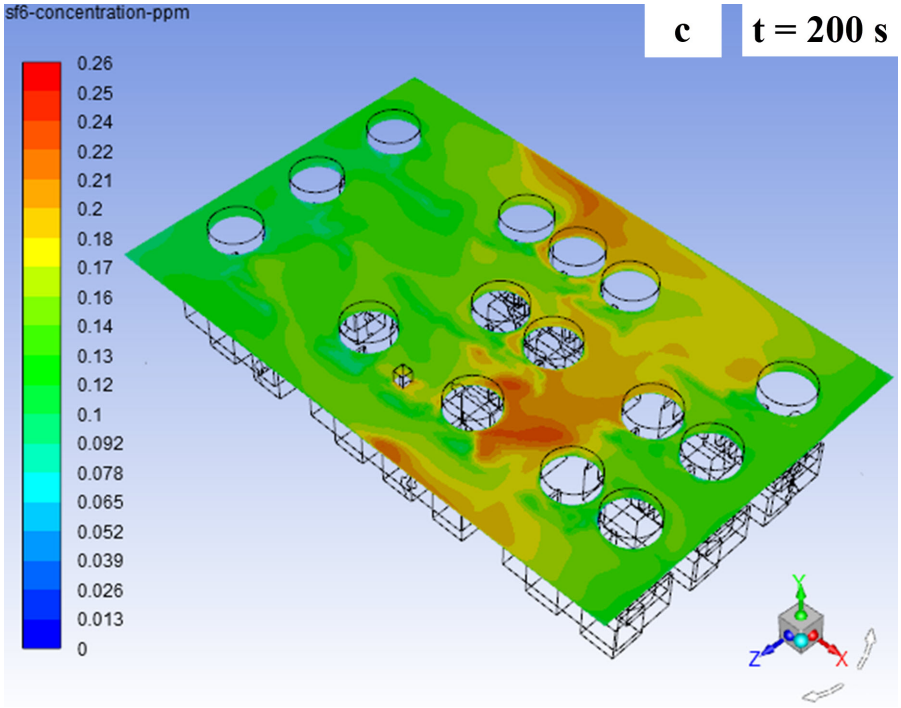

(c)

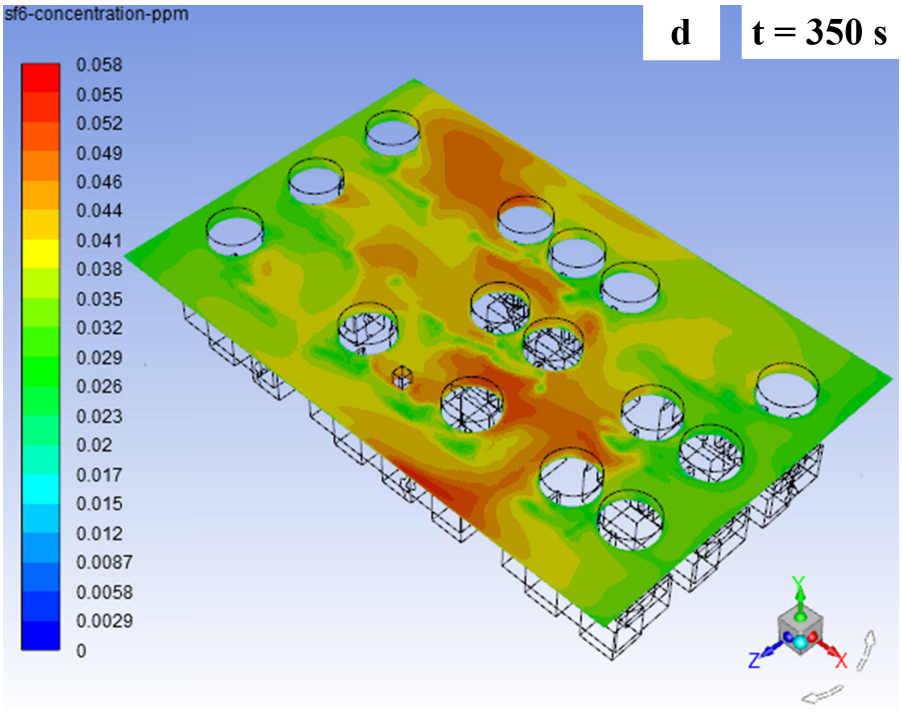

(d)

Figure 6.6: SF_6 concentration (ppm) contour plots at breathing level during steady level flight; (a) at t = 20 s, (b) at t = 40 s, (c) at t = 200 s, and (d) at t = 350 s after cough release.

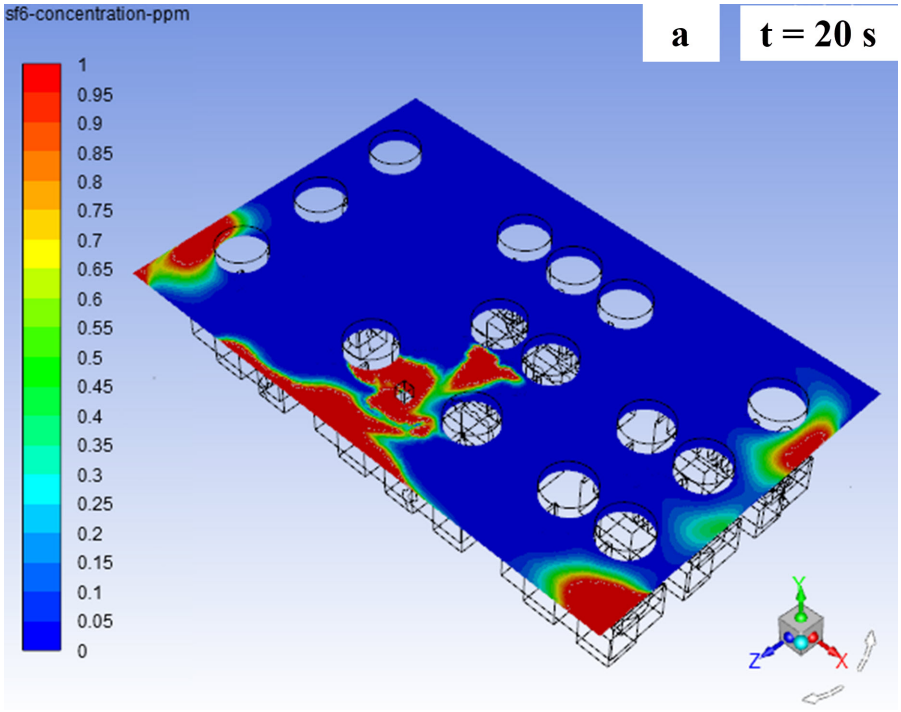
sf6-concentration-ppm
1
0.95
0.9
0.85
0.8
0.75
0.7
0.65
0.6
0.55
0.5
0.45
0.4
0.35
0.3
0.25
0.2
0.15
0.1
0.05
0
a
t = 20 s
Y
Z
X

(a)

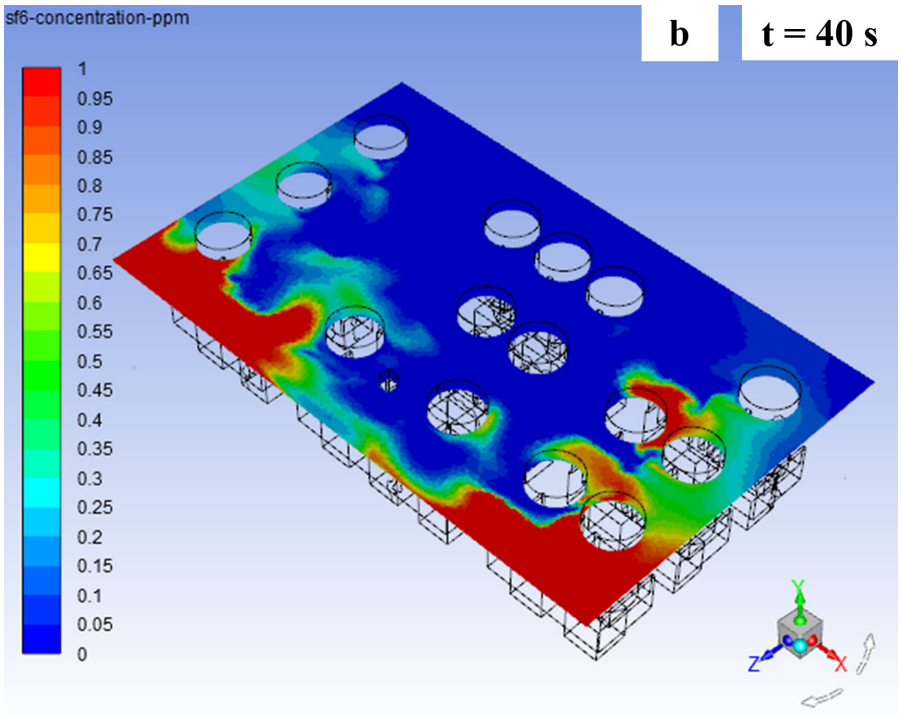
sf6-concentration-ppm
1
0.95
0.9
0.85
0.8
0.75
0.7
0.65
0.6
0.55
0.5
0.45
0.4
0.35
0.3
0.25
0.2
0.15
0.1
0.05
0
b
t = 40 s
Y
Z
X

(b)

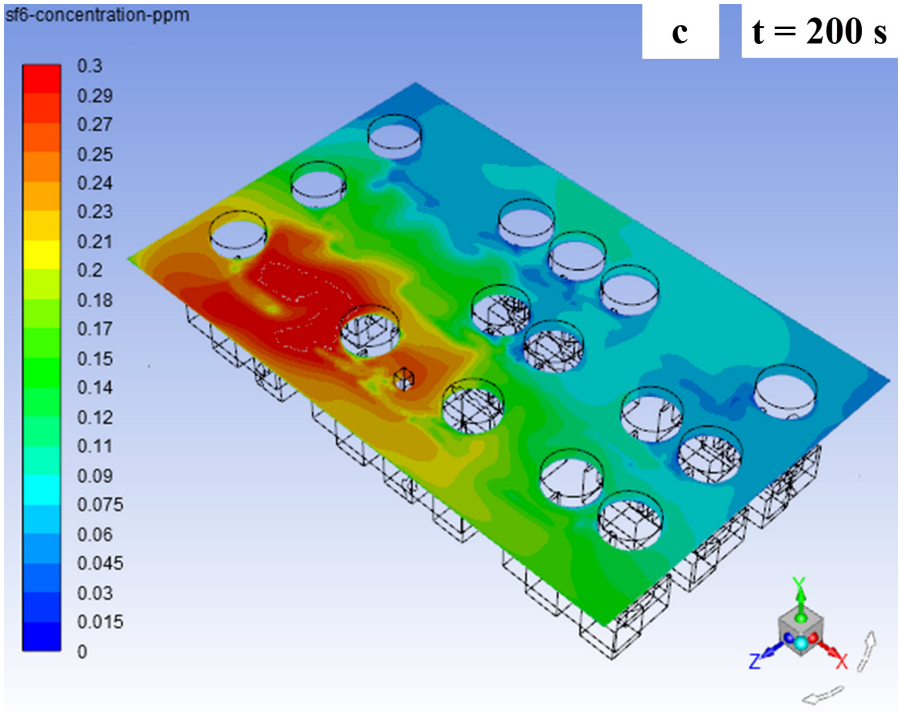

(c)

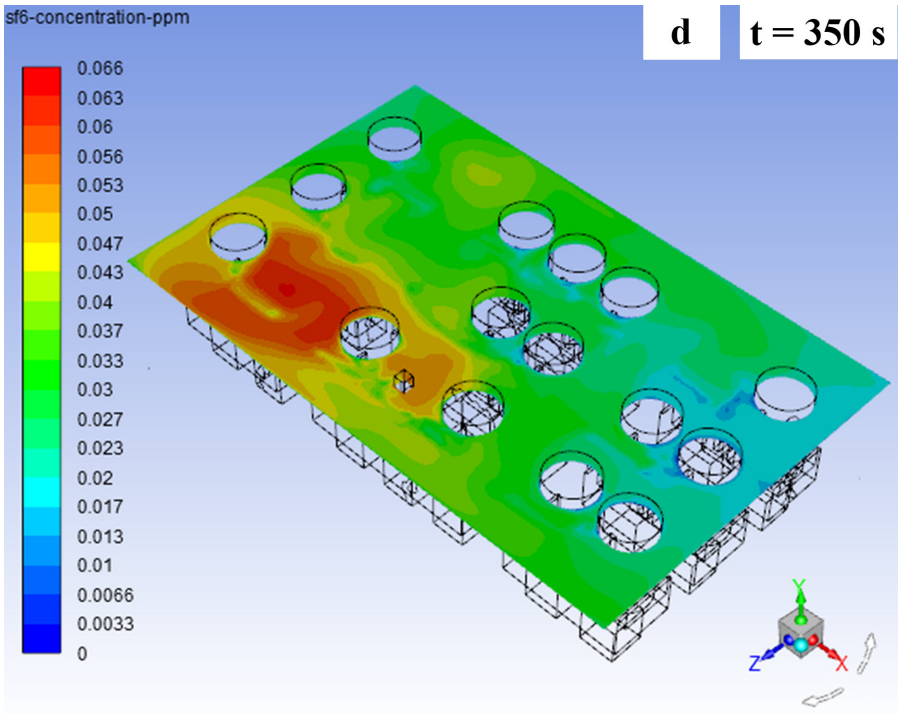

(d)

Figure 6.7: SF_6 concentration (ppm) contour plots at breathing level during climb leg under aircraft extreme operating conditions; (a) at t = 20 s, (b) at t = 40 s, (c) at t = 200 s, and (d) at t = 350 s after cough release.

during the descent leg under aircraft extreme operating conditions make it disperse to the front rows while restricting its lateral movement to the left side of the cabin. Later, SF_6 disperses slightly to the right side of the cabin while concentrating mainly at the left side of the front row (Note that the cabin occupancy is not symmetric from left to right).

Generally, the body forces due to aircraft acceleration during the climb and descent legs under aircraft extreme operating conditions appear to influence the dispersion pattern of the SF_6 contaminant surrogate in the cabin. The contaminant is forced to disperse in directions of the body force vector and to settle either at the back (climb) or front (descent). This behavior is ultimately influenced by the airflow patterns in the cabin throughout the different flight legs.

For the two set monitoring locations at seats A7 and C7, Figure 6.9 shows a comparison of the calculated concentration time series of SF_6 during steady level flight, climb, and descent.

It can be clearly noticed from Figure 6.9 that the tracer gas concentration is significantly higher (up to 150-300% more) during the climb leg under aircraft extreme operating conditions than the steady level flight case for most of the simulation time, especially at seat A7. Consequently, the level of exposure of passengers sitting at any of the two seats to the contaminant, which can be interpreted from the area under the curves, significantly increases throughout the aircraft climb time with the same percentage of the concentration. This poses greater risks on the health and well-being of most passengers in the cabin upon exposure to hazardous gaseous substances, in-cabin contaminants, or some infectious particulates during the aircraft climb leg under an extreme condition, such as gusts, that can impact commercial aircraft for considerable time periods especially for long-haul and transoceanic flights [87].

On the other hand, the SF_6 concentration time series during the descent leg under aircraft extreme operating conditions does not noticeably differ from that for the steady level flight leg, possibly due to the limited aircraft acceleration components during the descent leg generating limited acceleration-induced body forces on the aircraft. This indicates that the level of passengers' exposure to contaminant during the descent leg under aircraft extreme operating conditions is very close to that during the steady level flight leg at the breathing height.

To put the comparisons between climb and descent legs under aircraft extreme operating conditions, and steady level flight in more quantitative form, the exposure of passengers over time is calculated using equation 5.2.

Table 6.4 shows the ratio of passenger exposure during each of the climb and descent legs under aircraft extreme operating conditions to that during the steady level flight, and

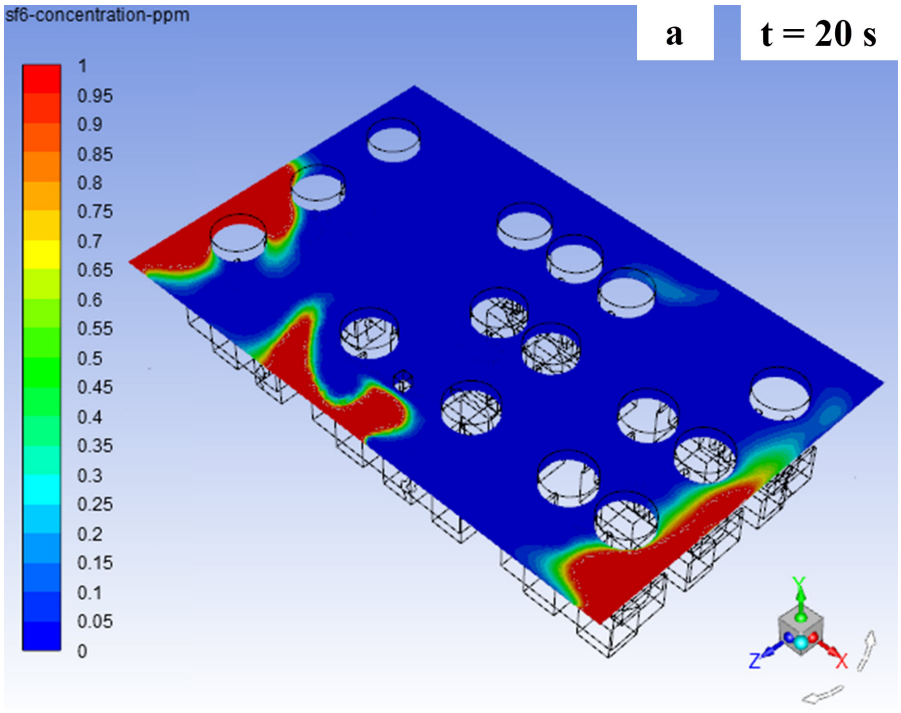
sf6-concentration-ppm
1
0.95
0.9
0.85
0.8
0.75
0.7
0.65
0.6
0.55
0.5
0.45
0.4
0.35
0.3
0.25
0.2
0.15
0.1
0.05
0
a
t = 20 s
Y
Z
X

(a)

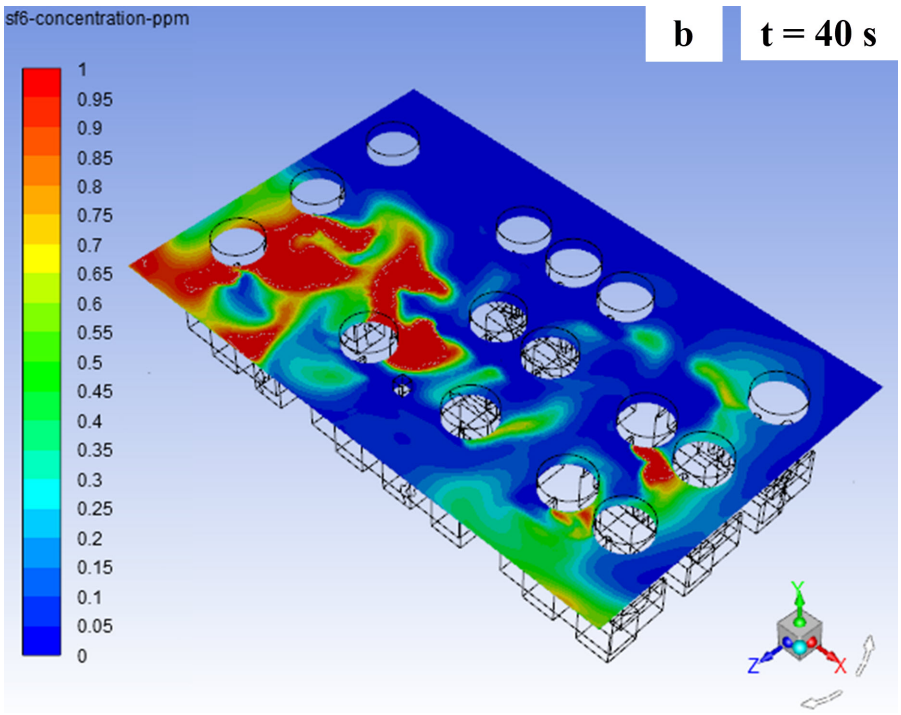
sf6-concentration-ppm
1
0.95
0.9
0.85
0.8
0.75
0.7
0.65
0.6
0.55
0.5
0.45
0.4
0.35
0.3
0.25
0.2
0.15
0.1
0.05
0
b
t = 40 s
Y
Z
X

(b)

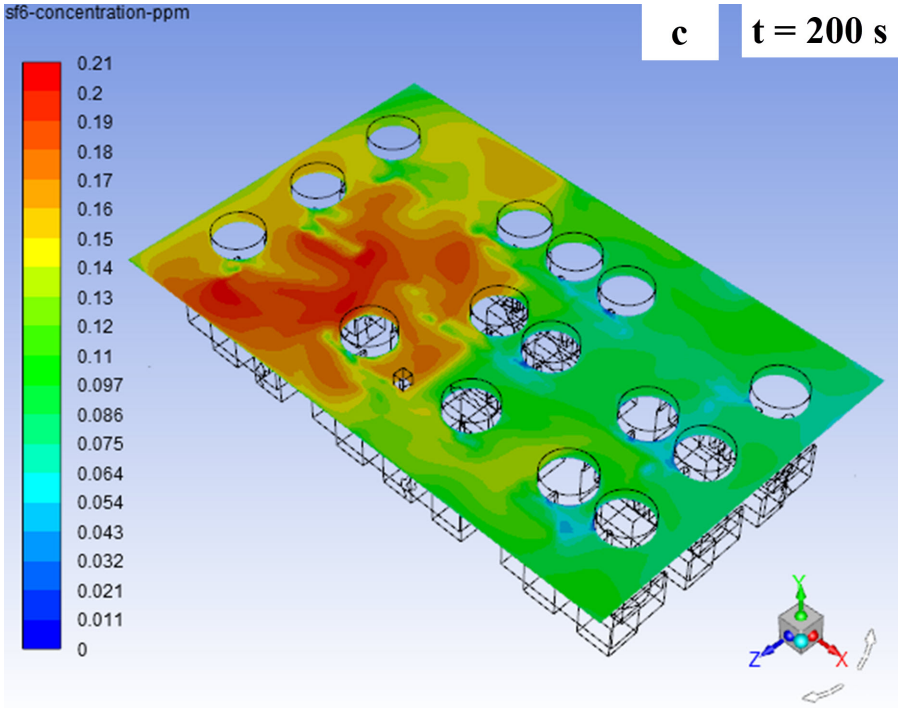

(c)

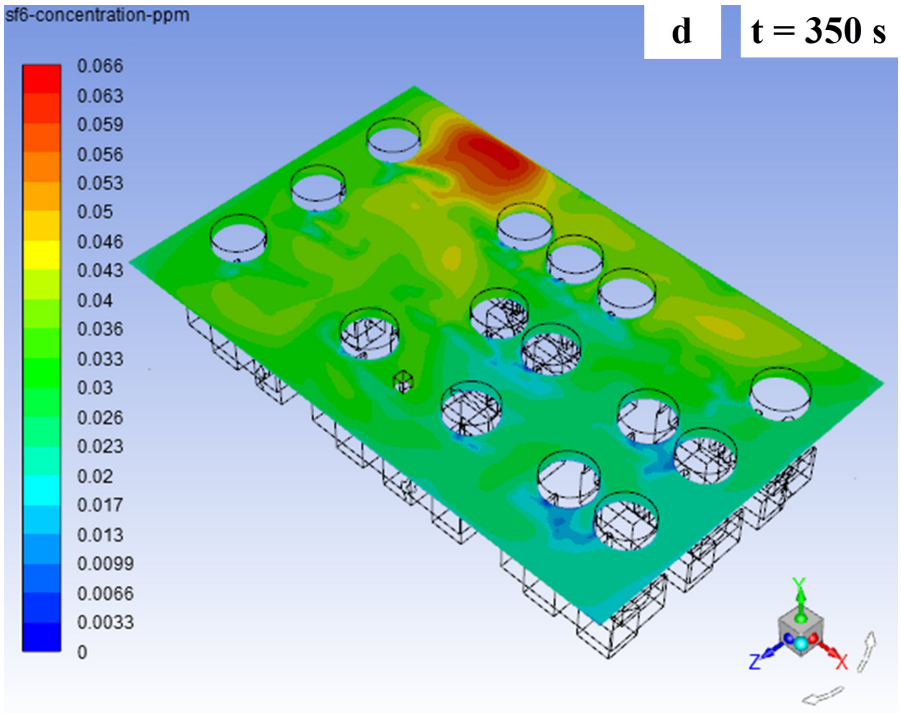

(d)

Figure 6.8: SF_6 concentration (ppm) contour plots at breathing level during descent leg under aircraft extreme operating conditions; (a) at t = 20 s, (b) at t = 40 s, (c) at t = 200 s, and (d) at t = 350 s after cough release.

the ratio of exposure during the climb leg to the descent leg under aircraft extreme operating conditions, as well, at seats A7 and C7.

Looking at Table 6.4, it can be noticed that the passenger exposure is always the highest during the climb leg under aircraft extreme operating conditions when compared to the steady level flight and the descent leg. The most elevated exposure ratio was 3 to 1, calculated between climb and descent at seat C7. At the same seat, the passenger exposure during the descent leg under aircraft extreme operating conditions was slightly less than the steady level flight with a ratio of 0.9 to 1.

Table 6.4: Ratio of passenger exposure between different flight legs at the two monitoring locations.

Flight legs	Passenger exposure ratio	
	Seat A7	Seat C7
Climb (Extreme) : Steady Level Flight	2.4 : 1	2.8 : 1
Descent (Extreme) : Steady Level Flight	1.3 : 1	0.9 : 1
Climb (Extreme) : Descent (Extreme)	1.9 : 1	3.0 : 1

At seat A7, however, the climb leg under aircraft extreme operating conditions to steady flight exposure ratio was higher than the ratio between both the climb and descent legs under aircraft extreme operating conditions. Additionally, the exposure during the descent leg under aircraft extreme operating conditions was very close to that during the steady level flight with a ratio of 1.3 to 1.

One factor that may have contributed to the considerable difference in the SF_6 concentration time series (or exposure) between the climb leg and descent leg under aircraft extreme operating conditions is the difference between climb and descent rate of velocity change and the corresponding accelerations under the extreme condition of gusts. The climb speed for most modern jet-powered passenger aircraft can reach up to 600 km hr^{-1} (324 knots) or more, while the full-powered descent rate is limited to around 250 km hr^{-1} (135 knots) only to ensure passengers' comfort. This large difference in aircraft speed between the two mission legs yields dissimilar aircraft accelerations, and therefore, distinct effects of the generated body forces on the contaminants dispersion rates and flow patterns inside the cabin.

Another factor in play is the difference between the climb and the descent flight path

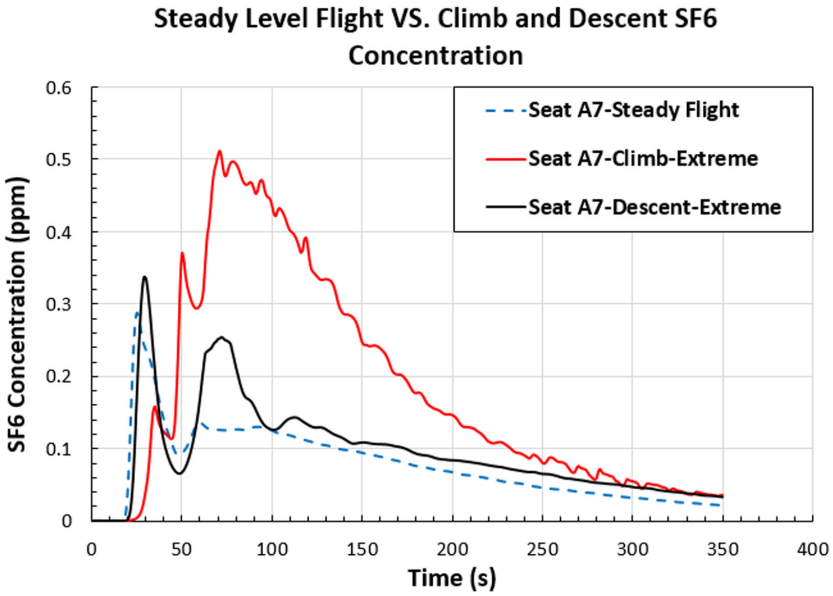

(a)

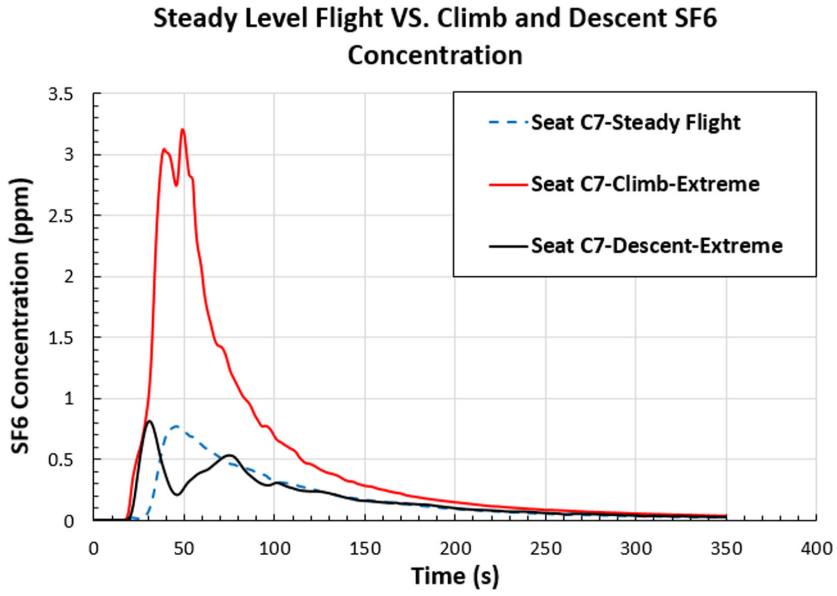

(b)

Figure 6.9: Comparison of the predicted SF_6 concentration time series among steady level flight, climb and descent legs under aircraft extreme operating conditions; (a) at seat A7, and (b) at seat C7.

(inclination) angles. During the take-off and climb legs, most jet-powered passenger aircraft adopt an inclination angle from 15° to 20°, such an angle is much steeper than the small descent angle restricted mostly to 3° to perform comfortable descents. As much as the rise in aircraft speed, the increase of the climb angle over the descent angle can also contribute in enhancing the dispersion rate of contaminants and changing their distribution contours within the cabin. This is because changing the flight path angles significantly alters the values of the aircraft acceleration components on the vertical and horizontal directions, and therefore, the acceleration-induced body force components acting on the aircraft in motion, the ventilation airflow patterns, and the contaminant dispersion behavior inside the cabin in each of those two directions. Such effects were fully considered in the present model.

6.3 Conclusions

In Chapter 6, the acceleration-induced body forces on passenger aircraft during the climb and descent legs under aircraft normal and extreme operating conditions are quantified and studied.

For aircraft normal operating conditions, the method used for calculating the passenger aircraft acceleration components during the climb and descent legs under those conditions is detailed. Additionally, the results concerned with the effect of those accelerations on contaminant concentration and dispersion behavior in the aircraft cabin are discussed. Actual commercial passenger aircraft traffic satellite data extracted from the U.S. National Oceanic and Atmospheric Administration (NOAA)'s Aircraft Meteorological Data Relay (AMDAR) satellite system were utilized to quantify the acceleration components of passenger aircraft for a hundred different flights using a second order curve-fitting technique.

Implementing the acceleration components in numerical simulations for aircraft climb and descent under aircraft normal operating conditions, it was found that the predicted contaminant (SF_6) concentration time series did not majorly differ from that for the steady level flight case (in which only the gravitational acceleration is in effect on the aircraft). For the climb leg under aircraft normal operating conditions, the SF_6 concentration time series was marginally less that during the steady level flight case at seat A7, while at seat C7 in the back row, the peak SF_6 concentration was about 50% less than that for the steady level flight case. Conversely, for the descent leg, and at seat A7, the SF_6 concentration was less than that for the steady level flight case for most of the simulation time. At seat C7, however, the SF_6 concentration time series was very close to that for the steady level flight

scenario. Generally, the passenger aircraft acceleration components during the climb and descent under normal operating conditions led to different contaminant dispersion behavior in the cabin between each other affected by the acceleration-induced body forces. However, none of the two cases produced contaminant concentrations that are considerably dissimilar to the the baseline steady level flight cases. This is based on the passenger exposure ratios between normal climb and steady level flight which were 0.92 to 1 at seat A7 and 0.77 to 1 at seat C7. Whereas, they were equal to 0.75 to 1 at seat A7 and 0.99 to 1 at seat C7 between normal descent and steady level flight. Consequently, it can be concluded that the acceleration-induced body forces have limited but existent effect on the contaminant dispersion behavior in passenger aircraft cabins during the climb and descent legs under the normal operating conditions.

On the other hand, for aircraft extreme operating conditions, the aircraft acceleration components have been chosen to simulate a condition of operating in gusty surroundings. The results concerned with the effect of acceleration-induced body forces on ventilation airflow patterns and contaminant dispersion behavior in the simulated aircraft cabin model during different aircraft mission legs are presented and discussed. The steady level (cruise) flight leg, which takes most of the flight time is taken as the reference case, to which the contaminant concentration and airflow changes during the climb and descent flight legs under aircraft extreme operating conditions are compared.

Airflow velocity magnitudes, increased everywhere in the simulated cabin during the climb leg under aircraft extreme operating conditions (between 1% and 45% increase) and the descent leg under aircraft extreme operating conditions (between 6% and 42% increase) compared to the steady level flight case. But, this was not the case for the airflow velocity components (V_x, V_y, and V_z) which showed different levels of increase and decrease with no fixed trend.

The change in airflow velocities had a significant effect on the airflow patterns and circulation in the cabin. Downward airflow coming from supply slots was less attached to the cabin walls during the climb and descent legs under aircraft extreme operating conditions than through the steady flight time. Additionally, airflow circulation strength in every direction inside the cabin, either on the full plane or its four quadrant corners, exhibits both increases and decreases during the climb and descent legs under aircraft extreme operating conditions with respect to the steady level flight case with increases occurring more frequently.

As a result of the accleration-induced body forces' influence on the airflow patterns and circulation in the cabin, it was noticed that the body forces during the climb and descent

legs under aircraft extreme operating conditions also affect the dispersion patterns of the contaminant surrogate in the cabin. This was evident in the concentration time series and concentration contour plots for the contaminant surrogate (SF_6). The contaminant was made to disperse in directions of the body force vector and to eventually settle either at the back of the cabin during climb, or the front during descent until this contaminant is cleared out of the cabin by the ventilation system. This behavior is mainly influenced by the airflow patterns in the cabin throughout the different flight legs. It was also remarked that the concentration of the contaminant at the two set monitoring locations, and therefore the passengers' exposure, increased substantially during the climb leg under aircraft extreme operating conditions from the steady level flight with ratios of 2.4 to 1 and 2.8 to 1 at seats A7 and C7, respectively. However, this was not the case during the descent leg under aircraft extreme operating conditions, throughout which the SF_6 concentration did not considerably differ from that during the steady level flight time with exposure ratios limited to 1.3 to 1 at seat A7, and 0.9 to 1 at seat C7.

The findings indicate the potent effect the acceleration-induced body forces have on the airflow patterns and contaminant dispersion behavior inside the cabins of passenger aircraft operating under extreme conditions, such as gusts, which are frequently encountered during flights. This depends on many factors, such as weather conditions, flight duration, and flight course. The findings call for more research attention to this topic to unveil some ventilation and/or ergonomic design remedies to the negative effects this may have on the health of occupants in commercial aircraft.

Chapter 7

Airflow Design and Source Control Strategies for Reducing Airborne Contaminant Exposure in the Aircraft Cabin During the Climb Leg under Extreme Operating Conditions

In this chapter, the same airflow design and source control strategies which were investigated as mitigation or reduction means for the cough-released contaminant exposure in passenger aircraft cabin during the steady level flight leg in Chapter 5 are used again to research their capability of limiting the increased passenger exposure during the climb leg under aircraft extreme operating conditions.

The case for the descent leg under aircraft extreme operating conditions was not considered due to the evidence that passenger exposure to the contaminant is not substantially influenced by the body forces on the aircraft during this leg (look at subsection 6.2.3).

The airflow design strategies used are changing airflow supply direction and altering the airflow rate. Moreover, the source control strategies considered are changing the cough direction, varying the cough velocity, and relocating the cougher to other locations in the cabin.

7.1 Airflow Design Strategies

7.1.1 Airflow Direction

For this investigation, the direction of the supply airflow during the climb leg under aircraft extreme operating conditions was changed using the same two-dimensional and three-dimensional approaches as in Chapter 5 by employing angle α alone in 2-D, and angles α and β together in 3-D.

Changing Angle α Only

The change of the supply airflow direction angle α in 2-D during the climb leg under aircraft extreme operating conditions is performed through the three airflow supply angles previously investigated for the steady level flight leg: 20°, 30°, and 60°. The SF_6 concentration time series for the 20° and 30° airflow supply scenarios during climb under aircraft extreme operating conditions versus that for the standard climb under the same extreme conditions (with $\alpha = 0°$) and the steady level flight at seats A7 and C7 are shown in Figure 7.1. For the readability of the figures, the same comparison for the 60° supply case is shown separately in Figure 7.2.

From Figures 7.1 and 7.2 it can be seen that the airflow supplied at 30° had the peak SF_6 concentration, and consequently the exposure of occupants, reduced to almost 50% of the original concentration during climb under aircraft extreme operating conditions at the two monitoring locations. Conversely, the airflow supplied at 20° was not able to provide better air quality conditions at the two monitoring locations, and the exposure of passengers to the contaminant was almost coincident to that for the original climb air supply scenario under the same extreme conditions.

On the other hand, from Figure 7.2, it can be noticed that supplying air at 60° to the cabin produced the worst air quality conditions at the two locations. This is because it lead to very high passenger exposure to SF_6, especially at seat A7, where the exposure was around 400% of the original case.

The SF_6 concentration contours at 350 s after contaminant release in the cabin are shown at the breathing level of the occupants for the 30° and 60° airflow supply cases in Figure 7.3. As can be seen in the two contour plots, and similar to the case under steady level flight condition (Chapter 5), when α is set to 60°, the area covered by the supplied air is very narrow and restricted to the cabin central area around the two rear seat rows. This

leaves most of the seats on the two cabin sides exposed to the contaminant. On the contrary, the airflow supplied at 30° efficiently reached the cabin sides and lead to reduced passenger exposure at most cabin seats. Therefore, with $\alpha = 30°$, the SF_6 contaminant surrogate was uniformly distributed in the cabin space due to the mixing effect induced by the strong airflow circulation during the climb leg under aircraft extreme operating conditions. This leads to uniform contaminant concentration everywhere at the breathing level of the occupants.

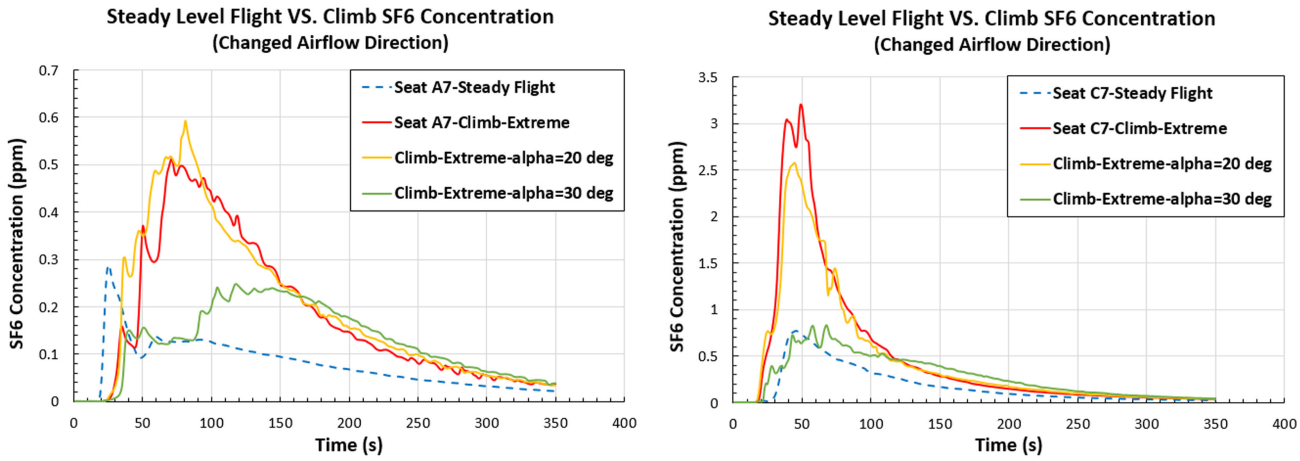

(a) (b)

Figure 7.1: Comparison of the predicted SF_6 concentration time series between the steady level flight leg and climb leg under aircraft extreme operating conditions using the default, 20°, and 30° airflow supply angles during climb; (a) at seat A7, and (b) at seat C7.

Changing Angles α and β Simultaneously

For this air supply angle change approach, angle β is simultaneously changed with angle α in a three-dimensional manner. Different to the steady level flight leg, $\alpha = 30°$ provided the best cabin air quality relative to the other two airflow supply angles in 2-D during the climb leg under aircraft extreme operating conditions. Therefore, $\alpha = 30°$ will be used here with β also chosen to be equal to 30° with supply airflow either directed to the front or to the back of the cabin. Figure 7.4 shows the SF_6 concentration time series at the two monitoring locations using $\beta = 30°$ to the front and to the back.

Looking at Figure 7.4, it can be seen that the $\beta = 30°$ airflow supply to the back of the cabin was able to reduce the time-integrated passenger exposure from the original climb case either at seat A7 or seat C7. More specifically, at seat C7, the exposure was reduced to

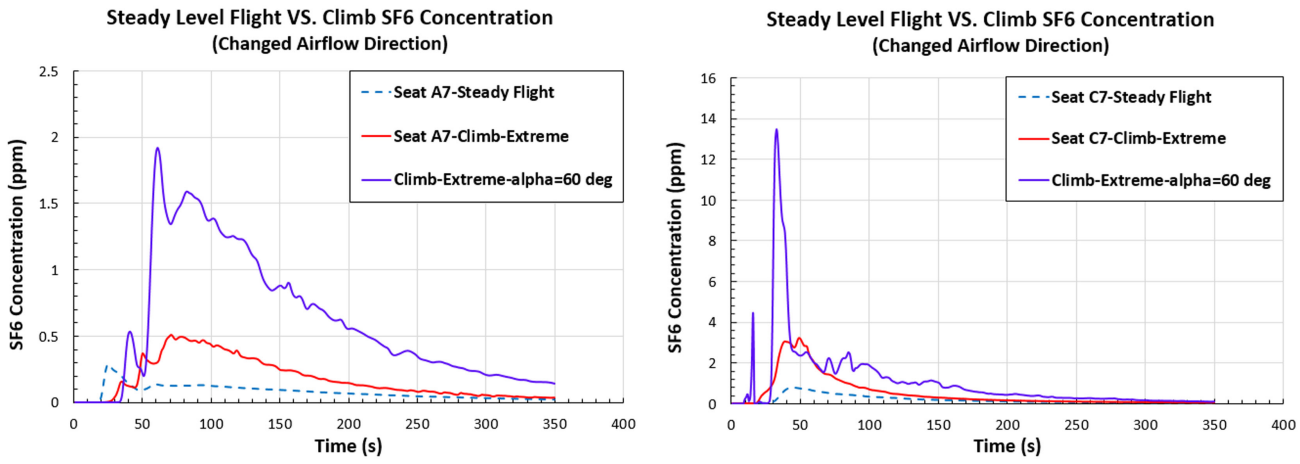

(a) (b)

Figure 7.2: Comparison of the predicted SF_6 concentration time series between the steady level flight leg and climb leg under aircraft extreme operating conditions using the default and 60° airflow supply angles during climb; (a) at seat A7, and (b) at seat C7.

a level close to that for the steady level flight condition. On the other hand, in case of the $\beta = 30°$ airflow supply to the front, the passenger exposure was higher at seat A7 than the original case, but the exposure was almost halved for the same scenario at seat C7. The SF_6 contour plots for the two airflow supply cases at 350 s are compared as shown in Figure 7.5.

As noticed from Figure 7.5, directing airflow to the front of the cabin pushes the contaminant to the back of the cabin at the end of simulation time (at 350 s). Before that, the air moves most of the contaminant to the front rows for a short period of time (70-80 s) after contaminant release in the cabin. Conversely, supplying airflow to the back of the cabin leads to steadily pushing the contaminant to the front of the cabin and providing dilution of it in the cabin air with no dispersion patterns in the back rows. This makes the back-directed airflow able to consistently reduce the overall passenger exposure to the contaminant at most cabin seats.

7.1.2 Airflow Rate

Following the criteria for the airflow rate change in Chapter 5, the three cabin airflow rate change cases: 400 L s^{-1} (100% more airflow), 300 L s^{-1} (50% more airflow), and 100 L s^{-1} (50% less airflow) are investigated as an airflow design strategy to reduce the passenger exposure to the cough-released contaminant from the original case (200 L s^{-1} airflow rate). Figure 7.6

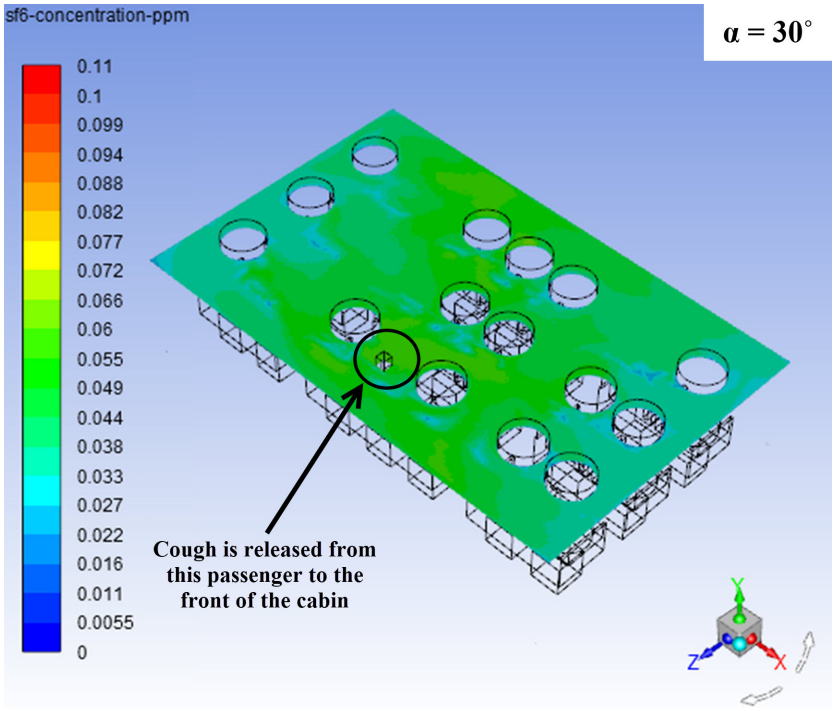

(a)

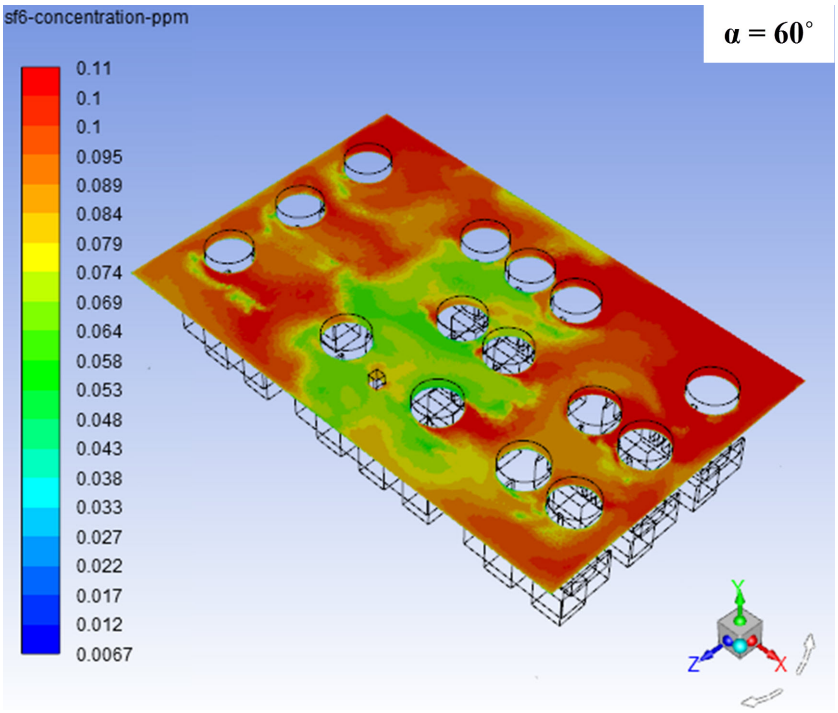

(b)

Figure 7.3: SF_6 concentration contour plots at passenger breathing level during climb leg under aircraft extreme operating conditions at 350 s; (a) using airflow supply angle $\alpha = 30°$, and (b) using airflow supply angle $\alpha = 60°$.

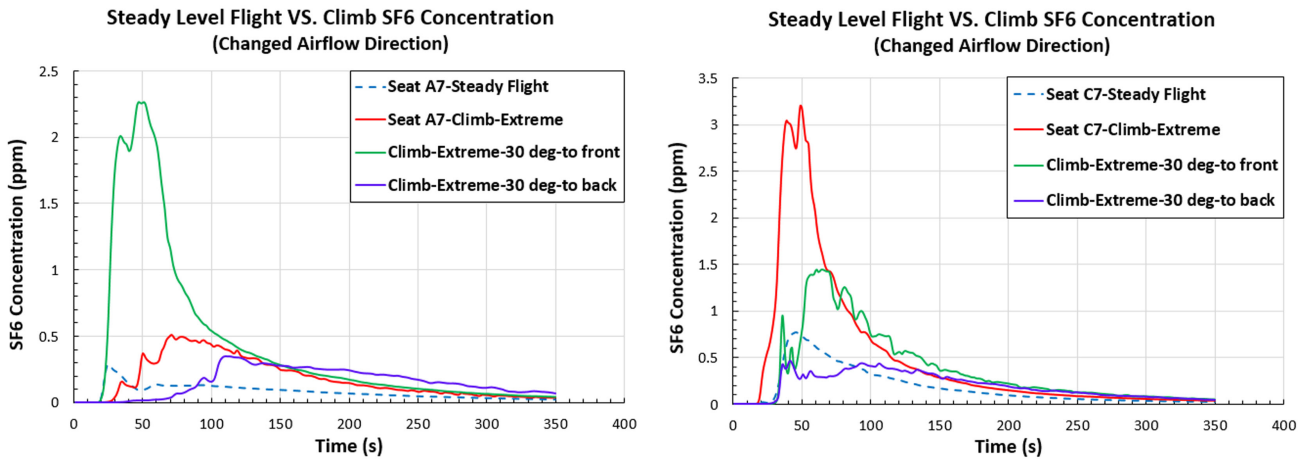

(a) (b)

Figure 7.4: Comparison of the predicted SF_6 concentration time series between the steady level flight leg and climb leg under aircraft extreme operating conditions using supply angles $\alpha = 30°$ and $\beta = 30°$ (to front and back) during climb; (a) at seat A7, and (b) at seat C7.

shows a comparison of the three SF_6 concentration time series under the modified airflow rate conditions with the default 200 L s^{-1} case during the climb leg under aircraft extreme operating conditions, in addition to the steady level flight case.

Comparing the concentration time series, it can be noticed that increasing the base airflow by 100% decreases the passenger exposure to SF_6 at the two monitoring points the most. This is followed by the 50% more airflow rate case, which leads to a slightly higher exposure than the previous case. Conversely, decreasing the original airflow rate by 50% of its amount led to higher overall exposure at seat A7 and almost the same exposure as the original at seat C7. This latter finding is generally expected because less airflow means more ability of the contaminant to disperse freely in the cabin under the effect of the cough momentum without a sufficient bulk of ventilation air to control it.

However, the 100% more airflow rate case cannot be generally preferred over the 50% more airflow rate based on economic considerations as the former requires more energy consumption, and consequently more fuel utilization, than the latter. Figure 7.7 shows the dispersion behavior of the contaminant in the cabin at 350 s after release using contours for the investigated cases.

From Figure 7.7, one can see that both the 100% more airflow and the 50% less airflow scenarios significantly enhance the contaminant dispersion in the cabin but using two different mechanisms. While the 100% more airflow case favors a longitudinal dispersion

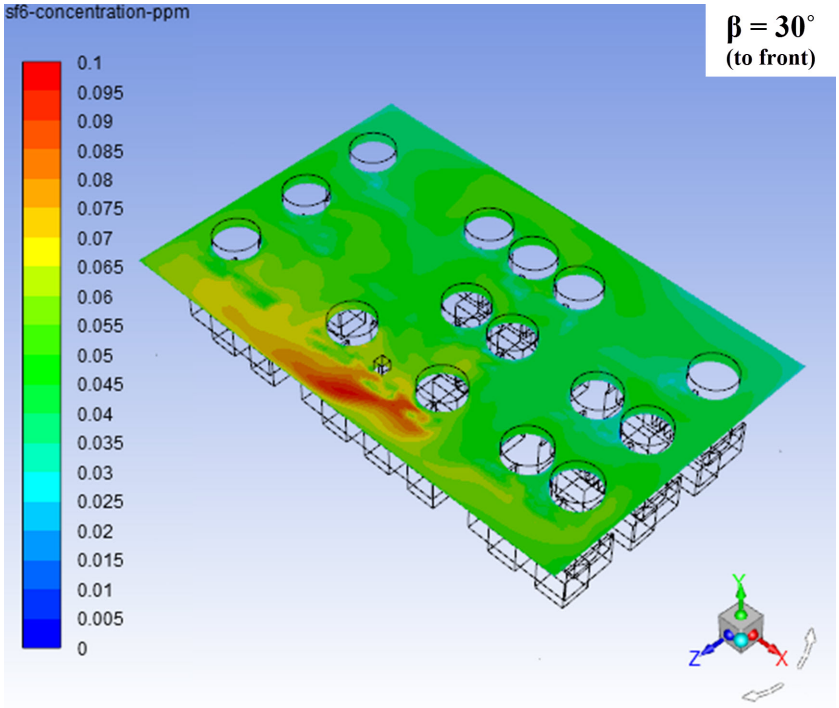

(a)

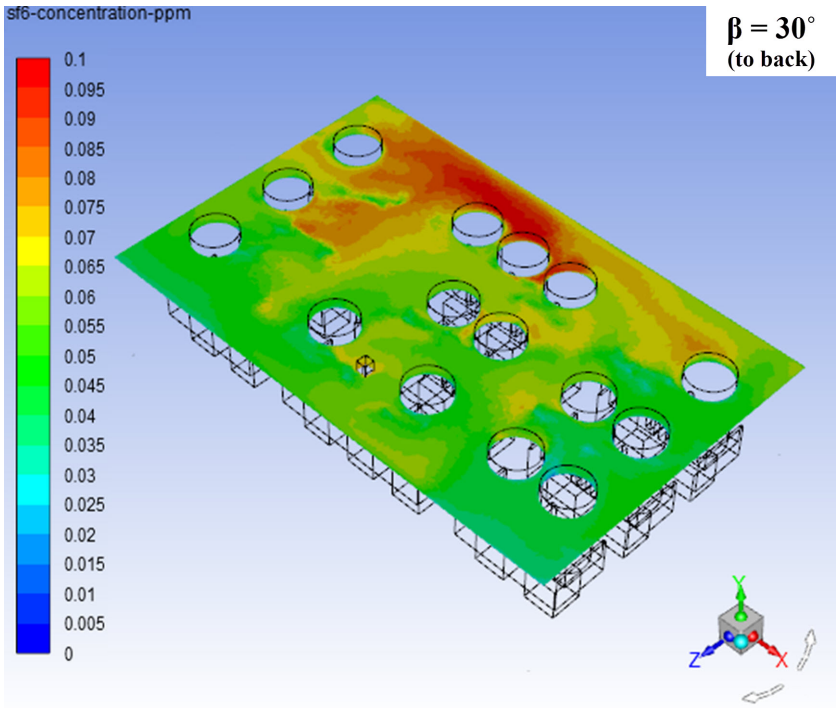

(b)

Figure 7.5: SF_6 concentration contour plots at passenger breathing level during climb leg under aircraft extreme operating conditions at 350 s; (a) using airflow supply angle $\beta = 30°$ to the front, and (b) using airflow supply angle $\beta = 30°$ to the back.

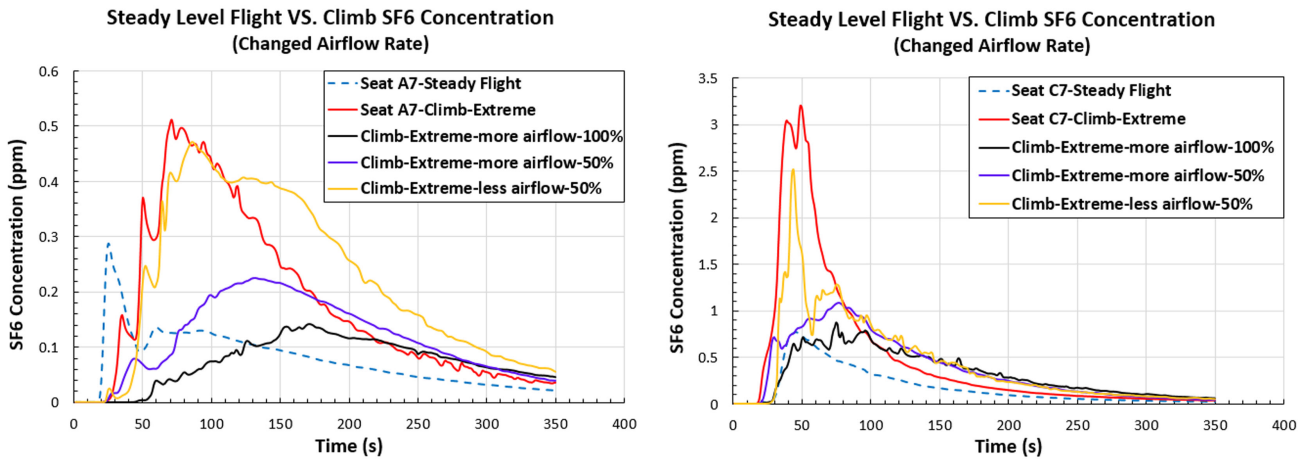

(a) (b)

Figure 7.6: Comparison of the predicted SF_6 concentration time series between the steady level flight leg and climb leg under aircraft extreme operating conditions using 100% more, 50% more, and 50% less supply airflow rates with respect to the original climb flow rate; (a) at seat A7, and (b) at seat C7.

mechanism for the contaminant from the front rows to the back rows of seats, a lateral dispersion mechanism occurs for the 50% less airflow case to mainly move the contaminant from the right side of the cabin to the left side. On the other hand, the 50% more airflow case applies a similar longitudinal dispersion scheme to that for the 100% more airflow, however, the former is capable of trapping the contaminant at the back of the cabin and reducing its dispersion. This advantage not only significantly decreases the exposure at seats A7 and C7, but also decreases the exposure of the occupants at most cabin seats. This makes the 50% more airflow case superior to the 100% more airflow case during the climb leg under aircraft extreme operating conditions.

7.2 Source Control Strategies

7.2.1 Cough Direction

Similar to the investigation for the steady level flight leg, the cough direction is tilted vertically with specific angles either downwards or upwards from the horizontal (with $\theta = 0°$) during the climb leg under aircraft extreme operating conditions. The angles used are 30° and 40° downwards, in addition to 30° upwards. Figure 7.8 shows the SF_6 concentration

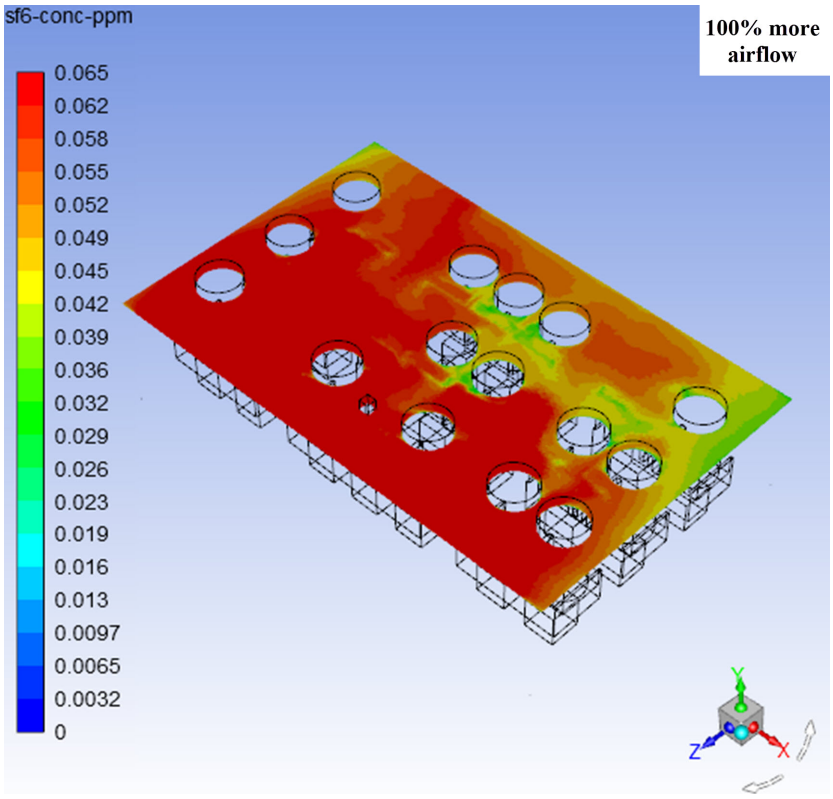
sf6-conc-ppm
0.065
0.062
0.058
0.055
0.052
0.049
0.045
0.042
0.039
0.036
0.032
0.029
0.026
0.023
0.019
0.016
0.013
0.0097
0.0065
0.0032
0
100% more airflow
Y
Z
X

(a)

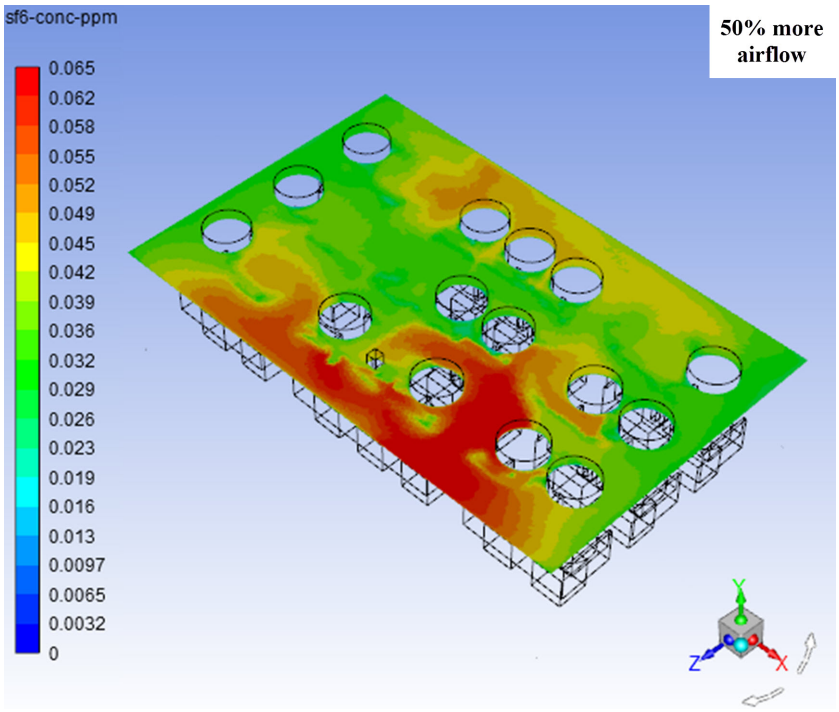
sf6-conc-ppm
0.065
0.062
0.058
0.055
0.052
0.049
0.045
0.042
0.039
0.036
0.032
0.029
0.026
0.023
0.019
0.016
0.013
0.0097
0.0065
0.0032
0
50% more airflow
Y
Z
X

(b)

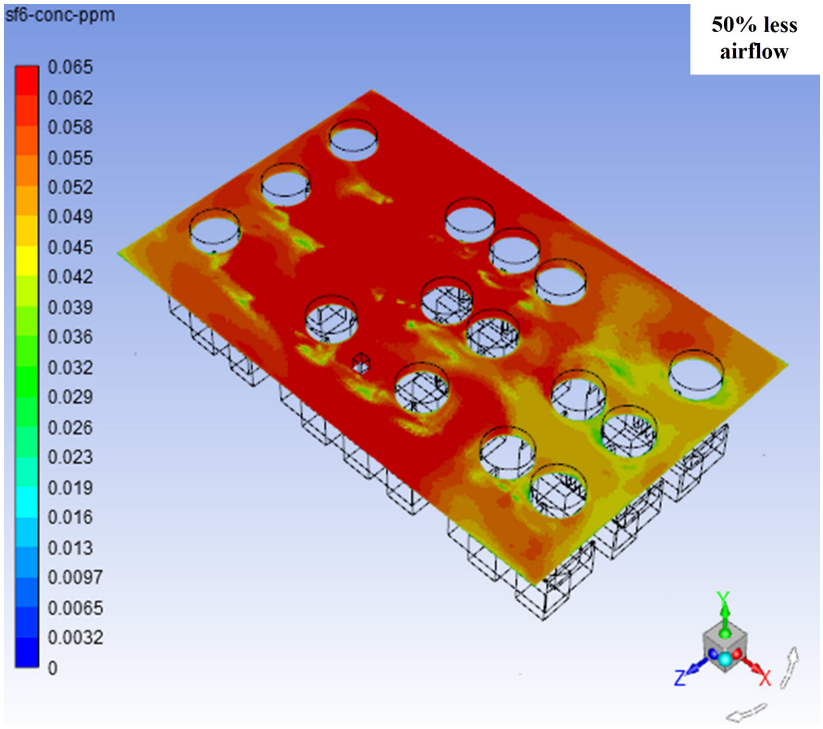

(c)

Figure 7.7: SF_6 concentration contour plots at passenger breathing level during climb leg under aircraft extreme operating conditions at 350 s; (a) using 100% more airflow rate, (b) using 50% more airflow rate, and (c) using 50% less airflow rate.

time series calculated at seats A7 and C7 in the cabin for the three cough direction angles employed.

Looking at Figure 7.8, the predicted concentration time series for the 30° downwards and 40° downwards are almost fully coincident. Similar to the case during the steady level flight leg, this indicates that increasing or decreasing the cough direction angle for the same cough orientation has almost no effect on the dispersion pattern of the contaminant and its concentration in the cabin during the climb leg under aircraft extreme operating conditions. On the other hand, when the cough was directed upwards using $\theta = 30°$, the exposure was significantly higher than the ones for the downwards cough direction. This finding also agrees well with the previous results for the upwards cough orientation during the steady level flight. Figure 7.9 depicts the difference between the SF_6 contour plots in the cabin at the end of simulation time under the 30° downwards and 30° upwards cough release conditions during the climb leg under aircraft extreme operating conditions.

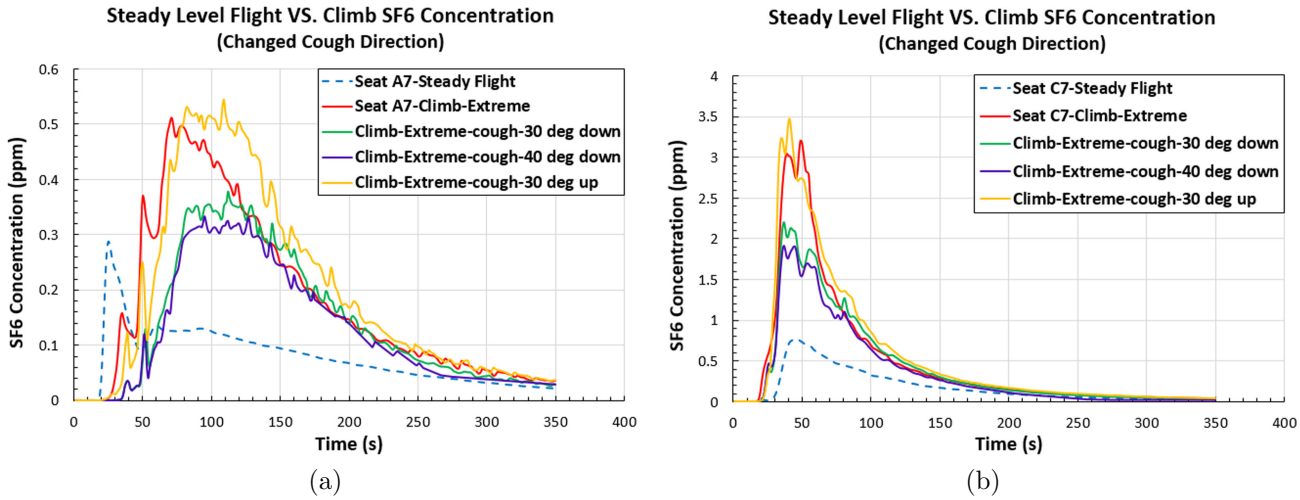

(a) (b)

Figure 7.8: Comparison of the predicted SF_6 concentration time series between the steady level flight leg and climb leg under aircraft extreme operating conditions using the 30° downwards, 40° downwards, and 30° upwards cough direction angles during climb; (a) at seat A7, and (b) at seat C7.

Releasing a cough with 30° upwards causes higher concentration of the released contaminant at the breathing level of the passengers everywhere in the cabin space especially in the central region. Such a local increase in the concentration can be attributed to the location of the cougher, which is the middle seat of the back row in this case. In comparison, the

cough released by the same person at 30° in the downward direction created a central buildup pattern of the contaminant as well, but with much less concentrations which leads to about 30% less passenger exposure than the 30° upwards cough case at most cabin locations.

7.2.2 Cough Velocity

The second source control strategy investigated for its ability to reduce the passenger exposure to the cough-released airborne contaminant during the climb leg under aircraft extreme operating conditions is changing the cough velocity.

For the case of the climb leg under aircraft extreme operating conditions, and following-up on the results from the same investigation during the steady level flight leg, the variable cough release velocity approach is only considered here. This is because the other fixed released contaminant mass approach previously investigated in Chapter 5 deemed to be impractical and unrealistic due to the excessively low contaminant concentration predicted for it throughout the whole simulation time with respect to the baseline steady level flight case.

Figure 7.10 shows the concentration time series for the high cough release velocity (20 m s^{-1}) and the low cough release velocity (5 m s^{-1}) in comparison to the baseline climb leg under aircraft extreme operating conditions with 10.6 m s^{-1} cough velocity and the steady level flight case

Similar to the dispersion behavior noticed during the steady level flight leg, releasing the cough with the high velocity of 20 m s^{-1} led to decreased contaminant concentration compared to the original velocity of 10.6 m s^{-1} for most of the simulation time. Conversely, the lower cough release velocity (5 m s^{-1}) results in a contaminant concentration time series that is almost similar to that for the baseline case with 10.6 m s^{-1} cough velocity. This indicates that as the cough release velocity decreases, the local peak concentration of the released contaminant in the cabin adopts an increasing trend. Also, the difference between this local peak concentration and that for further lower cough velocities cannot be distinguished. Such increase in local peak contaminant concentration causes higher passenger exposures to the contaminant at different seats.

Figure 7.11 shows the SF_6 concentration contours for the three cough velocity cases. It can be seen that the dispersion pattern of the contaminant in the cabin, especially at the center, is almost identical between the 5 m s^{-1} and 20 m s^{-1} cough velocity cases at the end of simulation time. This high resemblance between the two cases is slightly violated at the two

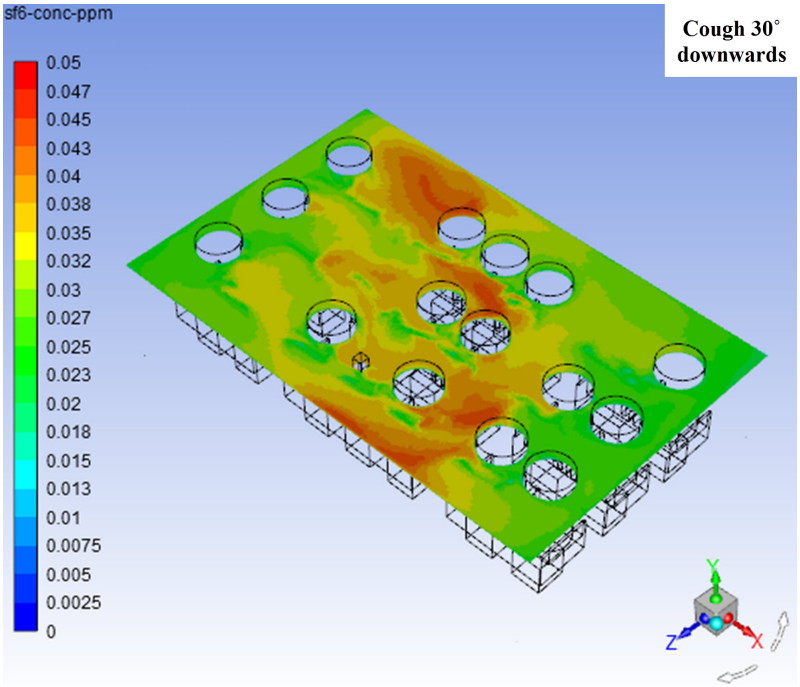

(a)

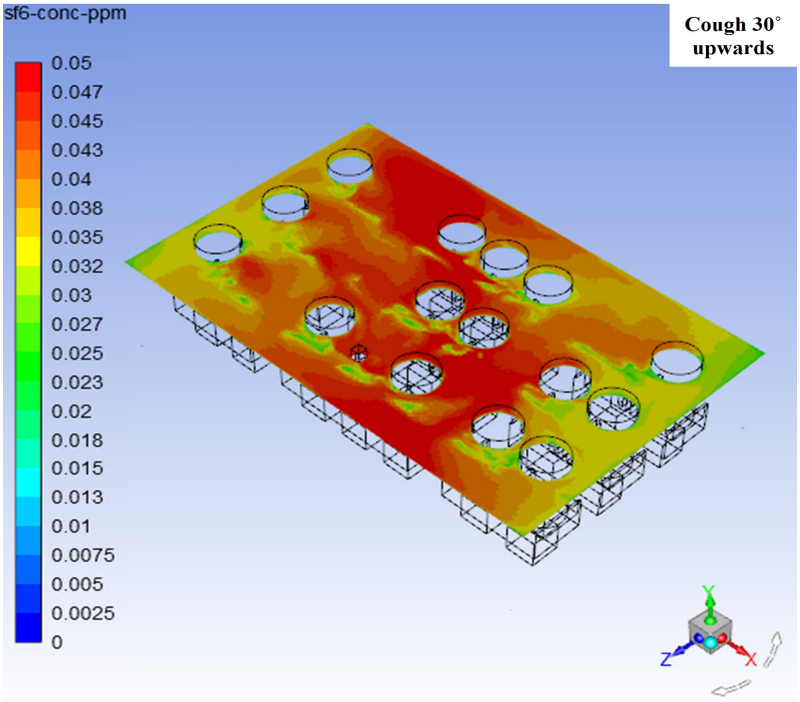

(b)

Figure 7.9: SF_6 concentration contour plots at passenger breathing level during climb leg under aircraft extreme operating conditions at 350 s; (a) using cough direction angle $\theta = 30°$ downwards, and (b) using cough direction angle $\theta = 30°$ upwards.

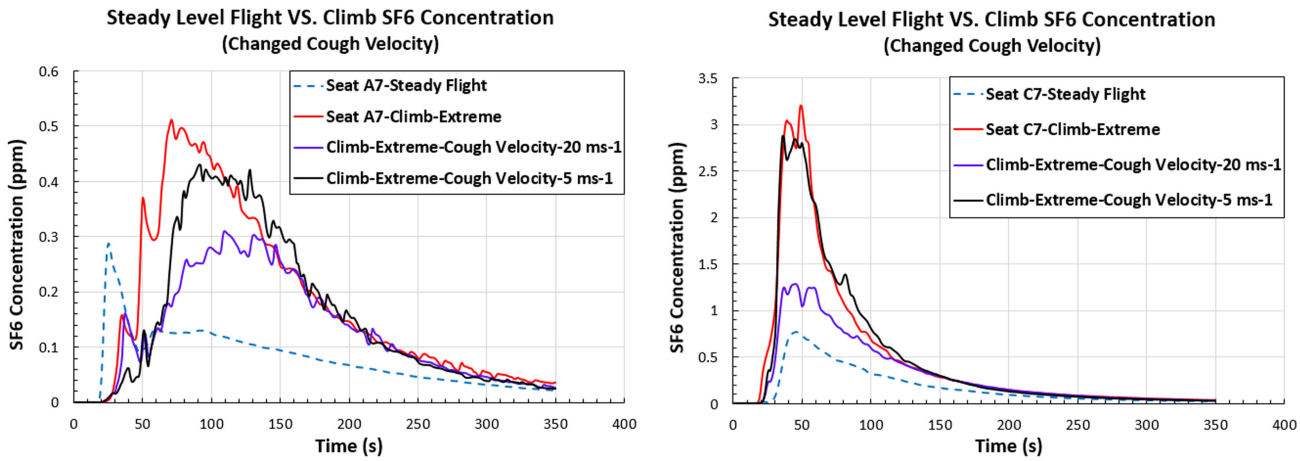

(a) (b)

Figure 7.10: Comparison of the predicted SF_6 concentration time series between the steady level flight leg and climb leg under aircraft extreme operating conditions using the 20 m s^{-1} and 5 m s^{-1} cough release velocities during climb; (a) at seat A7, and (b) at seat C7.

cabin sides where the contaminant concentration is lower for the 20 m s^{-1} case than the 5 m s^{-1} one for most of the simulation time. However, starting from around 200 s after the cough release, the concentration on the sides become higher for the 20 m s^{-1} case. In contrast, for the 10.6 m s^{-1} cough velocity, the contaminant was further dispersed to the two cabin sides than the other two cases.

Generally, the three cough release velocity cases led to contaminant dispersion behavior in the cabin without a clear trend, and no one case clearly results in a better air quality condition during the climb leg under aircraft extreme operating conditions.

7.2.3 Cougher Location in the Cabin

The effect of moving the cougher from the center of the back row on the contaminant dispersion behavior and the passenger exposure during the climb leg under aircraft extreme operating conditions is investigated in this section. Similar to the steady level flight case, the cougher is moved to either the central row on the left side of the cabin (LC) or the front row on the right side (RF), looking from the back of the cabin to the front.

Figures 7.12 and 7.13 show the SF_6 concentration time series at the two seats A7 and C7 with the cougher positions at locations LC and RF, respectively. The series for the two cases were separated to enhance their readability.

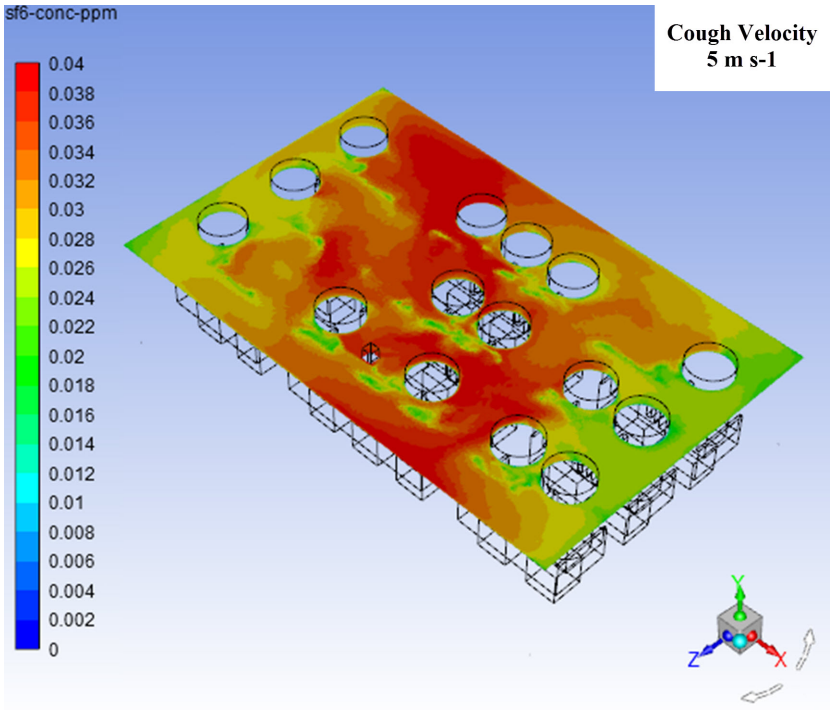
sf6-conc-ppm
0.04
0.038
0.036
0.034
0.032
0.03
0.028
0.026
0.024
0.022
0.02
0.018
0.016
0.014
0.012
0.01
0.008
0.006
0.004
0.002
0
Cough Velocity
5 m s-1
Y
Z
X

(a)

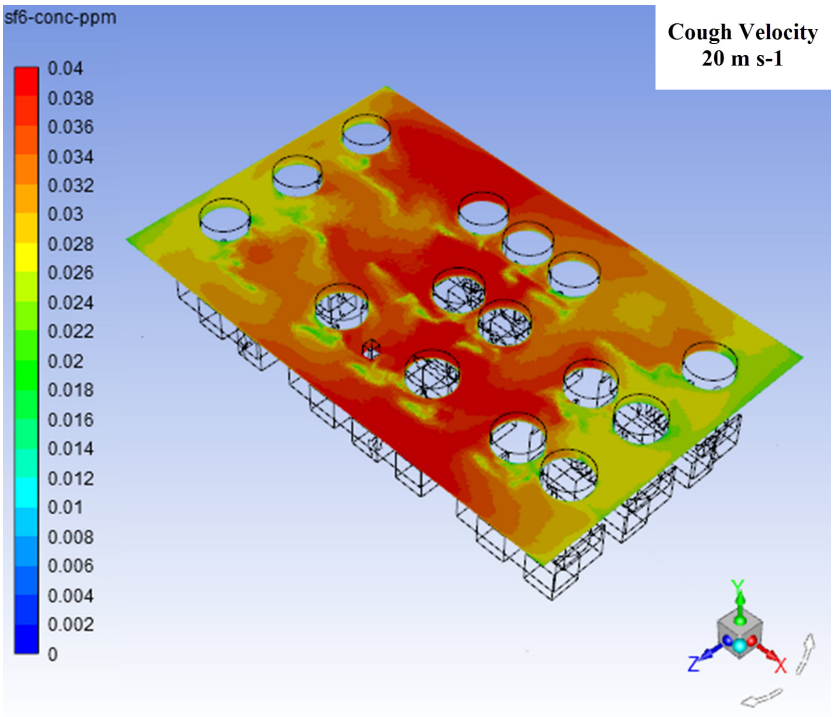
sf6-conc-ppm
0.04
0.038
0.036
0.034
0.032
0.03
0.028
0.026
0.024
0.022
0.02
0.018
0.016
0.014
0.012
0.01
0.008
0.006
0.004
0.002
0
Cough Velocity
20 m s-1
Y
Z
X

(b)

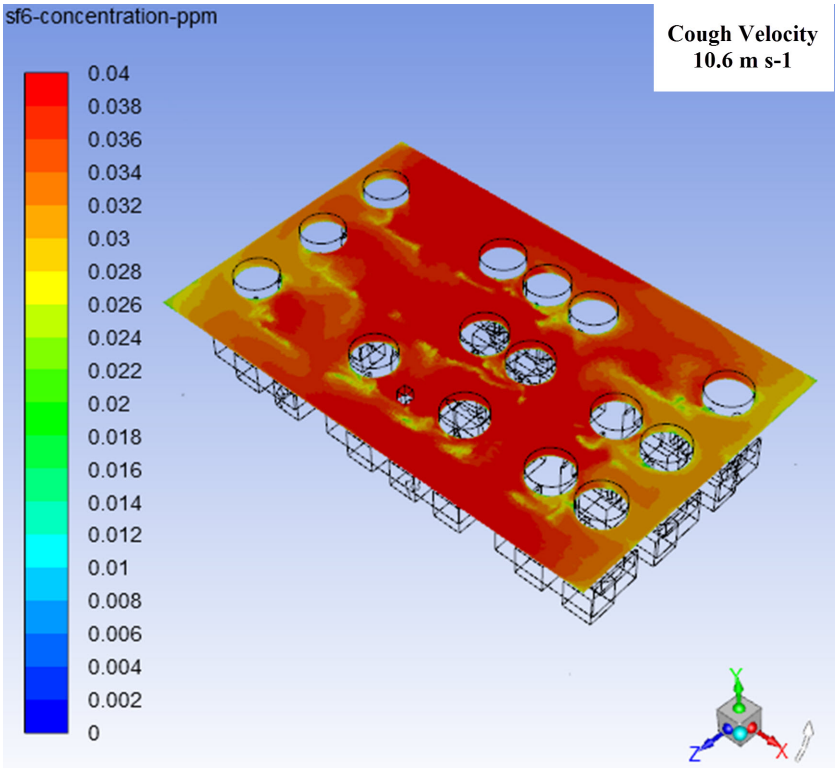

(c)

Figure 7.11: SF_6 concentration contour plots at passenger breathing level during climb leg under aircraft extreme operating conditions at 350 s; with (a) 5 m s^{-1} cough velocity, (b) 20 m s^{-1} cough velocity, and (c) 10.6 m s^{-1} cough velocity.

Looking at the time series, and as the cougher moves to the LC location, the concentration at the two monitors for the full simulation time was substantially reduced to low levels (0.2 ppm and 0.5 ppm for seats A7 and C7, respectively). This is because the cougher at the LC location is moved away by a nearly equal distance from the two monitoring points. Conversely, as the cougher moves to the RF location, which is very close to the monitoring point at seat A7, the contaminant concentration at this point increased to about eight-fold its peak value with respect to the original climb case under aircraft extreme operating conditions. At seat C7, however, the contaminant concentration time series was much lower (about six-fold less) than the baseline climb case under aircraft extreme operating conditions because the cougher was moved further away from it.

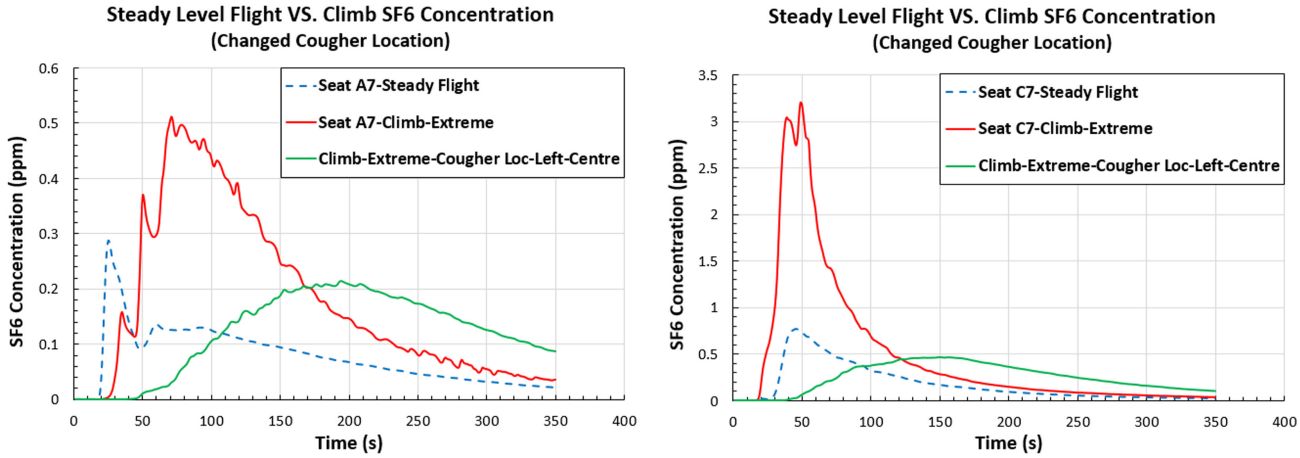

(a) (b)

Figure 7.12: Comparison of the predicted SF_6 concentration time series between the steady level flight leg and climb leg under aircraft extreme operating conditions with the cougher moved to the center row on the left side of the cabin during climb; (a) at seat A7, and (b) at seat C7.

With a similar effect to that during the steady level flight leg, and in addition to the cougher proximity to other occupants, the airflow patterns in the cabin, and the closeness of the cougher to walls or surfaces can very well influence the contaminant dispersion behavior and the exposure of the passengers to it. The concentration contour plots for the two cougher location cases are shown in Figure 7.14.

From the contour plot for the LC cougher location, it can be noticed that the contaminant reside at the back of the cabin at the end of simulation time. This is impacted by the airflow

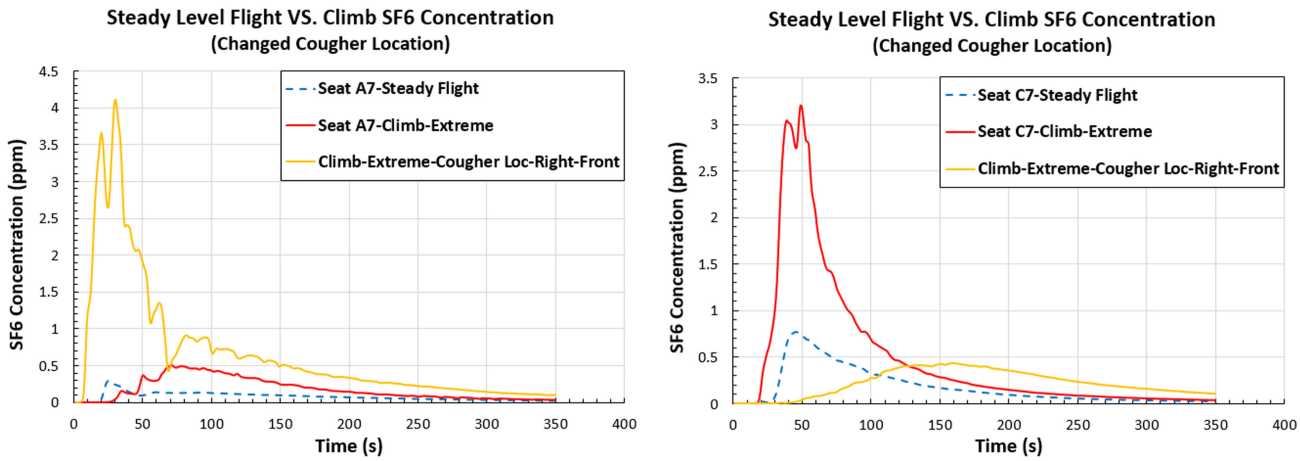

(a) (b)

Figure 7.13: Comparison of the predicted SF_6 concentration time series between the steady level flight leg and climb leg under aircraft extreme operating conditions with the cougher moved to the front row on the right side of the cabin during climb; (a) at seat A7, and (b) at seat C7.

in the cabin and the body forces during aircraft climb, which push the contaminant to the back rows from the front of the cabin on the left side where it initially dispersed after release. Differently, the contaminant released from the cougher in the RF position disperses along the front wall to the left before it disperses to the back of the cabin.

Table 7.1 lists the passenger exposure ratio between the various cases studied in this chapter and the baseline climb case under aircraft extreme operating conditions. The lowest exposure ratios are in bold font.

The exposure values were calculated using equation 5.2 and applying the composite Simpson's and the composite trapezoidal rules in determining the area under the curve for each concentration time series.

Looking at Table 7.1, the lowest average exposure ratio between the two seats is found for the 100% more airflow rate case. Cases that come after are the left-side, center-row relocation of the cougher, the $\alpha = 30^{\circ}$ airflow direction, and the 50% more airflow rate. However, for energy saving considerations (exact quantities of savings depend on the model and design aspects of the passenger aircraft), the latter three cases are preferred over the former one. Such airflow design and/or source control strategies could be implemented to reduce the exposure of the aircraft occupants to expiratory contaminants released in this aircraft cabin, especially during the climb leg under aircraft extreme operating conditions.

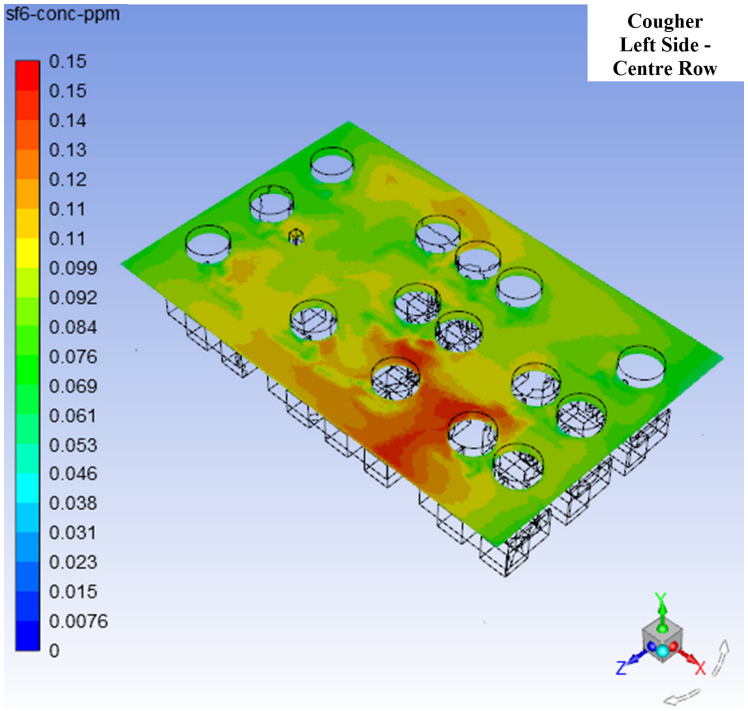

(a)

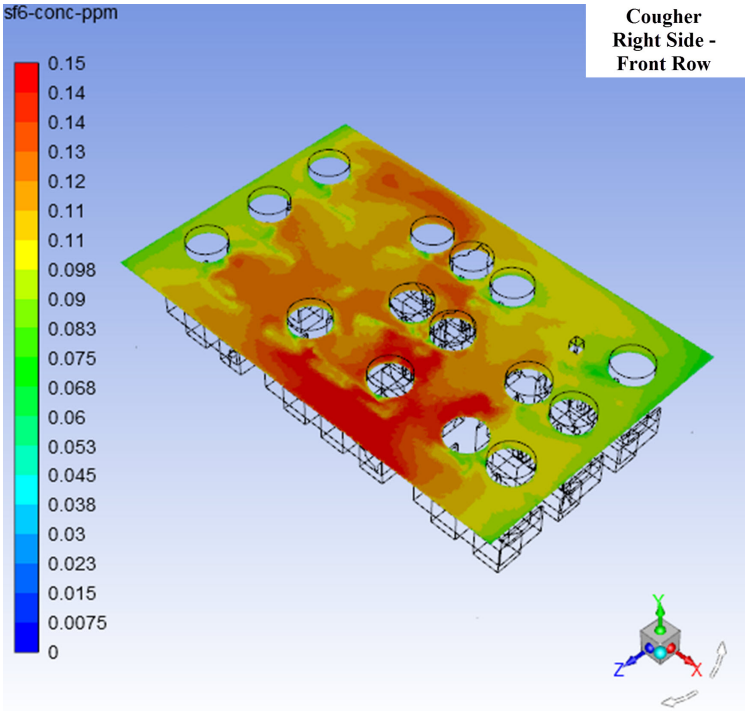

(b)

Figure 7.14: SF_6 concentration contour plots at passenger breathing level during climb leg under aircraft extreme operating conditions at 350 s; with (a) the cougher located at the center row on the left side of the cabin, and (b) the cougher located at the front row on the right side of the cabin.

Nevertheless, the highest exposure ratio is noticed for the $\alpha = 60°$ airflow direction scenario. This is followed by the occurrence in which the cougher is moved to the front row on the right side of the cabin, and later by setting $\alpha = 30°$ and $\beta = 30°$ to the front as airflow direction condition.

Table 7.1: Ratio of passenger exposure between different parametric sensitivity cases and the baseline climb case under aircraft extreme operating conditions at the two monitoring locations.

Case	Passenger exposure ratio to baseline climb (extreme)	
	Seat A7	Seat C7
$\alpha = 20°$ airflow	1.1 : 1	0.9 : 1
$\alpha = 30°$ airflow	**0.7 : 1**	**0.5 : 1**
$\alpha = 60°$ arflow	3.5 : 1	2.1 : 1
$\alpha = 30°$ and $\beta = 30°$ to front	2.4 : 1	0.7 : 1
$\alpha = 30°$ and $\beta = 30°$ to back	**0.9 : 1**	**0.4 : 1**
100% more airflow rate	**0.4 : 1**	**0.6 : 1**
50% more airflow rate	**0.6 : 1**	**0.7 : 1**
50% less airflow rate	1.2 : 1	0.8 : 1
Cough 30° downwards	**0.8 : 1**	**0.8 : 1**
Cough 40° downwards	**0.7 : 1**	**0.6 : 1**
Cough 30° upwards	1.1 : 1	1.1 : 1
Cough velocity 20 m s^{-1}	**0.7 : 1**	**0.6 : 1**
Cough velocity 5 m s^{-1}	0.9 : 1	1 : 1
Cougher at left side-center row	**0.7 : 1**	**0.5 : 1**
Cougher at right side-front row	3.9 : 1	0.4 : 1

7.3 Conclusions

In chapter 7, airflow design and source control strategies were investigated for their potential in reducing cough-released airborne contaminant exposure in the cabin of a passenger aircraft (Boeing 767-300) during the climb leg under aircraft extreme operating conditions.

The airflow design strategies investigated involved altering the supply airflow direction

and changing the supply airflow rate. Moreover, the source control strategies employed involved changing the cough direction, varying the cough release velocity or volumetric flowrate, and moving the cougher to different locations in the cabin.

Changing the airflow supply angle from the ceiling only, or α, from 20° to 60° had different effects on the SF_6 dispersion behavior in the cabin. The angle $\alpha = 30°$ led to the lowest passenger exposure. However, the 20° and 60° angles, compared to passenger exposure of the baseline climb case with $\alpha = 0°$, resulted in similar and higher exposures, respectively. Further, when a three-dimensional approach was introduced to the airflow redirection scenario through the angle β, directing the airflow to the back of the cabin led to less passenger exposure than directing it to the front.

The supply airflow rate to the cabin was changed from the baseline 200 L s^{-1} case to 100% increase, 50% increase, and 50% decrease. Following the expected notion, the 100% more airflow scenario led to the highest reduction in passenger exposure locally at the two monitoring points preceded by the 50% more flow rate. The 50% less airflow rate was not desirable as it increased exposure. However, cabin-wide, increasing airflow rate by 100% enhanced the contaminant spread as much as the 50% decrease did. From other practical considerations, the energy consumption that is required for the 100% increase case is significantly higher than other cases. For all these reasons, raising the supply airflow with 50% was found to be the optimal scenario during the climb leg under aircraft extreme operating conditions.

For the source control strategies, changing the cough direction was able to reduce the exposure of the passengers to the released contaminant. This occurred when the cough was directed downwards either with 30° or 40° from the horizontal direction, although no significant difference in exposure alleviation was noticed between the two angles for the same cough orientation. On the other hand, directing the cough upwards contributed to increasing the exposure over that for the baseline climb case under aircraft extreme operating conditions.

Changing the cough release velocity, and on local level at the two monitoring points, the higher cough velocity of 20 m s^{-1} led to reduced exposure than the lower velocity of 5 m s^{-1}. Nevertheless, cabin-wide, the contaminant dispersion behavior did not show a clear trend, and none of the two cough velocities clearly resulted in a better air quality condition.

As a last strategy, relocating the cougher to other locations in the cabin other than the original position at the center seat in the back row had a considerable effect on the dispersion behavior of the contaminant and the exposure of passengers to it. Moving the cougher to the left side of the cabin in the center row (LC location) led to decreased passenger exposure

both locally at the monitoring locations, and as an average in the whole cabin. On the other hand, moving the cougher to the right side of the cabin in the front row (RF location) caused a substantial increase in the exposure at seat A7, while it halved the exposure at seat C7 because the cougher was moved away from it. In addition to the proximity of the cougher to specific passengers, the airflow patters in the cabin, the body forces on the aircraft during the climb leg under aircraft extreme operating conditions, and the existence of walls and/or surfaces near the cougher all have confounding effects on the resulted contaminant dispersion behavior from different cougher locations.

In total, the cases that showed the greatest reduction in passenger exposure as an average between the two monitoring locations at seats A7 and C7 with respect to the baseline climb case are: the left-side, center-row relocation of the cougher, the $\alpha = 30^\circ$ airflow direction, and the 50% more airflow rate. The exposure ratios are $0.7 : 1$ at seat A7 and $0.5 : 1$ at seat C7 for the first case, $0.7 : 1$ at seat A7 and $0.5 : 1$ at seat C7 for the second case, and $0.6 : 1$ at seat A7 and $0.7 : 1$ at seat C7 for the third case, respectively. On the other hand, the highest exposure in average between the two seats belongs to the $\alpha = 60^\circ$ airflow direction case with $3.5 : 1$ at seat A7 and $2.1 : 1$ at seat C7.

Chapter 8

Comparison of Particulate Contaminant Dispersion behavior in the Aircraft Cabin between the Climb Leg under Extreme Operating Conditions and the Steady Level Flight Leg

In this chapter, particles of several sizes are used to represent the expiratory contaminant released from the cough instead of the SF_6 gas. This is performed to compare the particulate contaminant dispersion behavior in the aircraft cabin between the climb leg under aircraft extreme operating conditions and the steady level flight leg. Also, the exposure ratios previously quantified using the SF_6 gaseous contaminant surrogate at the two monitoring locations in the cabin are compared against that for fine cough particle (<5 µm in diameter), and to extend the study to include coarser particles usually generated from cough (>5 µm in diameter).

This investigation follows the theme of several studies in the literature which used particles of different sizes to model expiratory contaminant dispersion from coughing and sneezing [67, 83, 100].

8.1 Cough-Released Particles

Three particle diameter sizes have been utilized in this investigation, namely: 2.5 µm representing fine cough particles, and 7.5 and 10 µm for coarse particles. Figure 8.1 shows the concentration of the cough-released particles averaged over the cabin volume in kg m^{-3} versus the simulation time in seconds for the three investigated particle sizes.

From Figure 8.1, it can be noticed that every particle size has a different residence time in the cabin space, and that this time is also influenced by the body forces on the aircraft and the change in the airflow patterns as evident from the dissimilar volume-averaged particle concentration and residence time in the cabin between the climb leg under aircraft extreme operating conditions and the steady level flight leg.

Starting with the smallest particle diameter investigated, i.e. 2.5 µm, which represents the fine cough-released particles, they stayed in the cabin for about 19 s after injection without settling or being trapped on a surface during the steady level flight leg. However, this residence time decreased to 8 s only during the climb leg under extreme conditions. This difference can be attributed to the ability of those small particles to dilute and disperse in the cabin further during the steady flight leg, while they dispersed in the limited cabin rear area only during the climb leg and exited from the domain faster.

Also, the smallest size particles produced by a cough (2.5 µm in diameter and less) have their dispersion behavior primarily influenced by the buoyancy forces in the cabin space [3]. The buoyancy forces in the cabin are mainly induced by the thermal plumes released from occupants' bodies, which are in turn enhanced by the intensfied airflow circulation strength during the climb leg under extreme conditions from the steady flight leg (look at subsection 6.2.2). Therefore, all those factors combined lead to decrease the residence time of the 2.5 µm particles in the cabin from the steady level flight leg to the climb leg under extreme operating conditions by being discharged from the cabin or settled on a surface within it with a substantially faster rate (around 2.4 times faster) during the climb leg.

Similar behavior is observed for the 10 µm particles, which are the coarsest particles investigated. The 10 µm particles stayed for longer time (31 s) than the 2.5 µm particles in the cabin during the steady flight leg due to their larger inertia and slower dispersal rate. However, during the climb leg under extreme conditions, the 10 µm particles were faster to settle than the 2.5 µm particles (5 s for the former versus 8 s for the latter). This is because the body forces on the aircraft during the climb leg under extreme conditions moved the coarse particles to the back section of the cabin where they contacted the walls and surfaces

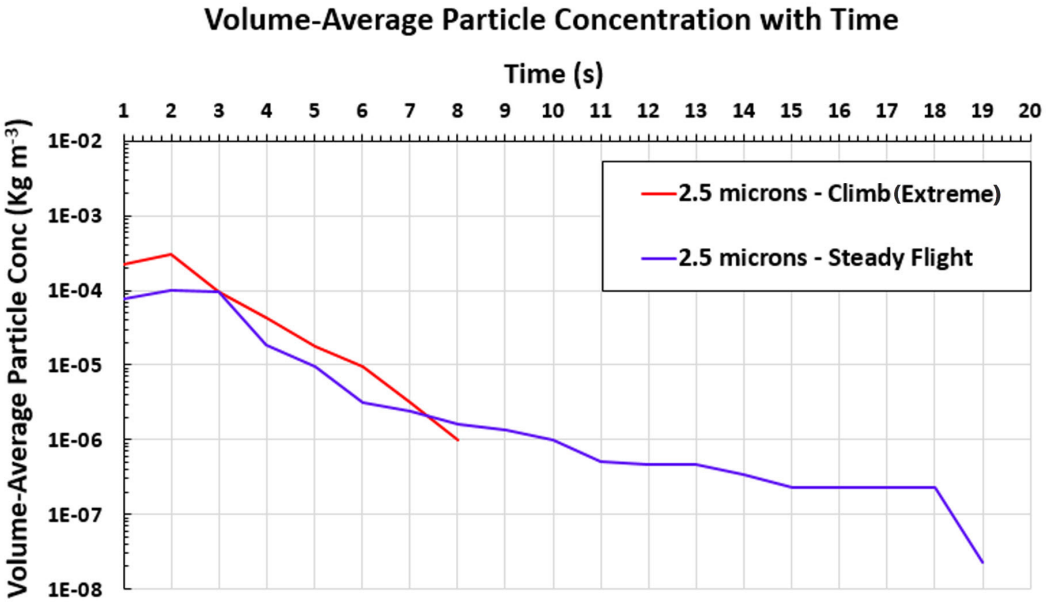
Volume-Average Particle Concentration with Time
Time (s)
1 2 3 4 5 6 7 8 9 10 11 12 13 14 15 16 17 18 19 20
Volume-Average Particle Conc (Kg m-3)
1E-02
1E-03
1E-04
1E-05
1E-06
1E-07
1E-08
2.5 microns - Climb (Extreme)
2.5 microns - Steady Flight

(a)

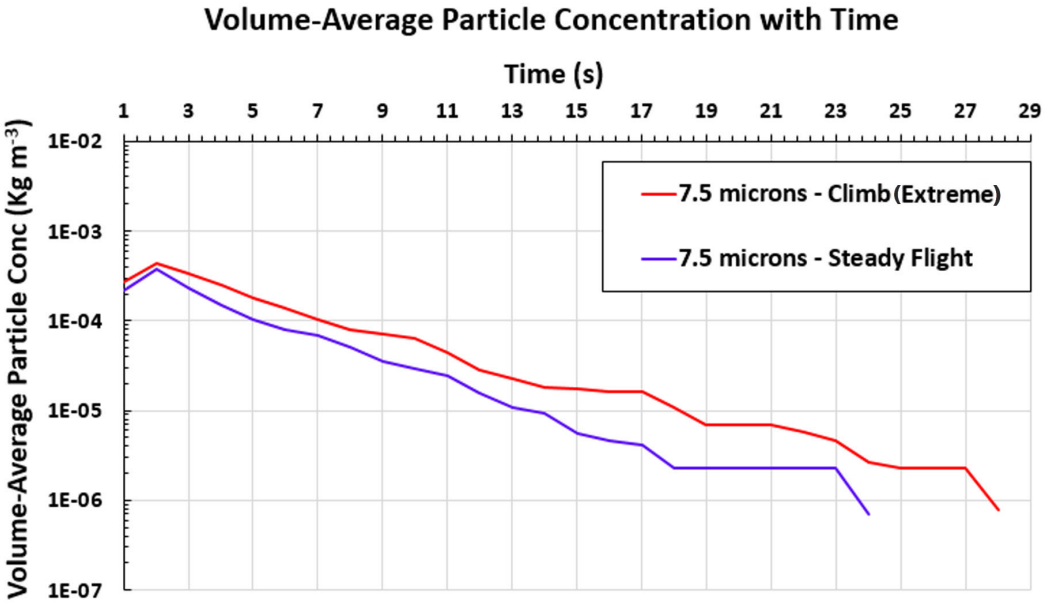
Volume-Average Particle Concentration with Time
Time (s)
1 3 5 7 9 11 13 15 17 19 21 23 25 27 29
Volume-Average Particle Conc (Kg m-3)
1E-02
1E-03
1E-04
1E-05
1E-06
1E-07
7.5 microns - Climb (Extreme)
7.5 microns - Steady Flight

(b)

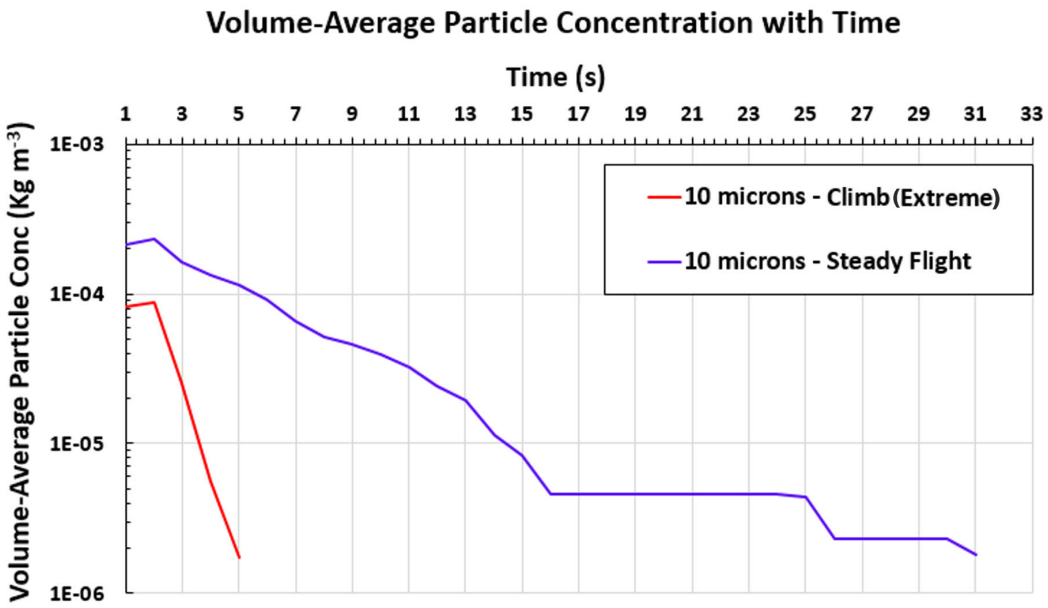

(c)

Figure 8.1: Comparison of the volume-averaged particle concentration in the cabin with simulation time between the climb leg under aircraft extreme operating conditions and the steady level flight leg for three particle sizes: (a) 2.5 µm, (b) 7.5 µm, and (c) 10 µm.

faster due to their larger size. This faster settling rate during the climb leg is also motivated by the increased drag forces on the 10 µm particles which primarily affect the dispersion behavior of similar large size particles. In comparison to the buoyancy forces dominating the motion of small particles, the drag forces are more potent, and they were able to push the 10 µm particles to the back of the cabin during the climb leg under extreme conditions, where they settled, in a very brief time.

Differently, the particles with the intermediate size of 7.5 µm, and unlike the 2.5 and 10 µm particles, are not ultimately dominated by a single force in terms of their dispersion behavior in the cabin. Instead, the motion of the 7.5 µm particles is affected by a combination of the drag, buoyancy and gravity forces with no one dominant force over the others. This provides the possibility for the interaction among the effects of the three forces on the 7.5 µm particles by opposition or accordance making the dispersion behavior of those intermediate size particles in the cabin under the effect of the aircraft body forces difficult to predict and/or define. This is evident in Figure 8.1 (b) as the 7.5 µm particles remained for 24 s after injection in the cabin during the steady level flight leg, while they stayed for 28 s during the climb leg under aircraft extreme operating conditions. This resemblance in the particles residence times between the two legs, which does not follow the theme of the 2.5 µm and 10 µm particles, indicate that the 7.5 µm particles are the least affected size by the body forces acting on the aircraft during the climb leg under extreme operating conditions. Also, this finding indicates that expiratory airborne particles of intermediate size (around 7.5 µm in diameter) can pose the greatest infection risk on the passengers as they remain in the cabin for relatively longer times for almost the whole flight duration whatever the flight leg is.

8.2 Passenger Exposure Ratios

Table 8.1 illustrates the ratio of passenger exposure to the different particle sizes between the climb leg under aircraft extreme operating conditions and the steady level flight leg taken as an average over the full cabin volume.

From Table 8.1, the highest passenger exposure ratio between the two legs is noticed for the 2.5 µm particles with 2.2 times during the climb leg under aircraft extreme operating conditions than the steady flight leg, while the least is for the 10 µm with 0.2 to 1 ratio. However, the 7.5 µm particles retain an intermediate exposure ratio of 1.5 to 1 due to the almost similar dispersion behavior and residence time in the cabin they exhibit between the two legs as previously shown.

Table 8.1: Ratio of passenger exposure to the airborne expiratory particles between the climb leg under extreme conditions and the steady level flight leg as an average over the whole cabin volume.

Particle diameter (µm)	Passenger exposure ratio
2.5	2.2 : 1
7.5	1.5 : 1
10	0.2 : 1

Additionally, the exposure ratio for the 2.5 µm particles closely resembles the exposure values previously calculated in Chapter 6 using the SF_6 expiratory contaminant surrogate at seats A7 and C7 in the cabin, which were 2.4 to 1 and 2.8 to 1, respectively. This result suggests that that the gaseous contaminant can efficiently mimic the dispersion behavior of the expiratory airborne particles in the investigated size range of 1.6 to 3 µm as indicated in Section 4.2 of the current thesis.

8.3 Conclusions

In Chapter 8, particles of different sizes are injected in the cabin to represent the expiratory contaminant released from the cough instead of the SF_6 gas. Three particle diameters have been used, namely: 2.5 µm representing the fine airborne particles, and 7.5 and 10 µm for the coarse particles. The 7.5 µm particles exhibited a dissimilar dispersion behavior to the one noticed for the 2.5 and 10 µm particles. Those intermediate size particles could stay for long time in the cabin without being settled and/or deposited on surfaces, or discharged from the cabin. The residence time for the 7.5 µm particles was not affected by the change in the acceleration-induced body forces between the climb leg under aircraft extreme operating conditions and the steady level flight leg. This indicates that this intermediate expiratory airborne particle size can pose the greatest infection risk on the passengers throughout most of the flight duration.

Chapter 9

Conclusions and Future Work

9.1 Conclusions

The current study conducts an evaluation for the ventilation airflow capability of controlling and/or limiting the passenger exposure to the airborne contaminant released from expiratory events such as coughs. It also investigates the influence of acceleration-induced body forces during the movement of passenger aircraft throughout different flight legs, such as the steady level flight, climb and descent legs on contaminant dispersion behavior and ventilation airflow patterns inside the cabin. The climb and descent cases were studies under two sets of conditions: first, the aircraft normal operating conditions, and second, aircraft extreme operating conditions. For the latter conditions, the passenger aircraft was assumed to perform climb or descent in gusty surroundings. The steady level flight case, during which there is usually no noticeable acceleration (except for gravitational acceleration) as the forces acting on the aircraft are balanced and negate each other in every direction [68], was used as the reference case to which the changes during the climb and descent legs under normal and extreme conditions were compared.

The cabin model created and simulated in this study is for a Boeing 767-300 aircraft following the actual dimensions provided for a full-size mockup in literature [81, 82, 91]. The grid for the cabin model were created and the governing equations were solved using the ANSYS Fluent commercial Computational Fluid Dynamics (CFD) package.

The validation of the model was performed against a set of experimental data provided by Sze To et al. [82], where the predicted concentration time series for the Sulfur Hexafluoride (SF_6) contaminant surrogate at two monitoring locations was compared with the measured concentration time series for the smallest size cough particles in the range from 1.6 µm to

3.0 µm after both were normalized.

After grid convergence testing, it was found that the contaminant concentration solution on the fine grid level showed enough independence from grid size changes, and that the ReNormalization Group (RNG) k-ε turbulence model was the most accurate model in predicting the solution as compared to the extracted experimental measurements. Therefore, both settings have been used for every simulation that was performed.

The findings of the study were divided into multiple chapters. First, various airflow design strategies in addition to source control strategies were proposed and investigated for their ability to mitigate or reduce the exposure of the passengers throughout the steady level flight leg. Second, the effect of acceleration-induced body forces on contaminant dispersion in the aircraft cabin during the climb and descent legs under normal operating conditions was simulated and studied. Third, the climb, and descent legs under aircraft extreme operating conditions were compared with the steady level flight leg for the contaminant dispersion behavior in the cabin, and the resulting passenger exposure ratios at two monitoring locations (seat A7 and seat C7), in addition to the contaminant concentration contours in the cabin-wide space. Moreover, the changes in airflow patterns and airflow circulation from the steady level flight to the climb under aircraft extreme operating conditions, and from steady level flight to the descent under aircraft extreme operating conditions were investigated. Fourth, and as the climb leg under aircraft extreme operating conditions was found to cause the highest passenger exposure to the contaminant at most cabin locations [29], the same airflow design and source control strategies previously applied for the steady level flight case were tested for their capability of reducing the passenger exposure to the cough-released contaminant during the climb leg under aircraft extreme operating conditions. Lastly, and to complement the results found using the gaseous SF_6 contaminant surrogate, a comparison was made for the dispersion behavior of particulate contaminant (or particles) in the aircraft cabin model between the steady level flight leg and the climb leg under aircraft extreme operating conditions.

9.1.1 Climb and Descent Legs Under Aircraft Normal Operating Conditions

Actual commercial passenger aircraft traffic satellite data extracted from the U.S. National Oceanic and Atmospheric Administration (NOAA)'s Aircraft Meteorological Data Relay (AMDAR) satellite system were utilized to quantify the acceleration components of passenger

aircraft under normal operating conditions for a hundred different flights using a second order curve-fitting technique. The vertical and horizontal aircraft acceleration components were implemented in numerical simulations for the climb and descent legs under aircraft normal operating conditions. Generally, it was noticed that the predicted SF_6 concentration time series for the two investigated flight legs did not considerably differ from that for the steady level flight case. The passenger exposure ratios between normal climb and steady level flight which were 0.92 to 1 at seat A7 and 0.77 to 1 at seat C7. Whereas, they were equal to 0.75 to 1 at seat A7 and 0.99 to 1 at seat C7 between normal descent and steady level flight. Based on that, it can be inferred that the acceleration-induced body forces have limited but existent effect on the contaminant dispersion behavior in passenger aircraft cabins during the climb and descent legs under the aircraft normal operating conditions.

9.1.2 Climb and Descent Legs Under Aircraft Extreme Operating Conditions

Under aircraft extreme operating conditions resembling a gusty flight environment, it was found that the body forces due to aircraft acceleration during those climb and descent legs influence the dispersion patterns of the contaminant surrogate in the cabin. This behavior is mainly influenced by the airflow patterns in the cabin throughout the different flight legs. The concentration of the contaminant at the two set monitoring locations, and therefore the passengers' exposure, increased substantially during the climb leg under aircraft extreme operating conditions from the steady level flight with ratios of 2.4 to 1 and 2.8 to 1 at seats A7 and C7, respectively. Conversely, during the descent leg under aircraft extreme operating conditions, the SF_6 concentration did not considerably differ from that during the steady level flight time with exposure ratios limited to 1.3 to 1 at seat A7, and 0.9 to 1 at seat C7. Furthermore, the change in airflow velocities had a significant effect on the airflow patterns and airflow circulation in the cabin. Airflow velocity magnitudes increased everywhere in the simulated cabin during climb under aircraft extreme operating conditions (between 1% and 45% increase) and during descent under aircraft extreme operating conditions (between 6% and 42% increase) compared to the steady level flight case. Airflow circulation strength in every direction inside the cabin, either on the full plane or its four quadrant corners, exhibits both increases and decreases during the climb and descent legs under aircraft extreme operating conditions, with respect to the steady level flight case, with increases occurring more frequently.

9.1.3 Passenger Exposure Reduction Strategies between the Steady Level Flight Leg and the Climb Leg under Aircraft Extreme Operating Conditions

To reduce the exposure of passengers in the aircraft cabin to the cough-released contaminant, airflow design and sources control strategies were implemented during the steady level flight leg and the climb leg under aircraft extreme operating conditions. The airflow design strategies researched involved altering the supply airflow direction and changing the supply airflow rate. On the other hand, the source control strategies employed involved changing the cough direction, varying the cough release velocity or volumetric flow rate, and moving the cougher to different locations in the cabin.

For the steady level flight leg and the climb leg under aircraft extreme operating conditions, it was noticed that changing the airflow supply angle from the ceiling only, or α, from 20° to 60° had different effects on the SF_6 dispersion behavior in the cabin. In the steady level flight case, The angle $\alpha = 20°$ led to the lowest passenger exposure to the contaminant, while the $\alpha = 30°$ caused the least exposure during the climb leg under aircraft extreme operating conditions. For both legs, however, the 60° airflow supply angle led to the highest passenger exposure. Additionally, and for both flight legs, when a three-dimensional approach was introduced to the airflow redirection scenario through the angle β, directing the airflow to the back of the cabin proved to be better than directing it to the front.

The supply airflow rate to the cabin was changed from a baseline of 200 L s^{-1} to 100% increase, 50% increase, and 50% decrease. For the steady level flight leg, none of the three airflow rate change scenarios provided consistent air quality improvement at the two monitoring locations; seat A7 and seat C7. The 100% more airflow led to reduced peak concentration at seat A7, but, at seat C7 it increased the exposure more than three time the original during the steady flight case. The 50% less airflow led to nearly the same exposure as of that for the steady flight case at the two seats with a tendency of exposure increase near the end of simulation time. Lastly, the 50% more airflow case was only able to reduce the passenger exposure to about 50% of that for the original steady flight case at seat C7, but it increased the exposure more than three-fold its original level at seat A7. Differently, for the climb leg under aircraft extreme operating conditions, the 100% more airflow scenario led to the highest reduction in passenger exposure locally at the two monitoring points preceded by the 50% more flow rate. The 50% less airflow rate was not desirable as it increased exposure. However, cabin-wide, increasing airflow rate by 100% enhanced the contaminant spread as

much as the 50% decrease did. For this reason, and based on energy consumption trade-offs, raising the supply airflow with 50% was found to be the optimal scenario during the climb leg under aircraft extreme operating conditions.

Changing the cough direction was proven effective in reducing the exposure of the passengers to the released contaminant for both steady level flight leg and the climb leg under aircraft extreme operating conditions. This is only the case when the cough was directed downwards either with 30° or 40° from the horizontal direction (or the baseline case with 0°). However, directing the cough upwards contributed to increasing the exposure over that for the baseline case for both steady level flight leg and climb leg under aircraft extreme operating conditions.

Altering the cough release velocity or volumetric flow rate was another source control remedial strategy adopted. For the steady level flight leg, both the variable cough release velocity and the fixed released SF_6 (contaminant) mass approaches were investigated. It was observed that on a local level at the two monitoring points, the higher cough velocity of 20 m s^{-1} led to reduced contaminant concentration and passenger exposure than the original velocity of 10.6 m s^{-1} . Also, the lower cough velocity of 5 m s^{-1} led to less passenger exposure than the higher cough velocity case, but only for limited time after the release of the contaminant. At later time, however, the contaminant concentration for the 5 m s^{-1} cough case surpass that for the 20 m s^{-1} cough case. Nevertheless, cabin-wide, the higher cough velocity of 20 m s^{-1} led to a marginally enhanced air quality condition over the other two cases. Conversely, through fixing the released contaminant mass in the cabin, the produced exposure at the two monitoring locations was unrealistically low as the cough with reduced release time was too weak to overcome the strong airflow currents in the cabin. Therefore, this latter approach was deemed impractical and was not investigated further. On the other hand, during the climb leg under aircraft extreme operating conditions, it was noticed that changing the cough release velocity led to reduced exposure when the velocity was increased from the baseline case of 10 m s^{-1} to 20 m s^{-1} at the two monitoring locations, and led to increased exposure when this baseline cough velocity was decreased to 5 m s^{-1}. On the cabin-wide level, however, the contaminant dispersion behavior did not show a clear trend, and neither of the two cough velocities clearly resulted in a better air quality condition.

As a last strategy in the source control category, and although being not highly practical nor applicable in some cases, moving the patient(s), especially those suffering from highly infectious diseases, can very well reduce the exposure of other healthy passengers in the cabin to the released contaminant, and consequently the probability of them being infected. In the

simulated cases, relocating the coughing person (or the cougher) to other locations in the cabin other than the original back-row-center-seat position had a considerable effect on the dispersion behavior of the contaminant, and consequently, the exposure of other passengers to it. For the steady level flight leg, moving the cougher to the left side of the cabin in the center row (LC location) led to decreased passenger exposure locally at seat C7, but it led to increased exposure at seat A7 after 100 s following the contaminant release from this changed location. Differently, moving the cougher to the right side of the cabin in the front row (RF location) caused a very substantial increase in the exposure at seat A7, as it is very close to it, while it kept the exposure at seat C7 at a low value. On the other hand, during the climb leg under aircraft extreme operating conditions, relocating the cougher the LC location led to decreased passenger exposure both locally at the two monitoring locations, and as an average in the whole cabin. But, similar to the steady flight case, moving the cougher to the RF location increased the exposure of the passenger at seat A7 considerably, while it halved the exposure at the other location at seat C7. For both flight legs, and in addition to the proximity of the cougher to specific passengers, the airflow patterns in the cabin, and the existence of walls and/or surfaces near the cougher all are factors with significant effects on the resulted contaminant dispersion behavior from different cougher locations. Added to those factors, the acceleration-induced body forces on the aircraft can be very influential on the contaminant dispersion behavior during the climb leg under aircraft extreme operating conditions.

For the steady level flight leg, the remedial cases that showed the highest reduction in passenger exposure as an average between the two monitoring locations at seats A7 and C7 with respect to the baseline case are: the 40° downwards cough, the 30° downwards cough, the 5 m s^{-1} cough velocity, and the 20 m s^{-1} cough velocity cases. The exposure ratios are 0.3 : 1 at seat A7 and 0.5 : 1 at seat C7 for the first case, 0.4 : 1 at seat A7 and 0.6 : 1 at seat C7 for the second case, 0.4 : 1 at seat A7 and 0.6 : 1 at seat C7 for the third case, and 0.6 : 1 at seat A7 and 0.5 : 1 at seat C7 for the fourth case, respectively. Conversely, the highest exposure in average between the two seats belongs to the right side-front row cougher relocation case with 36.6 : 1 at seat A7 and 0.7 : 1 at seat C7. On the other hand, for the climb leg under aircraft extreme operating conditions, the most efficient remedial cases are: the left-side, center-row relocation of the cougher, the $\alpha = 30°$ airflow direction, and the 50% more airflow rate. The exposure ratios are 0.7 : 1 at seat A7 and 0.5 : 1 at seat C7 for the first case, 0.7 : 1 at seat A7 and 0.5 : 1 at seat C7 for the second case, and 0.6 : 1 at seat A7 and 0.7 : 1 at seat C7 for the third case, respectively. However, the highest exposure

ratio for a remedial case during the climb leg under aircraft extreme operating conditions is for the $\alpha = 60^{\circ}$ airflow direction case with 3.5 : 1 at seat A7 and 2.1 : 1 at seat C7.

9.1.4 Cough-released Particles Dispersion behavior in the Cabin

Particles of different sizes were injected in the cabin to represent the expiratory contaminant released from the cough instead of the SF_6 gas. Three particle diameters have been used, namely: 2.5 µm representing the fine airborne particles, and 7.5 and 10 µm for the coarse particles. The 7.5 µm particles showed a dissimilar dispersion behavior to the one noticed for the 2.5 and 10 µm particles. They could stay for long time in the cabin without settling and/or depositing on surfaces, or being discharged from the cabin space. The residence time for the 7.5 m particles was not affected by the change in the acceleration-induced body forces between the climb leg under aircraft extreme operating conditions and the steady level flight leg. Consequently, the expiratory airborne particles of intermediate size (around 7.5 µm in diameter) can pose the greatest infection risk on the passengers throughout most of the flight duration.

9.1.5 Merits and Limitations of the Current Study

Finally, the current study provides a straightforward approach to studying passenger aircraft ventilation performance and expiratory contaminant dispersion during different flight legs and under the influence of acceleration-induced body forces using numerical means. This is to avoid the complicated and expensive experimental investigations required for this type of research. However, there are some implications for the study that the reader must be aware of. The current investigation is generally a preliminary concept study and not an exact one. SF_6 was used to mimic cough particles of the smallest size range which adds some inaccuracy. However, the dispersion behavior of fine and coarse particles, which are expected to be released from expiratory events, such as coughing, was investigated to complement the findings attained using the SF_6 gaseous surrogate. Also, the results of the study cannot be exactly generalized on all passenger aircraft because a specific aircraft model and design (Boeing 767-300) was used. Moreover, only a section of the economy cabin was considered for investigation and not the full aircraft fuselage.

9.2 Further Research Gaps and Future Research Topics

9.2.1 Determination of Contaminant Levels and Properties in Aircraft Cabins

Some of the studies that measured the concentrations of gaseous contaminants (real or surrogates) in aircraft cabin environments used portable and hand-held air or gas samplers and photometers [12, 43, 106] with limited accuracy and deficiency in determining a wide range of concentrations in large spaces. Alternatively, a fixed set of sensors or well-implemented sampling lines are more desirable for eliminating human errors in sampling. Some researchers used the fixed-sensor (sampling tree) approach for quantifying gas concentrations inside aircraft cabins through a Data Acquisition (DAQ) system [8, 81, 92, 101]. For future studies, and to attain as much concentration measurement accuracy as possible, gas sampling trees can be employed with higher resolution and better sensor positioning in the cabin space.

Another side to consider is the need for more detailed studies on the dispersion and deposition characteristics of some harmful gaseous compounds, such as disinsection pesticides, which are very common aboard many airliners nowadays. The inhalation of pesticides by passengers may pose health risks that are overlooked in the literature and could be worthy of investigation.

For particulate contaminants aboard aircrafts, and especially those generated from expiratory events, more emphasis can be directed towards conducting on-board live tests for the viability and infectivity of the micro-organisms contained in the droplets.

9.2.2 Aircraft Ventilation Strategies

Personalized Ventilation (PV) systems provided the most promising results for air quality enhancement and cross-infection mitigation in aircraft cabins [36, 105–107]. Therefore, more research effort should still be placed on the potential of the personalized ventilation systems in preventing harmful contaminants from reaching the occupants, and in containing infectious particles in the microenvironment of the infecting person. Such actions can be called shielding effects. For example, the shielding effects of the personalized ventilation can be investigated through new, but realistic, configurations for cabin seats with air inlets near the faces of the occupants, or modified arrangements (ergonomics) of overhead gaspers that can increase

their protection effectiveness.

With the development of new aircraft models and designs, such as the double-decker and multi-deck aircrafts, investigation of the employed ventilation strategies aboard those novel airliners and the resulting airflow patterns in each deck's cabin is required. Such a new research direction can pave the way for multi-cabin contaminant dispersion studies in the near future.

9.2.3 Suggested Air Quality Research Approaches in Aircrafts

Using culture methods, such as culture dishes, the viability and infectivity of airborne pathogens can be measured aboard airliners. The use of culture dishes or media plates (e.g. agar gel plates) to collect samples of airborne pathogens during flights, and allowing them to incubate, or grow, in the cabin temperature, relative humidity, and air composition conditions can provide more accurate indication of the true airborne infection risk in cabins. Despite this, laboratory techniques, such as Polymerase Chain Reaction (PCR) and plaque assay methods [6] can still be used to complement and verify the results from the culture methods aboard aircraft.

For the numerical simulation techniques of airflow and contaminant transport, the use of custom wall functions, either through modifying existing functions or considering new laws for the wall, can provide more accurate numerical predictions. Another suggestion is the application of alternative transport models to the common Navier-Stokes equations. One example is the Lattice-Boltzmann Method (LBM), which is based on complex fluid flow fields on microscopic collision models and mesoscopic equations instead of the familiar continuum-based Navier-Stokes model [17]. LBM has been successfully used in literature for simulating a wide range of complex flows, either bounded flows [32], or unbounded atmospheric and urban flow fields [18]. Moreover, LBM models have been shown to run faster than Navier-Stokes models using parallel computations.

Additional parametric variations of the variables included in the study, such as increasing the frequency of injections, and/or varying the number of concentration monitoring sites and their locations were beyond the scope of the current study. Those factors may have some impact on the difference in the passengers' exposure to contaminants between the steady level flight, and the climb and descent legs under aircraft normal and extreme operating conditions and necessitate further investigations.

Moreover, the effect of the acceleration-induced body forces on particle dispersion in the

passenger aircraft cabins is another necessary topic to expand upon in follow-up studies. Also, larger and more modern aircraft cabin models with different configurations can be utilized to generalize the findings of the current study.

For the descent leg, however, the impact of practical future plans such as the one proposed by the European Organization for the Safety of Air Navigation (EUROCONTROL) in 2011 to implement a Continuous Descent Approach (CDA) instead of the conventional staged descent approach can be studied. The CDA is sought to eliminate the extended low-level thrust segments currently performed in the middle of the descent stages. In addition to controlling contaminants dispersion inside the cabin, CDA may also help in offsetting the harmful effects of passenger aircraft noise and atmospheric emissions [30].

Finally, further combinations and/or additions to the proposed airflow design and source control strategies in Chapters 5 and 7 of the current thesis can be investigated for possible enhancements in the in-cabin air quality. This work warrants the need for multiple detailed investigations related to the influence of aircraft acceleration-induced body forces on the ventilation performance and the in-cabin air quality of passenger aircraft, especially during extreme or non-traditional aircraft operating conditions, a topic that has been neglected in the literature for a long time.

References

[1] Air Transport Action Group. Facts & Figures. Air Transport Action Group, Geneva, Switzerland: [https://www.atag.org/facts-figures.html]. Accessed (2019-02-21), 2019.

[2] Aliabadi, A. A. *Dispersion of Expiratory Airborne Droplets in a Model Single Patient Hospital Recovery Room with Stratified Ventilation.* Ph.D. thesis, The University of British Columbia, Vancouver, Canada, 2013.

[3] Aliabadi, A. A. *Theory and Applications of Turbulence: A Fundamental Approach for Scientists and Engineers.* Amir Abbas Aliabadi Publications, Guelph, ON, Canada, 2018.

[4] Aliabadi, A. A., Faghani, E., Tjong, H. A. R., and Green, S. I. Hybrid Ventilation Design for a Dining Hall Using Computational Fluid Dynamics (CFD). In *Proceedings of The Canadian Society for Mechanical Engineering (CSME) International Congress* (2014), pp. 1–6.

[5] Aliabadi, A. A., Krayenhoff, E. S., Nazarian, N., Chew, L. W., Armstrong, P. R., Afshari, A., and Norford, L. K. Effects of Roof-Edge Roughness on Air Temperature and Pollutant Concentration in Urban Canyons. *Boundary-Layer Meteorology 164*, 2 (2017), 249–279.

[6] Aliabadi, A. A., Rogak, S. N., Bartlett, K. H., and Green, S. I. Preventing Airborne Disease Transmission: Review of Methods for Ventilation Design in Health Care Facilities. *Advances in Preventive Medicine 2011* (2011), 1–21.

[7] Aliabadi, A. A., Veriotes, N., and Pedro, G. A Very Large-Eddy Simulation (VLES) model for the investigation of the neutral atmospheric boundary layer. *Journal of Wind Engineering and Industrial Aerodynamics 183* (2018), 152–171.

[8] Anderson, M. D. *Effect of Gaspers on Airflow Patterns and the Transmission of Airborne Contaminants within an Aircraft Cabin Environment.* M.Sc. thesis, Kansas State University, 2012.

[9] ANSYS Inc. *ANSYS Fluent Theory Guide: Release 16.2.* SAS IP, Inc., Canonsburg, Pennsylvania, U.S.A., 2015.

[10] ASHRAE. *Standard 161-2013: Air Quality within Commercial Aircraft*. American Society of Heating, Refrigerating and Air-Conditioning Engineers, Atlanta, GA, USA, 2013.

[11] ASHRAE. *Position Document on Airborne Infectious Diseases*. American Society of Heating, Refrigerating and Air-Conditioning Engineers, Atlanta, GA, USA, 2014.

[12] Bhangar, S., Cowlin, S. C., Singer, B. C., Sextro, R. G., and Nazaroff, W. W. Ozone Levels in Passenger Cabins of Commercial Aircraft on North American and Transoceanic Routes. *Environmental Science and Technology 42*, 11 (2008), 3938–3943.

[13] Blocken, B., Stathopoulos, T., and Carmeliet, J. CFD simulation of the atmospheric boundary layer: wall function problems. *Atmospheric Environment 41*, 2 (2007), 238–252.

[14] Bosbach, J., Pennecot, J., Wagner, C., Raffel, M., Lerche, T., and Repp, S. Experimental and numerical simulations of turbulent ventilation in aircraft cabins. *Energy 31*, 5 (2006), 694–705.

[15] Chang, J. C., and Hanna, S. R. Air quality model performance evaluation. *Meteorology and Atmospheric Physics 87*, 1-3 (2004), 167–196.

[16] Chen, Q. Comparison oF Different k-ϵ Models for Indoor Air Flow Computations. *Numerical Heat Transfer, Part B: Fundamentals 28*, 3 (1995), 353–369.

[17] Chen, S., and Doolen, G. D. Lattice Boltzmann Method for Fluid Flows. *Annual Review of Fluid Mechanics 30:329–64 30*, 1 (1998), 329–64.

[18] Chen, T. *Development of Designer-Relevant Lattice-Boltzmann Wind Field Model for Urban Canyons and Their Neighborhoods*. M.Sc. thesis, Massachusetts Institute of Technology, 2016.

[19] Chen, W., Liu, J., Li, F., Cao, X., Li, J., Zhu, X., and Chen, Q. Ventilation similarity of an aircraft cabin mockup with a real MD-82 commercial airliner. *Building and Environment 111* (2017), 80–90.

[20] Cheng, H.-P., Cheng, J.-R., and Yeh, G.-T. A Particle Tracking Technique for the Lagrangian-Eulerian Finite Element Method in Multi-Dimensions. *International Journal for Numerical Methods in Engineering 39*, 7 (1996), 1115–1136.

[21] Conceição, S. T., Pereira, M. L., and Tribess, A. A Review of Methods Applied to Study Airborne Biocontaminants Inside Aircraft Cabins. *International Journal of Aerospace Engineering 2011* (2011).

[22] Dai, S., Sun, H., Liu, W., Guo, Y., Jiang, N., and Liu, J. Experimental study on characteristics of the jet flow from an aircraft gasper. *Building and Environment 93*, P2 (2015), 278–284.

[23] Dechow, M., Sohn, H., and Steinhanses, J. Concentrations of Selected Contaminants in Cabin Air of Airbus Aircrafts. *Chemosphere 35* (1997), 21–31.

[24] Dimou, K. *3-D Hybrid Eulerian-Lagrangian / Particle Tracking Model for Simulating Mass Transport in Coastal Water Bodies*. Ph.D. thesis, Massachusetts Institute of Technology, 1992.

[25] Drake, J. W., and Johnson, D. E. Measurements of certain environmental tobacco smoke components on long-range flights. *Aviation, Space, and Environmental Medicine 61*, 6 (1990), 531–542.

[26] Duguid, J. P. The Size and the Duration of Air-Carriage of Respiratory Droplets and Droplet-Nuclei. *The Journal of Hygiene 44*, 6 (1946), 471–479.

[27] Dygert, R. K., and Dang, T. Q. Mitigation of cross-contamination in an aircraft cabin via localized exhaust. *Building and Environment 45*, 9 (2010), 2015–2026.

[28] Elmaghraby, H. A., Chiang, Y. W., and Aliabadi, A. A. Ventilation strategies and air quality management in passenger aircraft cabins: A review of experimental approaches and numerical simulations. *Science and Technology for the Built Environment 24*, 2 (2018), 160–175.

[29] Elmaghraby, H. A., Chiang, Y. W., and Aliabadi, A. A. Are Aircraft Acceleration-induced Body Forces Effective on Contaminant Dispersion in Passenger Aircraft Cabins? *Science and Technology for the Built Environment 25*, 7 (2019), 858–872.

[30] EUROCONTROL. *Continuous Descent: A Guide to Implementing Continuous Descent (Brochure)*. EUROCONTROL, Brussels, Belgium (BE), 2011.

[31] Fairchild, C. I., and Stampfer, J. F. Particle Concentration in Exhaled Breath - Summary Report. *American Industrial Hygiene Association Journal 48*, 11 (1987), 948–949.

[32] Fakhari, A., and Lee, T. Numerics of the lattice boltzmann method on nonuniform grids: Standard LBM and finite-difference LBM. *Computers and Fluids 107* (2015), 205–213.

[33] Fang, Z., Liu, H., Li, B., Baldwin, A., Wang, J., and Xia, K. Experimental investigation of personal air supply nozzle use in aircraft cabins. *Applied Ergonomics 47* (2015), 193–202.

[34] Faulkner, W. B., Memarzadeh, F., Riskowski, G., Kalbasi, A., and Ching-Zu Chang, A. Effects of air exchange rate, particle size and injection place on particle concentrations within a reduced-scale room. *Building and Environment 92* (2015), 246–255.

[35] Gao, N., and Niu, J. Transient CFD simulation of the respiration process and inter-person exposure assessment. *Building and Environment 41*, 9 (2006), 1214–1222.

[36] Gao, N. P., and Niu, J. L. Personalized Ventilation for Commercial Aircraft Cabins. *Journal of Aircraft 45*, 2 (2008), 508–512.

[37] Garner, R. P., Wong, K. L., Ericson, S. C., Baker, a. J., and Orzechowski, J. a. CFD Validation for Contaminant Transport in Aircraft Cabin Ventilation Flow Fields. Tech. rep., Office of Aerospace Medicine, U.S. Department of Transportation, Federal Aviation Administration, Washington, DC, 2004.

[38] Günther, G., Bosbach, J., Pennecot, J., Wagner, C., Lerche, T., and Gores, I. Experimental and numerical simulations of idealized aircraft cabin flows. *Aerospace Science and Technology 10*, 7 (2006), 563–573.

[39] Gupta, J. K., Lin, C.-H., and Chen, Q. Flow dynamics and characterization of a cough. *Indoor Air 19*, 6 (2009), 517–525.

[40] Gupta, J. K., Lin, C.-H., and Chen, Q. Inhalation of expiratory droplets in aircraft cabins. *Indoor Air 21*, 4 (2011a), 341–350.

[41] Gupta, J. K., Lin, C.-H., and Chen, Q. Transport of expiratory droplets in an aircraft cabin. *Indoor Air 21*, 4 (2011b), 3–11.

[42] Gupta, J. K., Lin, C.-H., and Chen, Q. Risk assessment of airborne infectious diseases in aircraft cabins. *Indoor Air 22*, 5 (2012), 388–395.

[43] Haghighat, F., Allard, F., Megri, A. C., Blondeau, P., and Shimotakahara, R. Measurement of Thermal Comfort and Indoor Air Quality Aboard 43 Flights on Commercial Airlines. *Indoor and Built Environment 8*, 1 (1999), 58–66.

[44] Hanna, S., and Chang, J. Acceptance criteria for urban dispersion model evaluation. *Meteorology and Atmospheric Physics 116*, 3-4 (2012), 133–146.

[45] Hanna, S. R. Confidence Limits for Air Quality Model Evaluations, As Estimated by Bootstrap and Jackknife Resampling Methods. *Atmospheric Environment 23*, 6 (1989), 1385–1398.

[46] Hassan, M. Numerical Investigation of Improving Distribution Systems In Aircraft Passengers Cabins. M.Sc. thesis, Faculty of Engineering, Cairo University, Giza, Egypt, 2016.

[47] Hull, D. G. *Fundamentals of Airplane Flight Mechanics*. Springer Berlin Heidelberg, New York, 2007.

[48] Isukapalli, S. S., Mazumdar, S., George, P., Wei, B., Jones, B., and Weisel, C. P. Computational fluid dynamics modeling of transport and deposition of pesticides in an aircraft cabin. *Atmospheric Environment 68* (2013), 198–207.

[49] Kühn, M., Bosbach, J., and Wagner, C. Experimental parametric study of forced and mixed convection in a passenger aircraft cabin mock-up. *Building and Environment 44*, 5 (2009), 961–970.

[50] Lai, A. C. K., and Cheng, Y. C. Study of expiratory droplet dispersion and transport using a new Eulerian modeling approach. *Atmospheric Environment 41*, 35 (2007), 7473–7484.

[51] Launder, B., and Spalding, D. The Numerical Computation of Turbulent Flows. *Computer Methods in Applied Mechanics and Engineering 3*, 2 (1974), 269–289.

[52] Li, B., Duan, R., Li, J., Huang, Y., Yin, H., Lin, C.-H., Wei, D., Shen, X., Liu, J., and Chen, Q. Experimental studies of thermal envi ronment and contaminant transport in a commercial aircraft cabin with gaspers on. *Indoor Air* (2015), 1–14.

[53] Li, F., Liu, J., Pei, J., Lin, C. H., and Chen, Q. Experimental study of gaseous and particulate contaminants distribution in an aircraft cabin. *Atmospheric Environment 85* (2014), 223–233.

[54] Li, F., Liu, J., Ren, J., Cao, X., and Zhu, Y. Numerical investigation of airborne contaminant transport under different vortex structures in the aircraft cabin. *International Journal of Heat and Mass Transfer 96* (2016), 287–295.

[55] Li, X. X., Britter, R. E., Koh, T. Y., Norford, L. K., Liu, C. H., Entekhabi, D., and Leung, D. Y. Large-eddy simulation of flow and pollutant transport in urban street canyons with ground heating. *Boundary-Layer Meteorology 137*, 2 (2010), 187–204.

[56] Li, X. X., Britter, R. E., Norford, L. K., Koh, T. Y., and Entekhabi, D. Flow and pollutant transport in urban street canyons of different aspect ratios with ground heating: large-eddy simulation. *Boundary-Layer Meteorology 142*, 2 (2012), 289–304.

[57] Li, X. X., Leung, D. Y., Liu, C. H., and Lam, K. M. Physical modeling of flow field inside urban street canyons. *Journal of Applied Meteorology and Climatology 47*, 7 (2008), 2058–2067.

[58] Lin, Z., Chow, T. T., Fong, K. F., Wang, Q., and Li, Y. Comparison of performances of displacement and mixing ventilations. Part I : thermal comfort. *International Journal of Refrigeration 28* (2005), 276–287.

[59] Liu, S., Xu, L., Chao, J., Shen, C., Liu, J., Sun, H., Xiao, X., and Nan, G. Thermal environment around passengers in an aircraft cabin. *HVAC&R Research 19*, 5 (2013), 627–634.

[60] Liu, W., Mazumdar, S., Zhang, Z., Poussou, S. B., Liu, J., Lin, C. H., and Chen, Q. State-of-the-art methods for studying air distributions in commercial airliner cabins. *Building and Environment 47*, 1 (2012), 5–12.

[61] Liu, W., Wen, J., Chao, J., Yin, W., Shen, C., Lai, D., Lin, C. H., Liu, J., Sun, H., and Chen, Q. Accurate and high-resolution boundary conditions and flow fields in the first-class cabin of an MD-82 commercial airliner. *Atmospheric Environment 56* (2012), 33–44.

[62] Liu, W., Wen, J., Lin, C. H., Liu, J., Long, Z., and Chen, Q. Evaluation of various categories of turbulence models for predicting air distribution in an airliner cabin. *Building and Environment 65* (2013), 118–131.

[63] Loudon, R. G., and Roberts, R. M. Relation Between the Airborne Diameters of Respiratory Droplets and the Diameter of the Stains Left After Recovery. *Nature* (1967), 95–96.

[64] Mangili, A., and Gendreau, M. A. Transmission of infections during commercial air travel. *Lancet 365*, 9478 (2005), 2176–2177.

[65] Melikov, A. K. Personalized Ventilation. *Indoor Air 14*, Suppl 7 (Jan 2004), 157–67.

[66] Memarzadeh, F. Effect of reducing ventilation rate on indoor air quality and energy cost in laboratories. *Journal of Chemical Health and Safety 16*, 5 (2009), 20–26.

[67] Milton, D. K., Fabian, M. P., Cowling, B. J., Grantham, M. L., and McDevitt, J. J. Influenza virus aerosols in human exhaled breath: Particle size, culturability, and effect of surgical masks. *PLoS Pathogens 9*, 3 (mar 2013), e1003205.

[68] National Aeronautics and Space Administration (NASA). Forces in a climb. [https://www.grc.nasa.gov/www/k-12/airplane/climb.html]. Accessed (2017-10-10), 2015.

[69] Nazarian, N., and Kleissl, J. Realistic solar heating in urban areas: Air exchange and street-canyon ventilation. *Building and Environment 95* (2016), 75–93.

[70] Nicas, M., Nazaroff, W. W., and Hubbard, A. Toward Understanding the Risk of Secondary Airborne Infection: Emission of Respirable Pathogens. *Journal of Occupational and Environmental Hygiene 2*, 3 (2005), 143–54.

[71] Nielsen, P. V. Predictions of air distribution in a forced ventilation room. *Ingeniarens Ugebtad 5* (1973).

[72] Nijdam, J. J., Langrish, T. A. G., and Fletcher, D. F. Assessment of an Eulerian CFD model for prediction of dilute droplet dispersion in a turbulent jet. *Applied Mathematical Modelling 32*, 12 (2008), 2686–2705.

[73] NOAA. NOAA AMDAR Data Display. National Oceanic and Atmospheric Administration - U.S. Department of Commerce. [https://amdar.noaa.gov/demo_java/]. Accessed (2019-05-10), 2019.

[74] Olsen, S., Chang, H., Cheung, T., Tang, A., Fisk, T., Ooi, S., Kuo, H., Jiang, D., Chen, K., Lando, J., and Hsu, K. Transmission of the Severe Acute Respiratory Syndrome on Aircraft. *New England Journal of Medicine 349*, 25 (2003), 2416–2422.

[75] Papineni, R. S., and Rosenthal, F. S. The Size Distribution of Droplets in the Exhaled Breath of Healthy Human Subjects. *Journal of Aerosol Medicine: the official journal of the International Society for Aerosols in Medicine 10*, 2 (1997), 105–116.

[76] Poussou, S. B., Mazumdar, S., Plesniak, M. W., Sojka, P. E., and Chen, Q. Flow and contaminant transport in an airliner cabin induced by a moving body: Model experiments and CFD predictions. *Atmospheric Environment 44*, 24 (2010), 2830–2839.

[77] Roache, P. J. Perspective: A Method for Uniform Reporting of Grid Refinement Studies. *Journal of Fluids Engineering 116*, 3 (1994), 405–413.

[78] Roache, P. J. Quantification of Uncertainty in Computational Fluid Dynamics. *Annual Review of Fluid Mechanics 29* (1997), 129–160.

[79] Rydock, J. P. Tracer Study of Proximity and Recirculation Effects on Exposure Risk in an Airliner Cabin. *Aviation Space and Environmental Medicine 75*, 2 (2004), 168–171.

[80] Spalart, P. R. Philosophies and fallacies in turbulence modeling. *Progress in Aerospace Sciences 74* (2015), 1–15.

[81] Strøm-Tejsen, P., Wyon, D. P., Lagercrantz, L., and Fang, L. Passenger evaluation of the optimum balance between fresh air supply and humidity from 7-h exposures in a simulated aircraft cabin. *Indoor Air 17*, 2 (2007), 92–108.

[82] Sze To, G. N., Wan, M. P., Chao, C. Y. H., Fang, L., and Melikov, A. Experimental Study of Dispersion and Deposition of Expiratory Aerosols in Aircraft Cabins and Impact on Infectious Disease Transmission. *Aerosol Science and Technology 43*, 5 (2009), 466–485.

[83] Tang, J. W., Nicolle, A. D., Klettner, C. a., Pantelic, J., Wang, L., Suhaimi, A. B., Tan, A. Y. L., Ong, G. W. X., Su, R., Sekhar, C., Cheong, D. D. W., and Tham, K. W. Airflow dynamics of human jets: sneezing and breathing - potential sources of infectious aerosols. *PloS one 8*, 4 (2013), e59970.

[84] Tellier, R. Review of Aerosol Transmission of Influenza A Virus. *Emerging Infectious Diseases 12*, 11 (2006), 1657–1662.

[85] Tellier, R. Aerosol transmission of influenza A virus: a review of new studies. *Journal of the Royal Society Interface 6* (2009), S783–S790.

[86] U.S. Federal Aviation Administration. *Advisory Circular*. (U.S. Government Publishing Office, Ed.) *AC 120–38: Transport Category Airplanes Cabin Ozone Concentrations*. U.S. Department of Transportation, Washington, DC, U.S.A., Washington, DC, 1980.

[87] U.S. Federal Aviation Administration (FAA). *Pilot's Handbook of Aeronautical Knowledge*. U.S. Department of Transportation, Washington, DC, U.S.A., 2016.

[88] USDOT. Aircraft Disinsection Requirements. U.S. Department of Transportation (USDOT), Washington, DC, U.S.A. [https://www.transportation.gov/airconsumer /spray]. Accessed (12-02-2017), 2017.

[89] Wagner, B. G., Coburn, B. J., and Blower, S. Calculating the potential for within-flight transmission of influenza A (H1N1). *BMC Medicine 7*, 1 (2009), 81.

[90] Wan, M. P., Chao, C. Y. H., and Fang, L. Transmission characteristics of passenger-exhaled droplets in a simulated air-cabin environment. In *Proceedings of the 10th International Conference on Indoor Air Quality and Climate* (2005), pp. 2598–2602.

[91] Wan, M. P., Sze To, G. N., Chao, C. Y. H., Fang, L., and Melikov, A. Modeling the Fate of Expiratory Aerosols and the Associated Infection Risk in an Aircraft Cabin Environment. *Aerosol Science and Technology 43*, 4 (2009), 322–343.

[92] Wang, A., Zhang, Y., Sun, Y., and Wang, X. Experimental study of ventilation effectiveness and air velocity distribution in an aircraft cabin mockup. *Building and Environment 43*, 3 (2008), 337–343.

[93] Wang, M., and Chen, Q. Assessment of Various Turbulence Models for Transitional Flows in Enclosed Environment (RP-1271). *HVAC&R Research 15*, 6 (2009), 1099–1119.

[94] Waters, M. A., Bloom, T. F., Grajewski, B., and Deddens, J. Measurements of Indoor Air Quality on Commercial Transport Aircraft. In *The 9th International Conference on Indoor Air Quality and Climate, Monterey, CA, U.S.A., June 30-July 5* (2002), pp. 782–787.

[95] Weber, T. P., and Stilianakis, N. I. Inactivation of influenza A viruses in the environment and modes of transmission: A critical review. *Journal of Infection 57*, 5 (2008), 361–373.

[96] Wells, W. F. On Air-Borne Infection. Study II. Droplets and Droplet Nuclei. *American Journal of Hygiene 20* (1934), 611–618.

[97] Wells, W. F., and Stone, W. R. On Air-Borne Infection. Study III. Viability of Droplet Nuclei Infection. *American Journal of Hygiene 20* (1934), 619–627.

[98] Wisthaler, A., Strøm-Tejsen, P., Fang, L., Arnaud, T. J., Hansel, A., Mark, T. D., and Wyon, D. P. PTR-MS Assessment of Photocatalytic and Sorption-Based Purification of Recirculated Cabin Air During Simulated 7-h Flights with High Passenger Density. *Environmental Science and Technology 41*, 1 (2007), 229–234.

[99] Wisthaler, A., Tamás, G., Wyon, D. P., Strøm-Tejsen, P., Space, D., Beauchamp, J., Hansel, A., Märk, T. D., and Weschler, C. J. Products of Ozone-Initiated Chemistry in a Simulated Aircraft Environment. *Environmental Science and Technology 39*, 13 (2005), 4823–4832.

[100] Yan, J., Grantham, M., Pantelic, J., de Mesquita, P. J. B., Albert, B., Liu, F., Ehrman, S., and and, D. K. M. Infectious virus in exhaled breath of symptomatic seasonal influenza cases from a college community. *Proceedings of the National Academy of Sciences 115*, 5 (Jan 2018), 1081–1086.

[101] Yan, W., Zhang, Y., Sun, Y., and Li, D. Experimental and CFD study of unsteady airborne pollutant transport within an aircraft cabin mock-up. *Building and Environment 44*, 1 (2009), 34–43.

[102] You, R., Chen, J., Shi, Z., Liu, W., Lin, C.-H., Wei, D., and Chen, Q. Experimental and numerical study of airflow distribution in an aircraft cabin mock up with a gasper on. *Journal of Building Performance Simulation 9*, 5 (2016), 555–566.

[103] Zhai, S., Li, Z., and Zhao, B. State-space analysis of influencing factors on airborne particle concentration in aircraft cabins. *Building and Environment 74* (2014), 13–21.

[104] Zhai, Z. J., Zhang, Z., Zhang, W., and Chen, Q. Y. Evaluation of Various Turbulence Models in Predicting Airflow and Turbulence in Enclosed Environments by CFD: Part 1—Summary of Prevalent Turbulence Models. *HVAC&R Research 13*, 6 (2007), 853–870.

[105] Zhang, T., and Chen, Q. Novel air distribution systems for commercial aircraft cabins. *Building and Environment 42*, 4 (2007), 1675–1684.

[106] Zhang, T. T., Li, P., and Wang, S. A personal air distribution system with air terminals embedded in chair armrests on commercial airplanes. *Building and Environment 47*, 1 (2012), 89–99.

[107] Zhang, T. T., Li, P., Zhao, Y., and Wang, S. Various air distribution modes on commercial airplanes. Part 1: Experimental measurement. *HVAC&R Research 9*, 3 (2013), 268–282.

[108] Zhang, T. T., Yin, S., and Wang, S. An under-aisle air distribution system facilitating humidification of commercial aircraft cabins. *Building and Environment 45*, 4 (2010), 907–915.

[109] Zhang, Y., Li, D., Lin, Z., Santanello, J. A., and Gao, Z. Development and Evaluation of a Long-Term Data Record of Planetary Boundary Layer Profiles From Aircraft Meteorological Reports. *Journal of Geophysical Research: Atmospheres 124*, 4 (2019), 2008–2030.

[110] Zhang, Z., and Chen, Q. Comparison of the Eulerian and Lagrangian methods for predicting particle transport in enclosed spaces. *Atmospheric Environment 41*, 25 (2007), 5236–5248.

[111] Zhang, Z., Chen, X., Mazumdar, S., Zhang, T., and Chen, Q. Experimental and numerical investigation of airflow and contaminant transport in an airliner cabin mockup. *Building and Environment 44*, 1 (2009), 85–94.

[112] Zhang, Z., Zhang, W., Zhai, Z. J., and Chen, Q. Y. Evaluation of Various Turbulence Models in Predicting Airflow and Turbulence in Enclosed Environments by CFD: Part 2—Comparison with Experimental Data from Literature. *HVAC&R Research 13*, 6 (2007), 871–886.

[113] Zhao, B., Yang, C., Yang, X., and Liu, S. Particle dispersion and deposition in ventilated rooms: Testing and evaluation of different Eulerian and Lagrangian models. *Building and Environment 43*, 4 (2008), 388–397.

[114] Zhao, B., Zhang, Z., and Li, X. Numerical study of the transport of droplets or particles generated by respiratory system indoors. *Building and Environment 40*, 8 (2005), 1032–1039.

[115] Zhu, S., Kato, S., and Yang, J.-H. Study on transport characteristics of saliva droplets produced by coughing in a calm indoor environment. *Building and Environment 41*, 12 (dec 2006), 1691–1702.

[116] Zítek, P., Vyhlídal, T., Simeunović, G., Nováková, L., and Čížek, J. Novel personalized and humidified air supply for airliner passengers. *Building and Environment 45*, 11 (2010), 2345–2353.

Appendix A

Python Codes

A.1 Area under Curve

The Python code shown on the next page is an example for the codes used for calculating the area under the concentration time series curves at the two monitoring locations (seat A7 and seat C7) for different cases by applying equation 5.2. The composite trapezoidal rule and the composite Simpson's rule were used to perform the integration.

The example code is used for calculating the area under the concentration time series curves for the airflow remedial strategy case in which the airflow was supplied with angle $\alpha = 30°$.

```
from __future__ import print_function
import numpy as np
from scipy.integrate import simps
from numpy import trapz

# Seat A7 #
# The y values. A numpy array is used here,
#  but a python list could also be used.
y1 = np.array([0, 0, 0.006872516, 0.150823817, 0.155448478, 0.125286926, 0.124628149,
               0.132241702, 0.148689713, 0.201357916, 0.216176091, 0.243673597, 0.235999577,
               0.238163921, 0.233916205, 0.224678262, 0.218865654, 0.208476669, 0.18716673,
               0.177113722, 0.159329362, 0.148342752, 0.132157826, 0.120240327, 0.110657316,
               0.094280377, 0.090346044, 0.081802669, 0.07194012, 0.062978408, 0.057390588,
               0.052208554, 0.044433974, 0.044636879, 0.038397418])

# Compute the area using the composite trapezoidal rule.
area = trapz(y1, dx=10)
print("A7_area_trapez=", area)

# Compute the area using the composite Simpson's rule.
area = simps(y1, dx=10)
print("A7_area_Simps=", area)

# Seat C7 #
y2 = np.array([0, 0.006808736, 0.331117979, 0.447947407, 0.63698172, 0.703127772,
               0.732281584, 0.609506643, 0.536259139, 0.498620731, 0.508492672,
               0.454891783, 0.443363422, 0.417797554, 0.39113985, 0.355212459,
               0.312414968, 0.289666837, 0.254873735, 0.228826378, 0.203914578,
               0.176242888, 0.152382828, 0.136661719, 0.117429411, 0.105717946,
               0.097702981, 0.083859114, 0.073617899, 0.068900672, 0.061056122,
               0.054131107, 0.049315416, 0.044151112, 0.039756915])

# Compute the area using the composite trapezoidal rule.
area = trapz(y2, dx=10)
print("C7_area_trapez=", area)

# Compute the area using the composite Simpson's rule.
area = simps(y2, dx=10)
print("C7_area_Simps=", area)
```

A.2 Calculation of Acceleration Components

The Python code used for calculating the passenger aircraft acceleration components under normal operating conditions is shown on the next page. The code reads the climb or descent flight log files one by one and converts the flight time, and latitude and longitude coordinates into sequential data set. Second order curve fitting is then done for this data set using equation 6.1, and plots for the data points and the fitting curve are generated. Lastly, the vertical and horizontal acceleration components are derived from the constants for the used curve-fitting model.

```
import random
import sys
import os
import glob
import numpy as np
import matplotlib.pyplot as plt
import matplotlib.dates as mdates
import datetime
import pandas as pd
from scipy.optimize import curve_fit
from sklearn.metrics import r2_score
from math import sin, cos, asin, sqrt

##############################################################################

#Define file names

fileName = "Climb1.txt"

##############################################################################

# Load all data in matrices
accel = np.loadtxt(fileName, usecols=[0,1,2,3,4])

hour=accel[:,0]
minute=accel[:,1]
lat=accel[:,2]*(3.141593/180)    # Latitude in radians
lon=accel[:,3]*(3.141593/180)    # Longitude in radians
altitude=accel[:,4]

N_accel=np.size(hour)

# Calculating time and horizontal distance travelled (using the haversine formula) from the
    beginning
sec_start=np.zeros(N_accel)

for i in range(1,N_accel):
    sec_start[i] = (minute[i]-minute[0])*60.0
    if sec_start[i] == 0:
        sec_start[i] = 60.0

hor_start=np.zeros(N_accel)

for j in range(1,N_accel):
    hor_start[j] = (2*6371000*asin((sqrt(((sin((lat[j]-lat[0])/2))**2)+(cos(lat[0])*cos(lat[
        j]))*
                    ((sin((lon[j]-lon[0])/2))**2)))))

# Defining the time and altitude\horizontal distance vectors
t = sec_start      # Time vector (s)
zm = altitude      # Altitude vector (ft)
dm = hor_start     # Horizontal distance vector (m)
```

```
# calculate polynomial
pf_alt = np.polyfit(t, zm, 2)
f_alt = np.poly1d(pf_alt)

pf_hor = np.polyfit(t, dm, 2)
f_hor = np.poly1d(pf_hor)

# calculate new t's, zm's, and dm's
t_new = np.linspace(min(t), max(t), 50)
zm_new = f_alt(t_new)
dm_new = f_hor(t_new)

plt.plot(t,zm/3280.84,'o', t_new, zm_new/3280.84)
plt.xlim([t[0]-1, t[-1] + 1])
plt.title('Altitude Data Regression for Vertical Acceleration')
plt.ylabel('Altitude(km)')
plt.xlabel('Time(s)')
plt.show()

plt.plot(t,dm/1000,'o', t_new, dm_new/1000)
plt.xlim([t[0]-1, t[-1] + 1])
plt.title('Distance Data Regression for Horizontal Acceleration')
plt.ylabel('Distance Travelled(km)')
plt.xlabel('Time(s)')
plt.show()


# define the function for fitting
def dis(t,c0,c1,c2):
    return (c0*t**2)+(c1*t)+c2

# applying the fit model
# z0=[50,5,0.1]          #initial guesses
fm1,covar=curve_fit(dis,t,zm)  # Altitude fit model
fm2,covar=curve_fit(dis,t,dm)  # Horizontal distance fit model

# printing optimal parameters
print('Optimal Parameters')
print(fm1)
print(fm2)

# calculate prediction
zp=dis(t,fm1[0],fm1[1],fm1[2])
dp=dis(t,fm2[0],fm2[1],fm2[2])

# calculate r^2
print('R^2 (for vertical acceleration): '+ str(r2_score(zm,zp)))
print('R^2 (for horizontal acceleration): '+ str(r2_score(dm,dp)))

print('Vertical Acceleration Component =', 2*fm1[0]*0.3048,'m/s^2')
print('Horizontal Acceleration Component =', 2*fm2[0],'m/s^2')
```

```
# plot data and prediction for vertical and horizontal acceleration
plt.figure()
plt.title('Altitude Data Regression for Vertical Acceleration')
plt.plot(t,zm/3280.84,'r—',label='Measured')
plt.plot(t,zp/3280.84,'b-',label='Predicted')
plt.ylabel('Altitude(km)')
plt.xlabel('Time(s)')
plt.legend(loc='best')
plt.show()

plt.figure()
plt.title('Distance Data Regression for Horizontal Acceleration')
plt.plot(t,dm/1000,'r—',label='Measured')
plt.plot(t,dp/1000,'b-',label='Predicted')
plt.ylabel('Distance Travelled(km)')
plt.xlabel('Time(s)')
plt.legend(loc='best')
plt.show()
```

Appendix B

Recorded Acceleration Data

In this appendix, examples for passenger aircraft vertical acceleration component data recorded by volunteers during actual flights throughout the take-off/climb and descent/landing portions of those flights are presented. The change of the vertical acceleration component with flight time during the mentioned legs recorded by two different volunteers; volunteer A and volunteer B aboard two different flights and aircraft models are shown in Figures B.1, B.2, B.3, and B.4.

From the figures, it can be generally noticed that the vertical acceleration component is strictly variating around 1 G (equal to the gravitational acceleration) during the take-off/climb and descent/landing portions of the flights under aircraft normal operating conditions. However, some instances of unusual (extreme) variations of the vertical acceleration component are seen on the figures either to values greater or less than 1 G. This is mainly attributed to unstable weather conditions (winds and gusts) or instantaneous impact forces to the aircraft body/landing gear during landing (touchdown).

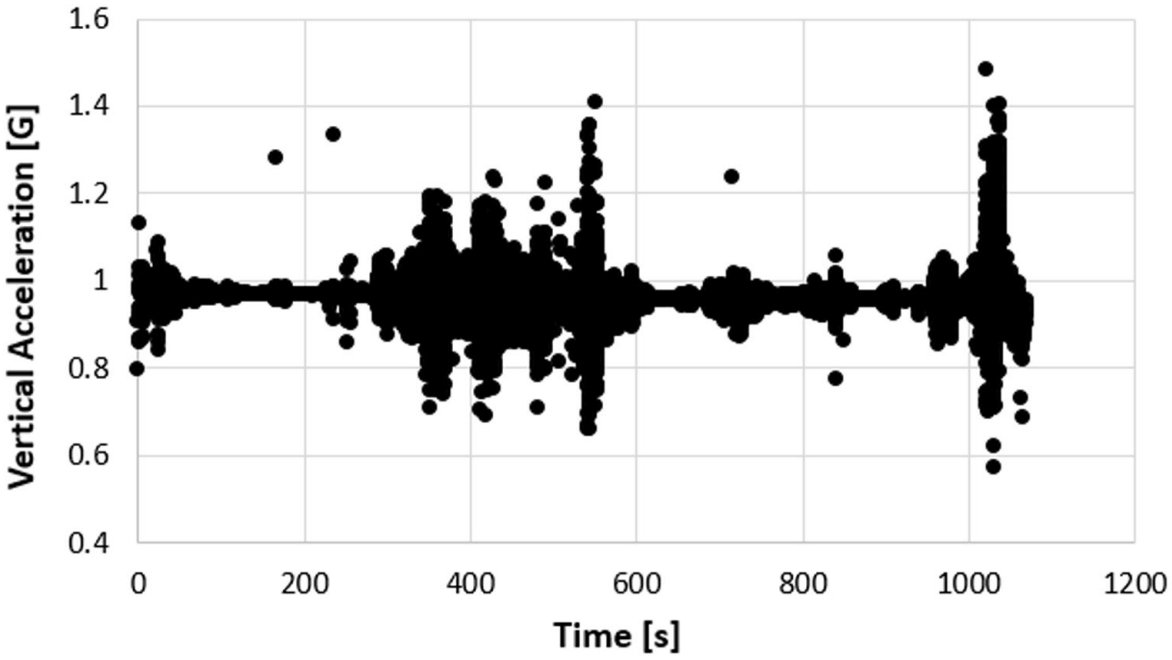

Figure B.1: Vertical acceleration component of a passenger aircraft during take-off and climb under normal operating conditions (recorded by volunteer A).

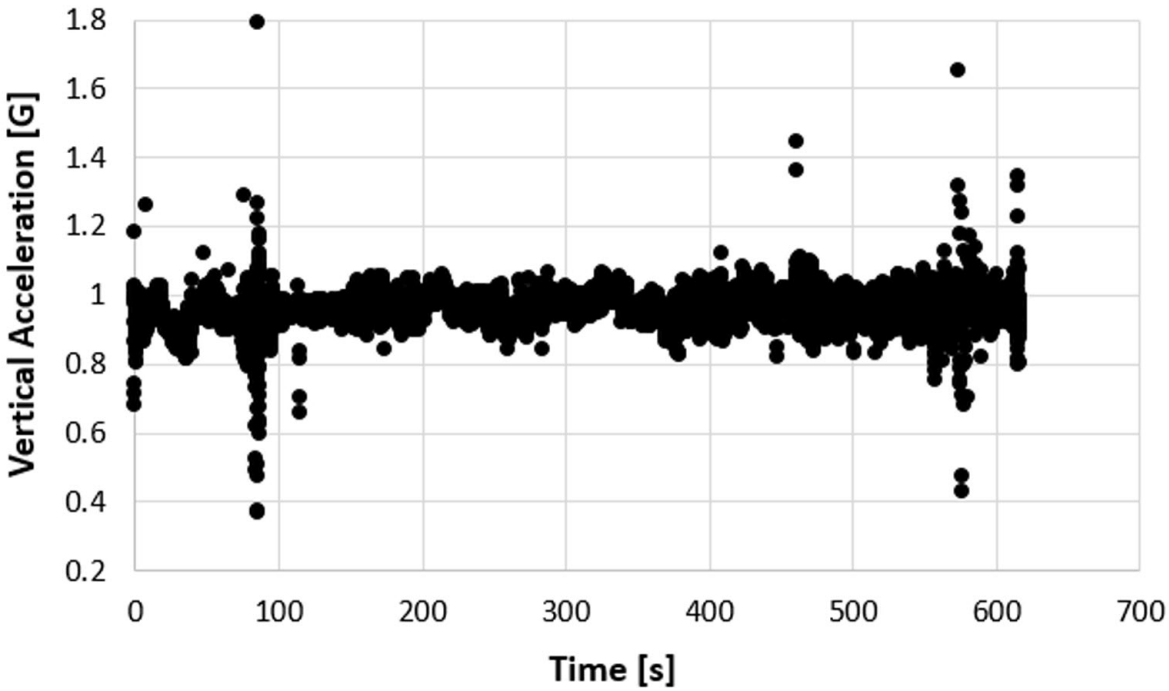

Figure B.2: Vertical acceleration component of a passenger aircraft during descent and landing under normal operating conditions (recorded by volunteer A).

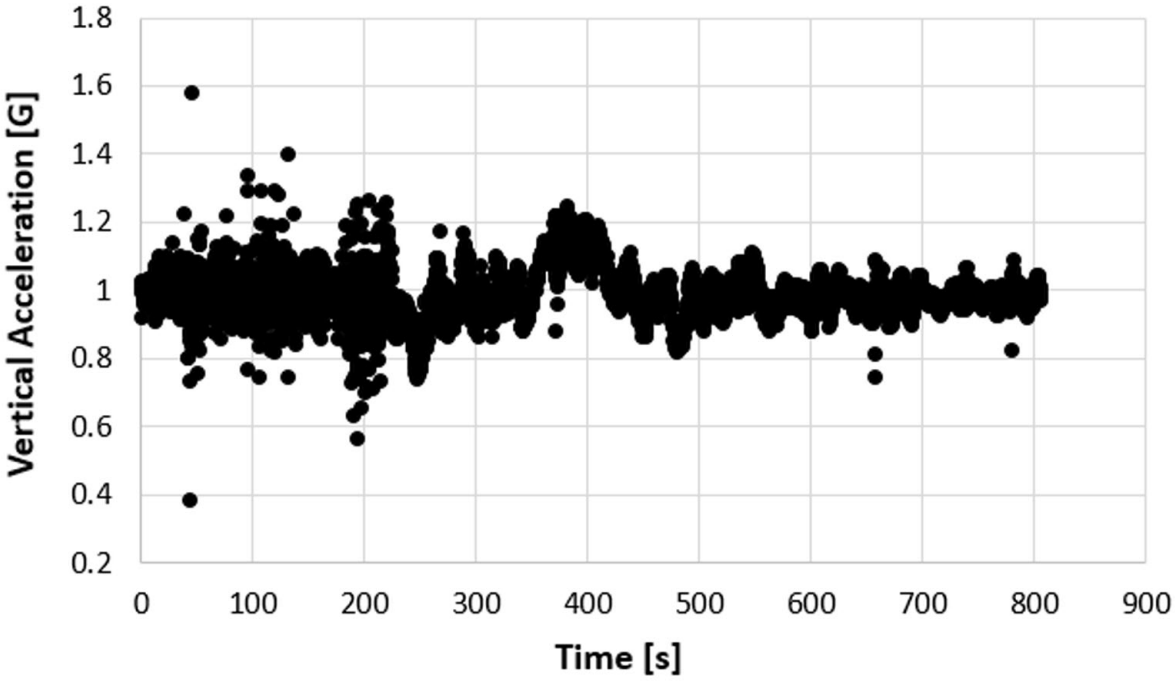

Figure B.3: Vertical acceleration component of a passenger aircraft during take-off and climb under normal operating conditions (recorded by volunteer B).

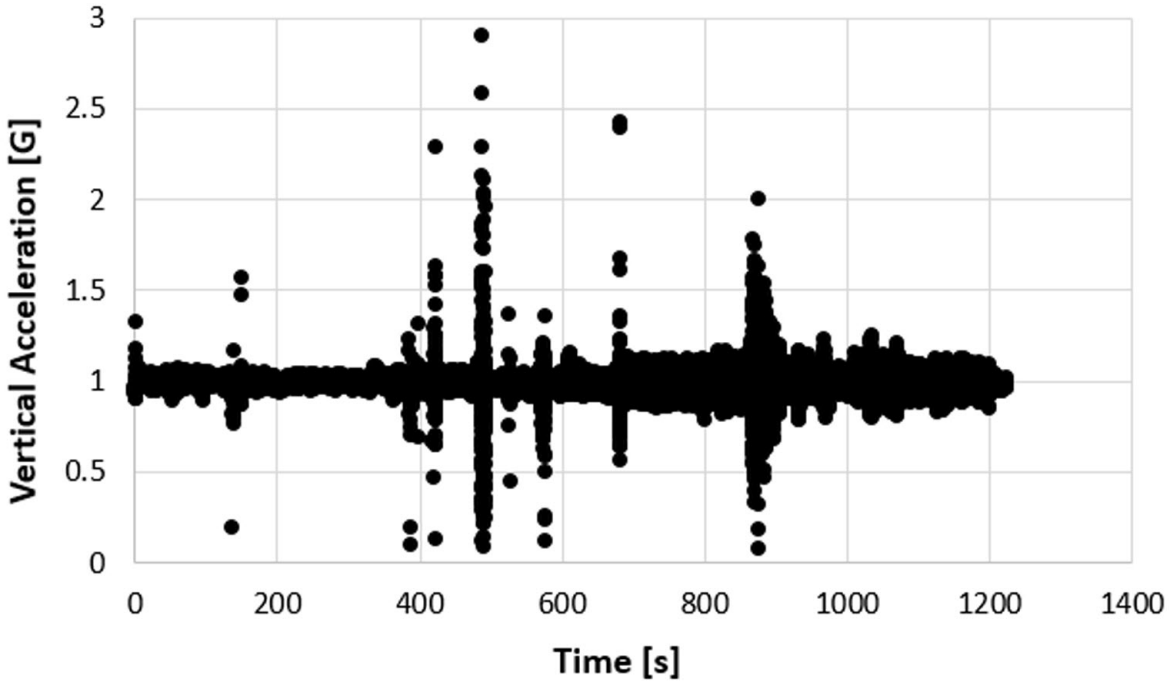

Figure B.4: Vertical acceleration component of a passenger aircraft during descent and landing under normal operating conditions (recorded by volunteer B).

Appendix C

Published Work

C.1 Peer-Reviewed Journal Papers

1. Elmaghraby, H. A., Chiang, Y. W., and Aliabadi, A. A. Ventilation strategies and air quality management in passenger aircraft cabins: A review of experimental approaches and numerical simulations. *Science and Technology for the Built Environment 24*, 2 (2018), 160–175. [Chapter 2]

2. Elmaghraby, H. A., Chiang, Y. W., and Aliabadi, A. A. Are aircraft acceleration-induced body forces effective on contaminant dispersion in passenger aircraft cabins? *Science and Technology for the Built Environment 25*, 7 (2019), 858–872. [Chapters 3, 4 and 6]

3. Elmaghraby, H. A., Chiang, Y. W., and Aliabadi, A. A. Airflow design and source control strategies for reducing airborne contaminant exposure in passenger aircraft cabins during the climb leg. *Science and Technology for the Built Environment*, accepted (2019). [Chapters 3, 4 and 7]

4. Elmaghraby, H. A., Chiang, Y. W., and Aliabadi, A. A. Normal and Extreme Aircraft Accelerations and the Effects on Exposure to Expiratory Airborne Contaminant inside Commercial Aircraft Cabins. *Science and Technology for the Built Environment*, under review. [Chapter 6]

C.2 Refereed Conferences

1. Elmaghraby, H. A., Chiang, Y. W., and Aliabadi, A. A. Effect of body forces due to aircraft acceleration on ventilation airflow and contaminant dispersion in passenger aircraft cabins. In *Proceedings of The Canadian Society for Mechanical Engineering (CSME) International Congress* (2018), Toronto, ON, Canada.

2. Elmaghraby, H. A., Chiang, Y. W., and Aliabadi, A. A. Can we limit the passenger exposure to airborne contaminants in commercial aircraft cabins during the climb leg? In *Proceedings of The Joint Canadian Society for Mechanical Engineering (CSME) and CFD Society of Canada (CFDSC) International Congress* (2019), London, ON, Canada.